UNIVERSITY OF HYDERABAD

DOCTORAL THESIS

Correlation between structural, microstructural and magnetic properties of $CoFe_2O_4$ and $La_{0.7}Sr_{0.3}MnO_3$ nano, bulk and thin films for possible room-temperature device applications

---

A thesis submitted in partial fulfillment of the award of the degree of
Doctor of Philosophy

in

Physics

by
Avisek Das
[Reg. No.: 15PHPH19]

School of Physics
University of Hyderabad
Hyderabad 500 046
Telangana, INDIA

May, 2022

DECLARATION

I hereby declare that the matter embodied in this thesis entitled, "**Correlation between structural, microstructural and magnetic properties of $CoFe_2O_4$ and $La_{0.7}Sr_{0.3}MnO_3$ nano, bulk and thin films for possible room-temperature device applications** ", is the result of investigations carried out by me in the School of Physics, University of Hyderabad, Hyderabad, India under the supervision of **Dr. Venkataiah Gorige**.

Place: Hyderabad
Date: 27/05/2022

Avisek Das
Reg. No. 15PHPH19

CERTIFICATE

This is to certify that the thesis entitled, "**Correlation between structural, microstructural and magnetic properties of $CoFe_2O_4$ and $La_{0.7}Sr_{0.3}MnO_3$ nano, bulk and thin films for possible room-temperature device applications** ", submitted by **Mr. Avisek Das** bearing the registration number: 15PHPH19 in partial fulfillment of the requirements for the award of Doctor of Philosophy in Physics at the School of Physics is a bonafide work carried out by him under my direct supervision.

This thesis is free from plagiarism and has not been submitted previously in part or in full to any other University or Institution for the award of any degree or diploma.

Further, the student has the following publications and conference proceedings before the submission of the thesis for adjudication.

Papers in refereed journals

(3) Dielectric and electron spin resonance studies of (x) $NiFe_2O_4$ (1-x) $BaTiO_3$ magnetoelectric composites.
P. Bongurala, Mrinalini, **Avisek Das** and V. Gorige,
J. Alloys Compd., **903**, 163931 (2022).

(2) Correlation between size, shape and magnetic anisotropy of $CoFe_2O_4$ ferrite nanoparticles.
Avisek Das, Kranthi kumar Bestha, Prakash Bongurala and Venkataiah Gorige
Nanotechnology **31,** 335716 (2020).

(1) A comparative study of a (0-3) connectivity type composite and core-shell structure of $CoFe_2O_4$ - $BaTiO_3$ based on microstructure and magnetic property.
Avisek Das and V. Gorige,
AIP Conf. Proc. **1942**, 130056, (2018).

Manuscripts under preparation

3. Electric and magnetic tuning of Gilbert damping factor in LSMO/PMN-PT(011) heterostructure.
Avisek Das, Mrinalini, T. Usami, S. P. Pati, T. Taniyama and V. Gorige,

2. Investigation on structure, morphology and magnetic properties of PLD grown CFO/Pt-Si(111) thin films of variable thickness.
Avisek Das, J. Rout and V. Gorige.

1. Magnetic and FMR studies on LSMO deposited on PMN-PT oriented along [001], [011] and [111].
Avisek Das, A. Sridhar and V. Gorige.

Conferences attended

7. Workshop on *" Functional Magnetic Materials"* organized by University of Hyderabad, Hyderabad – India 26th February – 3rd March 2018.

6. Workshop on *"Processing and Characterization of Thin Films"* organized by University of Hyderabad, Hyderabad – India, 3rd -9th January 2018.

5. National Conference on *'Physics at Small Scales and Advanced Materials'* 2017 held at the University of Hyderabad during 8th to 9th September 2017,

   Poster Presentation *Magneto-electric Coupling in Ferrite-Ferroelectric Composite.*

4. National Conference on Condensed Matter Physics 2017, organized by the Department of Physics, Tripura University, Participated

3. DAE Solid State Physics Symposium (DAE-SSPS 2017), BARC, Mumbai,

   Poster Presentation *A comparative study of a (0-3) connectivity type composite and core-shell structure of $CoFe_2O_4$ - $BaTiO_3$ based on microstructure and magnetic property.*

2. International Conference of Young Researchers on Advanced Materials (IUMRS-ICYRAM 2016) held at Indian Institute of Science, Bangalore during 11th -15th December 2016, participated.

1. National Conference on Frontiers in Physics (FIP) held at University of Hyderabad, Hyderabad during 28th -29th March 2016, participated.

Further, the student has completed the following courses towards the fulfillment of course-work required for Ph.D.

S.No.	Course code	Name of the course	Credits	Pass/Fail
1	PY801	Advanced Quantum Mechanics	4	Pass
2	PY803	Advanced Statistical Mechanics	4	Pass
3	PY804	Advanced Electromagnetic Theory	4	Pass
4	PY821	Research Methodology	4	Pass

27/5/2022

Dean
School of Physics

संकाय अध्यक्ष / Dean
भौतिकी संकाय / School of Physics
हैदराबाद विश्वविद्यालय
UNIVERSITY OF HYDERABAD
हैदराबाद / HYDERABAD-500 046. भारत / INDIA.

27/05/2022.

Dr. Venkataiah Gorige
Thesis Supervisor
School of Physics

Dr. VENKATAIAH GORIGE
Assistant Professor
School of Physics, University of Hyderabad
Gachibowli, Hyderabad 500046, INDIA

ACKNOWLEDGEMENTS

I am pleased to express my deepest gratitude and sincere thanks to my supervisor Dr. Venkataiah Gorige for giving me an opportunity to join his research group and for supporting me in carrying out different experiments to accomplish my dream.

I would like to take this opportunity to thank my doctoral review committee members Prof. Ashok Chatterjee and Prof. S. Srinath for their valuable suggestions and insightful questions. I would also like to thank Dr. A. Rajanikanth for sharing his valuable knowledge on various aspects of magnetism.

I am thankful to the present Dean, Prof. K.C James Raju and former Deans, Prof. Ashok Chatterjee, Prof. V. Seshubai, Prof. Bindu A. Bambah and Prof. Rajender Singh for allowing me to use the departmental facilities.

I am obliged to Professor-in-charge, Center for Nanotechnology, University of Hyderabad, for allowing me to use Physical Property Measurement System for carrying out the magnetic measurements and also for allowing me to use the clean room facility. I wish to thank Mr. Pankaj who helped me for carrying out the TEM imaging. I wish to thank Mr. Sudhakar and Ms. Y. Jyothi for XRD measurements. I thank Ms. Sunitha and Mr. Santosh for helping me in FESEM imaging. My special thanks to Mr. T. Abraham, Mrs. Shailaja, Mr. Prasad, Mrs. Deepika, Mr. Sudarshan, Ms. Vijaya Lakshmi, Mr. Mukunda Reddy, Mr. Srinivas, and other non-teaching staff at the School of Physics.

I would like to thank Dr. J. Arout Chelvane, Scientist, Defence Metallurgical Research Laboratory, Hyderabad for allowing me to perform magnetic measurements in his laboratory.

I would like to thank our collaborator Prof. Tomoyasu Taniyama, Nagoya University, Japan for opening up his laboratory facilities while I made my visit to that place. I'm utmost grateful to Dr. Satya Prakash Pati and Dr. Takamasa Usami for not only helping me in performing all the experiments but also for all the fruitful discussions while analysing the results. Their cooperation both in and out of laboratory made the visit a joyful and learning experience.

I would like to thank my seniors of University of Hyderabad, Dr. Binoy Krishna Hazra, Dr. B. Ravi Kumar, Ms. Uma Lavanya, Dr. Luluh K Jahan, Dr. P.V. Madduri, Dr. j. Pundareekam Goud, Dr. Joshy Joseph, Dr. Atiya Farheen, Dr. Nisha, Dr. Arun Nimmala, Dr. Ravi and others. I would specially like to thank Binoy da for sharing his knowledge on different techniques and research basics in my early days of PhD program. I'm immensely grateful to him for extending his emotional support while I needed it the most.

I'm thankful to my lab members, Dr. Anupama Swain, Dr. Prakash Bongurala, Ms. B. Praneetha, Mr. B. Kranthi Kumar, Mr. Joyal John Abraham, Mr. Rajesh Puntia, Mr. Rangarao, Mr. Sridhar, Mr. Rajesh Gangwar, Mr. Jyotiranjan Rout, Ms. Mrinalini, Mr. D. Balaganesh, Ms. Anna Rose, Ms. Mahima Ann Paul and Ms. Krupa Ann Paul. The time spent on discussion especially with Anupama, Prakash,

Praneetha and Kranthi helped me in many ways. I hope the formed bonds between us will continue and strengthen with time.

I would like to thank my juniors, Mr. Kuntal Bhattacharyya, Mr. L. Akum, Mr. Mainur Rahaman, Mr. Chandan Ghorui, Ms. Pooja Saini, Mr. Vinod Rajput, Dr. Atasi Ray, Mr. Nurul Hassan, Dr. Nazir, Mr. Samir Das, Mr. Avishek Saha, Dr. Sovan Sau, Ms. Debika Debnath, Mr. Anirban Debnath, Mr. Subhadeep Saha, Mr. Venkat Reddy, Mr. Pavan Verma, Mr. Jiwan, Mr. Soumen Nayak, Mr. Suman Panja and others. I would specially like to thank Mainur for spending his valuable time on fruitful discussions of FMR data.

My teachers, right from school, are the ones whose motivation and teaching made the ground for my growing interest in academia. Though there are many of them, I would specially like to mention, Subrata Sir, Ram Sir, Arindam sir, Amalendu sir and Ashish Sir who became an inspiration for me to pursue higher education.

The exciting physics lessons of Prof. Barin Kumar De and Prof. Syed Arshad Hussain, of Tripura University made my journey in the field of Physics exciting. I was fortunate enough to come in contact with Prof. Hussain in my school days.

I feel myself blessed to be a part of Ramakrishna Mission fraternity, where I came in contact with my friend, Dr. Phanibhusan Singha Mahapatra, Rahul Bandyopadhyay, Bappaditya Sankhari, Dr. Suman Sarkar, Gopal Jana, Dr. Prosenjit Majumdar, Dr. Kushal Mazumdar, Anjan Das, Dr. Bapan Paul, Mr. Bireshwar Paul and others. The numerous discussions on various topics helped me to shape my career and grow as a person. I would specially like to acknowledge Phani, whose passion towards science and physics, in particular, was inspiring to me.

I would take this platform to thank my PhD batch mates, Late Rashmiranjan Suna, Dr. Nilanjan Basu, Dr. Sujai Matta, Dr. Muhammed Rasi M., Dr. Y. Rajesh, Mr. Naresh Shyaga, Mr. Mohammed Abu Taher, Mr. Mohammed Zahid Mallik, Ms. Leelashree S. Ms. Manasa Kalla, Mr. Vinod, Mr. Hemant Kumar Sharma, Mr. Bappaditya Sankhari, Mr. M. Praveen Kumar and Dr. Subrata Mondal. I would like to thank my friends, Dr. Apurba De, Dr. Sheikh Saddam Hussain from School of Chemistry and Dr. Arijit Mukherjee from School of Mathematics, for their support.

It will be difficult to describe in words about the love, care, companionship, support received from Rasi, Zahid, Shivaraju, Leela, Manasa, Hiba and Chaitu. Without their presence, this document would not have seen light of the day. They stood as pillars of support whenever I need. The days spent with them are worth for lifetime and I'm lucky enough to have them in my life.

Last but not the least, I am in debt to my parents, Ms. Supriya Das and Mr. Anjan Kumar Das for the uncountable sacrifices made. I feel myself lucky to be raised in a family where the decisions made by an individual are respected. I'm lucky to have a younger sister, Ms. Sumedha Das, whose entrepreneurship skills inspires me.

At last I would like to thank the popular science writers who make physics interesting to the budding scientists by their wonderful and lucid explanations.

Dedicated

to

Parents, Sister, Friends and
Popular science writers

List of Abbreviations

AC	Alternating current
Ae	Alkaline earth metal
AFM	Antiferromagnetic; Antiferromagnetism; Atomic force microscopy
CCD	Charge coupled device
CFO	Cobalt ferrite
CPW	Coplanar waveguide
DE	Double exchange
e	electron(s); charge of electron
E	Anisotropy energy
EDX	Energy dispersive x-ray
E-field	Electric field
ESR	Electron spin resonance
f	frequency
FE	Ferroelectric
FESEM	Field emission scanning electron microscopy
FM	Ferromagnetic; Ferromagnetism
FMR	Ferromagnetic resonance
FWHM	Full-width at half-maxima
H-field	Magnetic field
HRTEM	High resolution transmission electron microscopy
H_C	Coercivity
ICDD	International center for diffraction data
IP	In plane
LLG	Landau-Lifshitz-Gilbert
LSMO	$La_{0.70}Sr_{0.30}MnO_3$
M	Magnetization
MCA	Magnetocrystalline anisotropy
ME	Magnetoelectric
MFM	Magnetic force microscopy
M−H	Magnetic hysteresis
M_r	Remanent magnetization
M−T	Temperature-dependent magnetization
OP	Out-of-plane

List of Abbreviations

P−E	Polarization versus electric field
PE	Paraelectric
PM	Paramagnetic
PMN-PT	$Pb(Mg_{1/3}Nb_{2/3})O_3$–$PbTiO_3$
PPMS	Physical property measurement system
PZT	$PbZrTiO_3$
PLD	Pulsed laser deposition
Q	Quality factor
RT	Room temperature
SAED	Selected area electron diffraction
SE	Superexchange
S-K	Stranski- Krastinov
SPM	Superparamagnetic; Superparamagnetism
SW	Spin-wave
T_C	Curie temperature
TEM	Transmission electron microscopy
VSM	Vibrating sample magnetometer
XRD	X−ray diffraction
α	Gilbert damping constant
χ^2	Goodness of fit

List of Figures

1.1 Schematic representation of "double exchange" interaction in manganites. 5
1.2 Schematic representation of " double exchange" interaction in manganites. 5
1.3 Schematic representation of spinel ferrite structure 9
1.4 Phase diagram of $La_{1-x}Sr_xMnO_3$. AFM-I denotes antiferromagnetism insulator; CO denotes ordering; FM-I ferromagnetic insulator; FM-ferromagnetic metal 10

2.1 Flowchart of formation of CFO nanoparticles using thermal decomposition via PVA method. 18
2.2 Flowchart for synthesis of LSMO using sol-gel method. 19
2.3 Schematic representation of PLD chamber and its deposition geometry. 20
2.4 Inside view of PLD chamber during the growth process. 22
2.5 Schematic representation of x-ray diffractometer in θ-2θ geometry. . . 24
2.6 Photograph of field emission scanning electron microscope 26
2.7 The photograph of transmission electron microscope. 28
2.8 Photograph of physical property measurement system 30
2.9 (a) Precession of the magnetic moment with a magnetization vector M towards the effective magnetic field direction due to the presence of damping like torque, (b) The splitting of the energy levels in the presence of magnetic field where the energy difference of the atomic levels at resonance $g\mu_B H_{res}$ is equal to the energy of the microwave power $h\nu$ 32
2.10 Schematic representation of co-planar wave guide based FMR. 32
2.11 Photograph of coplanar waveguide based FMR measurement system. 33

3.1 The room-temperature XRD patterns of CFO samples sintered at different temperatures. 39
3.2 Williamson-Hall plot for the CFO samples. 40

3.3 Rietveld refined XRD (solid red) patterns along with experimentally measured (black circles) ones for (a) CFO-300 (7 nm) and (b) CFO-1200 (780 nm) samples. The blue curve represents the difference in measured and simulated patterns. The marked vertical (green) bars represents the Bragg positions. 41
3.4 The FESEM micrographs of CFO samples. 43
3.5 The tem micrograph images of CFO samples. The SAED patterns and high resolution images are shown in corresponding insets. 44
3.6 A schematic illustration of the transformation from octahedral shape to truncated octahedral shape of CFO nanoparticles. 45
3.7 Temperature-dependent magnetization (M-T) curves of CFO samples. dM/dT versus T plots are shown in insets. 47
3.8 The M-H loops of set of CFO samples measured at (a) 300 K and (b) 5 K. 48
3.9 The plots of particle size dependence of (a) H_C, (b) M_S, (c) M_r and (d) squareness ratio for CFO samples measured at 5 K and 300 K, respectively. 48
3.10 The schematic representations of possible magnetization orientations (solid red arrows) in different shape particles, proposed for CFO. . . . 49
3.11 The law of approach to saturation fit to the M-H plots for CFO samples sintered at different temperatures. 51
3.12 (a) Variation of effective magnetic anisotropy constant as a function of particle size for CFO samples at 300 K. (b) The values of BH_{max} as a function of particle size estimated at 5 K (black solid symbols) and 300 K (red hollow symbols). 52
3.13 The room-temperature XRD patterns of LSMO samples along with Rietveld refinement of the patterns. 55
3.14 The Williamson-Hall plot for the LSMO-700 and LSMO-1200 samples. 56
3.15 The FESEM micrographs of LSMO samples. 57
3.16 (a) and (c) M-H loops of LSMO-700 and LSMO-1200 respectively; (b) and (c) M-T plots of LSMO-700 and LSMO-1200 respectively 58

4.1 XRD peaks of cobalt ferrite thin films with varying thickness. 64
4.2 (a)-(f) FESEM images of the sample with varying thickness. (g) Inset shows the composition of the samples obtained through EDAX. (h) Thickness of a 300 nm film obtained through cross sectional FESEM. . 66
4.3 (a)-(f) Magnetic force microscopic images of the samples showing re-orientation of the spin of the samples with increasing thickness. (g)-(l) Atomic force microscopic images of the samples showing the graineness of the samples with increasing thickness. 68
4.4 (a)-(f) IP (represented by black dots) and OP (represented by red dots) $M - H$ loops with the change in film thickness at RT. 70

4.5 (a)Variation of H_C for IP and OP samples with increase in thickness.(b)Variation of M_S for IP and OP samples with increase in thickness. 70
4.6 Law of Approach to saturation fit for CFO thin films of varying thickness. 71
4.7 Variation of effective magnetic anisotropy constant for "in-plane" and "out-of-plane" samples of CFO thin film with increase in thickness. . . 72
4.8 The room temperature Raman spectra of CFO thin films of varying thickness. 73
4.9 Lorentzian profile fitted Raman spectra of CFO films at different thickness. 74

5.1 XRD (θ-2θ) patterns for LSMO films deposited on PMN-PT substrates oriented along [001], [011] and [111] directions. 82
5.2 The M-T data of LSMO deposited on PMN-PT(001) (represented by black squares), PMN-PT(011) (represented by red dots), PMN-PT(111) (represented by blue triangles) and (inset) shows the corresponding dM/dT versus T plots. 84
5.3 In-plane M-H loops measured in different orientations of the LSMO sample deposited on PMN-PT(001). 85
5.4 Polar plot of M_r/M_S versus rotation angle of LSMO/PMN-PT(001) heterostructure. 86
5.5 (a) Unit cell of cubic PMN-PT(001), (b) represents the 2-D view of the polarization directions of PMN-PT(001) plane, (c) the solid lines represents the magnetization direction of LSMO and (d) the projections of magnetic orientations of LSMO with respect to the polarization directions of the PMN-PT and (e) The projected directions of LSMO on PMN-PT. 87
5.6 In-plane M-H loops measured for different in-plane orientations with respect to applied field of the LSMO sample deposited on PMN-PT(011). 88
5.7 Polar plot of M_r/M_S versus rotation angle of LSMO/PMN-PT(011) heterostructures. 89
5.8 (a) Unit cell of cubic PMN-PT(011), (b) solid lines represent the polarization directions, (c) the resultant polarization direction and (d) the orientation of LSMO with respect to PMN-PT. 90
5.9 In-plane M-H loops of the LSMO sample deposited on PMN-PT(111) in different orientations. 91
5.10 Polar plot of M_r/M_S versus rotation angle for LSMO/PMN-PT(111) heterostructure. 92
5.11 (a) Unit cell of cubic PMN-PT(111), (b) projections of the polarization directions, (c) resultant of the projected polarization on (111) plane of PMN-PT and (d) magnetization directions of LSMO. 93

6.1 The lineshape plot of LSMO/PMN-PT(001) with a frequency ranging from 1-20 GHz by varying applied magnetic field from -400 to 4000 Oe in different directions. 97
6.2 The plot of absorption frequency versus resonance field for (a) unpoled (b) positively poled and (c) negatively poled LSMO/PMN-PT(001) samples in different directions. The solid (red) lines show the Kittle fit. 99
6.3 The linewidth versus frequency plot of unpoled and poled samples of LSMO/PMN-PT(001) applying H-field along the easy axis (a) and hard axis (b) directions, respectively 100
6.4 The lineshape plot of LSMO/PMN-PT(011) with a frequency ranging from 1-20 GHz by varying applied magnetic field from -400 to 4000 Oe in different directions. 102
6.5 The plot of absorption frequency versus resonance field for (a) unpoled sample (b) positive poled and (c) negative poled LSMO/PMN-PT(011) in different directions. The solid lines shows the Kittle fit. . . . 103
6.6 The linewidth versus frequency plot of unpoled and poled samples of LSMO/PMN-PT(011) applying H-field along the easy axis (a) and hard axis (b) directions, respectively. 104
6.7 The lineshape plot of LSMO/PMN-PT(111) with a frequency ranging from 1-20 GHz by varying applied magnetic field from -400 to 4000 Oe in different directions. 106
6.8 The plot of absorption frequency versus resonance field for (a) unpoled sample (b) positive poled and (c) negative poled LSMO/PMN-PT(111) in different directions. The solid lines shows the Kittle fit. . . . 107
6.9 The linewidth versus frequency plot of unpoled and poled samples of LSMO/PMN-PT(111) applying H-field along the easy axis (a) and hard axis (b) directions, respectively. 108

List of Tables

3.1 Crystallographic and particle size data of CFO samples. 42
3.2 The crystallographic data of LSMO samples. 55

4.1 Variation of lattice mismatch, induced strain with the change in thickness of CFO films. 65
4.2 The deconvoluted Raman peak positions of CFO samples with varying thickness. 75
4.3 The force constant, cation distribution and magnetic moment values of CFO samples for different thicknesses. 76

6.1 The Gilbert damping constant α for LSMO/PMN-PT(001) in different directions with and without electric poling. 101
6.2 The Gilbert damping constant α for LSMO/PMN-PT(011) in different directions with and without electric poling. 104
6.3 The Gilbert damping constant α for LSMO/PMN-PT(111) in different directions with and without electric poling. 109

Contents

1 Introduction **1**

1.1 Ferromagnetism (FM) . . . 2
1.2 Ferrimagnetism . . . 3
1.3 Magnetic interactions . . . 3
1.3.1 Exchange energy . . . 3
1.3.2 Double exchange . . . 4
1.3.3 Superexchange . . . 4
1.4 Static magnetic property . . . 6
1.4.1 Magnetic Anisotropy . . . 6
1.4.1.1 Magnetocrystalline Anisotropy (MCA) . . . 6
1.4.1.2 Uniaxial Anisotropy . . . 7
1.4.1.3 Shape anisotropy . . . 7
1.5 Dynamic magnetic property . . . 8
1.5.1 Magnetization dynamics and "Landau-Lifshitz-Gilbert equation" 8
1.6 Aims of the present work . . . 9
1.6.1 $CoFe_2O_4$ (CFO) . . . 9
1.6.2 $La_{0.7}Sr_{0.3}MnO_3$ (LSMO) . . . 9
1.6.3 Literature review . . . 10
1.6.4 Objectives of the thesis . . . 12
1.6.5 Organization of the thesis . . . 12

2 Experimental methods **17**

2.1 Overview . . . 17
2.2 Preparation . . . 17
2.2.1 Preparation of nano and bulk samples: CFO . . . 17
2.2.1.1 Polymeric method via thermal decomposition . . . 17
2.2.2 Preparation of nano and bulk samples: LSMO . . . 18
2.2.3 Preparation of PLD target: CFO . . . 19
2.2.4 Preparation of PLD target: LSMO . . . 19
2.2.5 Thin films (PLD) . . . 20
2.2.5.1 Working principle . . . 20
2.2.5.2 Growth of the film . . . 21
2.2.5.3 Deposition of CFO thin films . . . 22
2.2.5.4 Deposition of LSMO thin films . . . 22
2.3 Characterization . . . 23

2.3.1 Structural : XRD . . . 23
2.3.1.1 Rietveld analysis . . . 23
2.3.2 Structural : Raman spectroscopy . . . 25
2.3.2 Morphology : FESEM . . . 25
2.3.3 Energy dispersive x-ray (EDX) spectroscopy . . . 26
2.3.4 Microstructure Analysis : High resolution transmission electron microscopy (HRTEM) . . . 27
2.3.5 Magnetic Force Microscopy (MFM) . . . 27
2.4 Physical properties . . . 29
2.4.1 Static magnetic properties . . . 29
2.4.1.1 Physical property measurement system (PPMS) . . . 29
2.4.2 Dynamic magnetic properties . . . 30
2.4.2.1 Ferromagnetic resonance (FMR) . . . 30
2.5 Conclusion . . . 34

3 Structural, morphological, microstructural and magnetic properties of $CoFe_2O_4$ and $La_{0.7}Sr_{0.3}MnO_3$ bulk and nanoparticles 37
3.1 $CoFe_2O_4$ . . . 37
3.1.1 Introduction . . . 37
3.1.2 Experimental . . . 38
3.1.3 Results and discussion . . . 38
3.1.3.1 X-ray diffraction . . . 38
3.1.2.2 FESEM . . . 42
3.1.3.3. HRTEM . . . 43
3.1.3.4 Growth mechanism . . . 44
3.1.3.5 Magnetic properties . . . 46
3.2 $La_{0.7}Sr_{0.3}MnO_3$ . . . 53
3.2.1 Introduction . . . 53
3.2.2 Experimental methods . . . 53
3.2.3 Results and discussions . . . 54
3.2.3.1. X-ray diffraction . . . 54
3.2.3.2. FESEM . . . 56
3.2.3.3. TEM . . . 56
3.2.3.4. Magnetic properties . . . 57
3.3 Summary . . . 58

4 Structural, morphological and magnetic properties of CFO thin films 62
4.1 Introduction . . . 62
4.2 Experimental . . . 62
4.3 Results and discussion . . . 63
4.3.1 Structural analysis . . . 63
4.3.2 Morphological analysis . . . 65
4.3.2.1 FESEM . . . 65

4.3.2.2 MFM and AFM 67
4.3.3 Magnetization 69
4.3.4 Raman spectroscopy 72
4.4 Summary 76

5 Structural and magnetic properties of LSMO/PMN-PT heterostructures 80
5.1 Introduction 80
5.2 Experimental 81
5.3 Results and discussion 81
5.3.1 Structure 81
5.3.2 Magnetic Properties 83
5.3.2.1 LSMO/PMN-PT(001) 84
5.3.2.2 LSMO/PMN-PT(011) 87
5.3.2.3 LSMO/PMN-PT(111) 90
5.4 Summary 93

6 Ferromagnetic resonance studies of LSMO/PMN-PT heterostructures 95
6.1 Introduction 95
6.2 Experimental 96
6.3 Results 96
6.3.1 LSMO/PMN-PT(001) 96
6.3.1.1 Lineshape measurements 96
6.3.1.2 Kittel fit 98
6.3.1.3 Gilbert damping factor 99
6.3.2 LSMO/PMN-PT(011) 101
6.3.2.1 Lineshape measurements 101
6.3.2.2 Kittel fit 102
6.3.2.3 Gilbert damping factor 103
6.3.3 LSMO/PMN-PT(111) 105
6.3.3.1 Lineshape measurements 105
6.3.3.2 Kittel fit 106
6.3.3.3 Gilbert damping factor 107
6.4 Summary 109

7 Summary and conclusion 111
7.1 Summary and conclusions 111
7.2 Future scope 113

Chapter 1

Introduction

Research on magnetism is crucial not only in the understanding of the basic underlying physics but also in designing many day-to-day device applications. Magnetic nanoparticles are widely used in electrical devices such as hard disc drives, the car industry such as hybrid-electric vehicles, and medical applications such as targeted medication delivery, to mention a few [1]. The ever-increasing need for faster data processing and more data storage has resulted in major increases in energy usage and environmental issues [2]. This growth in data storage capacity has come at a tremendous cost in terms of energy use. Big data centers, which accounted for 1–1.5% of worldwide electricity consumption in 2010, support cloud data storage and online information exchange, with an increase in consumption of 3 to 13% predicted by 2030, depending on steps implemented to decrease power expenditure [3]. With this in mind, efforts are being made to develop ultra-low-power consumption gadgets. One of the exciting study topics of current attention within the scientific community is the achievement of "ultra-low power consumption" in switching and "memory devices" [4, 5]. The binary information is put in ferro(ferri)magnetic medium, in which the "spin" orientation "up" or "down" is labeled as "0" or "1" in contemporary magnetic data storage systems [6,7]. In most cases, a magnetic field is utilized to write/store digital information in magnetic material, requiring a large amount of electric current. The traditional method of manipulating magnetism, on the other hand, requires a considerable quantity of current, resulting in a large amount of power being spent, with a portion of it being dissipated as Joule heat. There is a need to search for a different approach to manage magnetism in this regard.

One of the growing topics for "next-generation" miniaturized data storage devices aims towards minimum possible power consumption while increasing memory and processing capabilities. Electrons and/or holes having spin degrees of freedom, interacting with their orbital moments, are used in devices [9]. In this aspect, "electric field-controlled magnetic anisotropy" in nanoparticles plays a vital role [9]. In the case of bulk magnetic materials, the "dipolar" (demagnetizing) field, originating from the corners, causes the magnetization (M) to split apart into domains rather often. Depending on the materials, the size d_{domain} of the domains might range from tens of nanometers to micrometers or even centimeters. When the system's size is in

nano scale, the "exchange interaction" takes over, and the system becomes a single-domain state. The anisotropy influences the magnetic orientation in the system of consideration. The "exchange length", derived from the competition within the "exchange energy" and "magnetostatic energy", magnetic distortions may still persist near the device's margins [9].

In inverse spinel $CoFe_2O_4$ (CFO), The "Co^{+2}" ions mostly occupy the "octahedral" (B) sites and whereas "Fe^{+3}" occupy both "tetrahedral" (A) and B sites [10, 11]. Due to their interesting "anisotropy", high coercivity (H_C), low saturation magnetization (M_S), and outstanding "mechanical" and excellent "chemical" consistence at ambient temperature, CFO has gained a lot of attention from the researchers [12, 13]. The CFOs are widely utilized in "sensors, recording devices, magnetic cards, solar cells, magnetic drug delivery, bio-medicine, catalysis, biotechnology" etc. [14, 15].

Manganites, which are manganese perovskite oxides with a strong "spin polarization" property, have been chosen as the potential material in this study to accomplish magnetic manipulations by different techniques. In terms of manipulating M by applying an electric field (E-field), the present thesis includes both "fundamental" and "application" aspects.

A brief overview of the properties involved in understanding the different phenomena exhibited by the synthesized materials has been discussed in the subsequent sections.

1.1 Ferromagnetism (FM)

The most important property of magnetic materials is ferromagnetism (FM). The magnetic exchange interactions are largely responsible for the ordering of atomic magnetic moments [2, 16]. The FM, which is showed by specific metals, alloys, and compounds of "transition metal ions" and "rare earth elements", the spins prefer to align in a single direction below a temperature known as Transition temperature (T_C). In the absence of applied field, all magnetic moments in a FM substance are effectively aligned in areas known as magnetic domains, yielding a net non-zero magnetic moment. Above T_C, the FM oxide materials act like paramagnetic. The Curies' law assumes the isolated magnetic moments and are solely influenced by the applied magnetic and thermal fields [17]. Weiss, however, updated Curie's rule for FM materials in 1907 by incorporating the concept of a molecular field 'H_m'. This phrase refers to the internal field that exists within a material and acts along with the applied field H. Thus,

$$H_m = \gamma M \tag{1.1}$$

here, γ is "molecular field constant", H_m represents "molecular field". Hence, the net field in the system is given by

$$H_t = H + H_m \tag{1.2}$$

where, H represents applied field. Weiss postulated the Curie's law as,

$$\chi = \frac{M}{\rho H} = \frac{C}{T - \theta} \tag{1.3}$$

The above formula is well known as the "Curie-Weiss law", here, θ in the denominator is called as Weiss constant, which quantifies the strength of magnetic interactions.

1.2 Ferrimagnetism

As stated earlier, CFO has become an indispensable part of the technological revolution due to its high electrical resistivity, low eddy current, and dielectric behavior. These materials have several practical and potential applications in many latest applied scientific fields such as microwave devices, high-frequency applications, permanent magnets, magnetic data storage, magnetic imaging, and targeted drug delivery [18–20]. The magnetic interactions, as well as the magnetic properties, are driven by the placement of ions in the lattice of the ferrite. Different interactions within a system help one to understand the magnetic ordering of a system. Therefore, M in ferrites arises from the "uncompensated" anti-ferromagnetism (AFM). Here the magnitude of M rely on stoichiometry, cationic arrangement, and the relative intensity of the probable interactions. The Neel model describes the spinel ferrites to exhibit three different magnetic interactions between "tetrahedral" and "octahedral" sites. When these two ions are at "tetrahedral" A-site, it is termed as "A-A interaction"; and are at "octahedral" B-site, it is termed as "B-B interaction", and when one ion is at "tetrahedral" A-site and the other one at "octahedral" B-site, it is termed as A-B interaction. As compared to the other two magnetic interactions (A-A) and (B-B), the (A-B) interaction is very strong. This type of interaction is known as a superexchange (SE) interaction. This can be explained as the "magnetic exchange forces" between the metallic ions in ferrites "mediated by an exchange mechanism via oxygen ions" [21].

1.3 Magnetic interactions

1.3.1 Exchange energy

Magnetic materials display long-range ordering of magnetic moments due to the numerous types of exchange interactions found in these materials. The exchange interaction is a phenomenon in which individual atomic magnetic moments strive to coordinate all other "atomic magnetic moments" inside a material by themselves [22]. Dipole exchange, SE, and double exchange (DE) are the three basic types of exchanges [22]. Many molecules' total energy, as well as the covalent bond in many

materials, is made up of exchange energy. The Hamiltonian gives the exchange energy between atoms i and j with total spins S_i and S_j in a many-electron system of crystal.

$$H_{ex} = -\Sigma J_{ij} S_i . S_j \tag{1.4}$$

where, J_{ij} is the "effective exchange integral" between "i" and "j" atoms with total spins S_i and S_j. If J_{ij} is positive, H_{ex} is "minimum" when spins are "parallel" (FM) and a "maximum" when the spins are "anti-parallel" (AFM). Therefore, J_{ij} has to be positive for FM to take place.

From the "Weiss field model", the relation between J_{ex} and T_c is given by

$$\frac{J_{ex}}{kT_c} = \frac{3}{[2zS(S+1)]} \tag{1.5}$$

here, z is "number of nearest neighbours".

The direct exchange is not feasible because the magnetic exchange forces in metal oxides are conciliating through the oxygen atoms. The 90° and 180° cation-anion-cation SEs are two significant coupling interactions. The orbital of anion mediates the exchange, and the "cation-anion-cation" bond angle is either 90° or 180°, therefore, the particular name has been adopted. The coupling produces different sorts of magnetic ordering depending on the nature of the e_g orbitals of cations (assuming an octahedral crystal field). AFM alignment occurs when both $t_{2}g$ are half full, whereas FM alignment occurs when one $t_{2}g$ is half-filled, and the other is empty. The Goodenough-Kanamori rules indicate the presence of SE interactions.

1.3.2 Double exchange

A sort of magnetic exchange that may occur between ions with different oxidation is termed as the DE. This mechanism was first formulated by "Zener" [23], predicts the relative ease with which the charge carrier may be moving between two ions and has substantial effects for the materials, if they are FM, AFM, or spiral magnetization [24]. Consider the Mn-O-Mn 180-degree contact, in which the Mn "e_g" orbitals engage directly with the O "2p" orbitals, and one of the Mn ions has more electrons than the other.

1.3.3 Superexchange

The strong (typically) AFM interaction between two immediate neighbor ions via a "non-magnetic anion" is known as SE, or Kramers—Anderson SE. In this regard, it differs from the direct exchange, where the nearest neighbor cations are coupled without the presence of other anion. SE occurs when electrons (e) from the same donor atom are connected to the spins of the receiving ions. The interaction can be FM if the two neighboring atoms are coupled at 90^o to the bridging "non-magnetic anion".

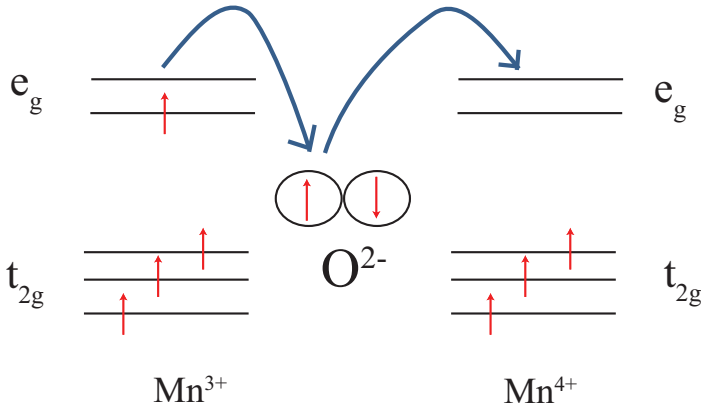

FIGURE 1.1: Schematic representation of "double exchange" interaction in manganites [25].

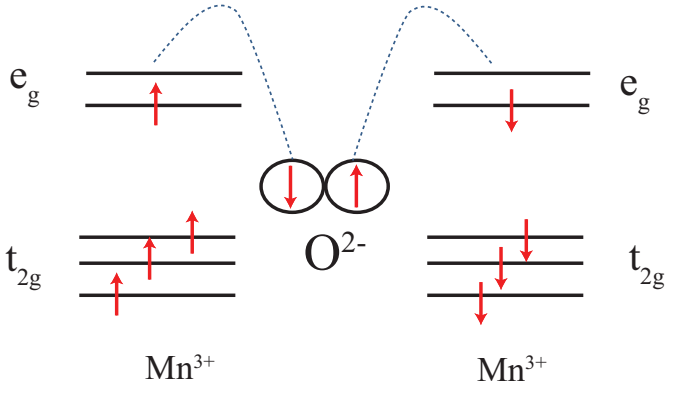

FIGURE 1.2: Schematic representation of " double exchange" interaction in manganites [26].

The different exchange interactions results in different magnetic properties as stated below:

1.4 Static magnetic property

1.4.1 Magnetic Anisotropy

Magnetic anisotropy, a critical characteristic feature of magnetic materials, has a large effect on the magnetic properties of materials. This term simply says that the measuring direction has an impact on magnetic properties. Magnetic anisotropy includes "crystal anisotropy, shape anisotropy, stress anisotropy, and exchange anisotropy" [27]. "Anisotropy" also happens because of "magnetic annealing", "plastic deformation", and other mechanisms. The only anisotropy in the material is the crystal anisotropy, which favors the magnetization to orient in a preferred direction i.e, easy magnetic axis or magnetically favored axis. As the applied magnetic field (H-field) acts against the "anisotropy force" to deviate the M from the easy direction, each material having M oriented in the non-easy direction must have stored energy in it. The amount of energy required to turn the M from a favored or "easy" direction to a "hard" one is known as anisotropy energy [22]. In other words, crystal anisotropy is a force that binds M to the orientations of certain crystal forms. The interaction between the "mean exchange field" and the "orbital angular momentum" of the atoms (ions) in the lattice is the physical source of magnetic anisotropy energy. This interaction is referred to as "spin-orbit coupling". If M produces angles a, b, and c with the crystal axes in a cubic crystal, and "α_1, α_2, and α_3" are cosine angles, hence, the "anisotropy" is given by:

$$E = K_0 + K_1\alpha_1^2\alpha_2^2 + \alpha_2^2\alpha_3^2 + \alpha_3^2\alpha_1^2 + K_1(\alpha_1^2\alpha_2^2\alpha_3^2) + ... \tag{1.6}$$

where K_0, K_1, K_2, ... are constants for a given system and are conveyed in erg/cm^3. The higher-order powers of K are rarely required, and K_2 is sometimes so small that terms involving it can be ignored. The "hexagonal" c-axis is the direction of easy M in hexagonal crystals, and any direction in the basal plane is equally hard. As a result, the "anisotropy energy" (E) is determined by angle between the M and the "c-axis",

$$E = K_0 + K_1 sin^2\theta \tag{1.7}$$

1.4.1.1 Magnetocrystalline Anisotropy (MCA)

MCA is a characteristic of ferrimagnets that exists regardless of particle size or shape. Measuring M curves in various crystal orientations is the most simple way to see it. The M approaches saturation at various fields based on the "crystallographic orientation" of the sample in an applied H-field. The cross-talking of the spin moment with the crystal lattice contributes to the "easy" and "hard" directions (spin-orbit coupling). The magnetic anisotropy is the consequence of individual magnetic cations'

collective contributions [22]. The potential issues from "domain wall pinning" and mobility do not occur in nano scale materials having a single magnetic domain. As a result, magnetic coupling at individual lattice sites may be directly linked to magnetic features like superparamagnetism (SPM). In ferrites, like CFO, the metal cations reside the "tetrahedral" (A-site) and "octahedral" (B-site) lattice positions in a cubic spinel crystal. Because the ligand field in spinel ferrites is weak, all cations adopt "high spin states". In a weak ligand field, the orbital angular momentum of a Fe^{3+} cation with a "$3d^5$" *e* configuration is normally quenched. As a result, only the Co^{2+} cations in CFO should contribute to the magnetic anisotropy. In CFO, a "Co^{2+}" cation having a "$3d^7$" *e* configuration at a B-site possesses a triplet "$4t_{1g}$" "ground state" [2]. Despite the fact that the "trigonal" field arises with the "t_{1g}" ground state dividing into "A_2" and "E_g", the "Co^{2+}" cation with a "degenerated ground state" of "E" is regarded as a "strong L-S coupling" and thus gives significantly to the "magnetic anisotropy" of CFO [28].

1.4.1.2 Uniaxial Anisotropy

"Anisotropy" is the distribution of an energy level on a specific direction. If the "magnetic moments" in a system are oriented in one of the direction, the material is said to have "uniaxial anisotropy", such as cobalt [27]. The crystalline nature of the materials dictates this kind of anisotropy. In "uniaxial anisotropy", the energy corresponds to the angle to a single axis [22].

$$E = K_1 sin^2\theta + K_2 sin^4\theta \tag{1.8}$$

here, E is "anisotropy energy", K_1 and K_2 are the anisotropic constants and θ is the angle, between M and crystal planes.

1.4.1.3 Shape anisotropy

There is another type of magnetic interaction that is relatively weak yet vital, in addition to the powerful and short-range exchange interactions. The equilibrium M of these interactions is anisotropic, which means it has preferred orientations. The magnetic dipole interaction is the first and most important of these weak interactions. The dipole interaction occurs because each atom in a magnetic substance has a dipole moment, causing the atoms to interact as an array of magnetic dipoles, as shown by

$$E_{dipole} = \frac{1}{2}\Sigma\frac{(m_i.m_j)r_{ij}^2 - 3(m_i r_{ij}^2)(m_j r_{ij}^2)}{2} \tag{1.9}$$

where, r_{ij} is the vector connecting any two dipole moments m_i and m_j in the system. Since the internuclear axes of a thin film are preferably pointed in the plane of the sample, the "dipole energy" is minimised for an in-plane magnetic moment direction. In the case of bulk samples, the "dipolar field" may contain the following three

contributions: (i) spherical volume, (ii) surface of the sphere and (iii) demagnetizing field [16]. The microscopic component is made up of contributions from "atomic dipoles" on the actual lattice sites within a spherical volume, as well as "pseudo-charges" on the sphere's periphery, and the macroscopic component is made up of contributions from the demagnetizing field generated by "pseudo-charges" on outer surface of the material samples.

1.5 Dynamic magnetic property

1.5.1 Magnetization dynamics and "Landau-Lifshitz-Gilbert equation"

The time-dependent M variations can take place on a variety of time scales. The interaction energies (E) define the time scales (t) via the Heisenberg relation $t = h/E$, where h is Planck's constant. The basic exchange interaction, which happens in 10 fs, is the quickest process. On a time scale of 10 fs-1ps, the "spin-orbit coupling" and "spin-transfer torque" happens. Within a few hundred fs, laser-induced ultrafast demagnetization occurs. Following rapid demagnetization, the quick re-magnetization time ranges from 1 to 10 ps. Magnetic writing happens over a time range of a few ps to a few 100s of ps, while "vortex" core reversal happens over a time scale of a few 10s of ps to ns. The M precession happens in the range of a few ps to a few 100s of ps, whereas M precession damping takes place in the range of sub-ns to 10 ns. The domain wall motion is the slowest process, with a time scale spanning a few nanoseconds to 100s of milliseconds. The different interaction energies discussed are based on the minimization of a FM substance's free energy. This allows one to determine the equilibrium configurations for a magnetic item without having to describe how M achieves equilibrium during this time. However, Landau and Lifshitz (1935) proposed a theory of FM body and predicted an equation of motion describing M precession that took into account all interactions. Gilbert (1955) changed the Landau-Lifshitz equation by replacing the original damping term with a dimensionless Gilbert damping term. From a mathematical and physical standpoint, the "Landau-Lifshitz-Gilbert (LLG) equation" is an interesting nonlinear evolution equation

$$\frac{\partial \mathbf{M}}{\partial t} = -\gamma \left(\mathrm{M} \times \mathrm{H_{eff}}\right) - \frac{\alpha}{M}\left(\mathbf{M} \times \frac{d\mathbf{M}}{\mathrm{dt}}\right) \tag{1.10}$$

.

It has to do with the dynamics of a variety of significant physical systems, including FMs. Due to orientation of spin, as well as the type of interactions, it can accept a wide range of dynamical structures, including spin waves. The "spin torque effect" in nanoferromagnets is now characterised by an extension of the "LLG equation", which is a fundamental dynamical equation in the area of "spintronics" [29].

1.6 Aims of the present work

1.6.1 $CoFe_2O_4$ (CFO)

Due to its tremendous practical value as well as a scientific curiosity, the study of spinel ferrite magnetic nanoparticles has attracted a lot of interest during several decades. The CFO is a versatile magnetic material that has been regarded as a viable contender. It is a member of the spinel ferrites family. Furthermore, due to its excellent inherent properties such as strong MCA, high H_C (5400 Oe) at RT, moderate M_S (80 emu/g), high T_C, and high "chemical and thermal" stabilities, CFO has opened the door to the development of novel potential applications. Because of these features, CFO has become increasingly popular in recent decades for more applications. The CFO is a face-centered cubic inverse spinel structure with the $Fd\bar{3}m$ space group, with Co^{2+} ions always present at "octahedral" (B) sites and Fe^{3+} ions evenly distributed between "tetrahedral" (A) and "octahedral" (B) sites. Because of its unique electrical and magnetic characteristics, CFO nanoparticles display a variety of novel and fascinating phenomena compared to their bulk counterparts. The greater number of atoms at or near the surface of the particles above those in the interior of the particles when particle size drops to a certain critical size. This has an impact on the nanoparticles' physical and chemical characteristics. The creation of novel materials has fueled the advancement of magnetic nanoparticles at ever-smaller length scales.

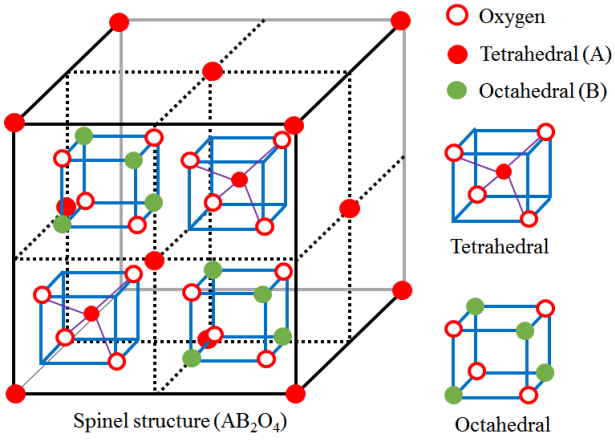

FIGURE 1.3: Schematic representation of spinel ferrite structure [30]

1.6.2 $La_{0.7}Sr_{0.3}MnO_3$ (LSMO)

The large bandwidth manganites such as LSMO has a high T_C for a wide doping range. For a small doping leads to a canted antiferromagnetic insulating (AFMI) phase in the parent material $LaMnO_3$, which is comparable to AFM under high H-fields. This doping range also features phase separation, which is made up of FM and AFM phases. Between the canted insulator and the ferromagnetic metal (FMM) phase, the ferromagnetic insulator (FMI) phase exists in a restricted range. At high

temperatures, the paramagnetic insulating (PMI) phase appears at $x = 0.25$, which is unexpected because it is normally associated with metallic conductivity. This phase transitions to FMM at lower temperatures, and when $T > T_C$, a paramagnetic (PM) metallic phase arises with increasing doping. The A-type AFM insulating phase appears when x > 0.5. Due to C-type AFM ordering, the system becomes an insulator. The C-type AFM order is made up of antiferromagnetically ordered planes with ferromagnetically connected magnetic ions. Because the tolerance factor has such a strong influence on crystal structure, LSMO shows numerous structural phases as x increases, from orthorhombic to rhombohedral to tetragonal to cubic. The hexagonal phase is stabilised when $x > 0.8$ and the tolerance factor > 1.

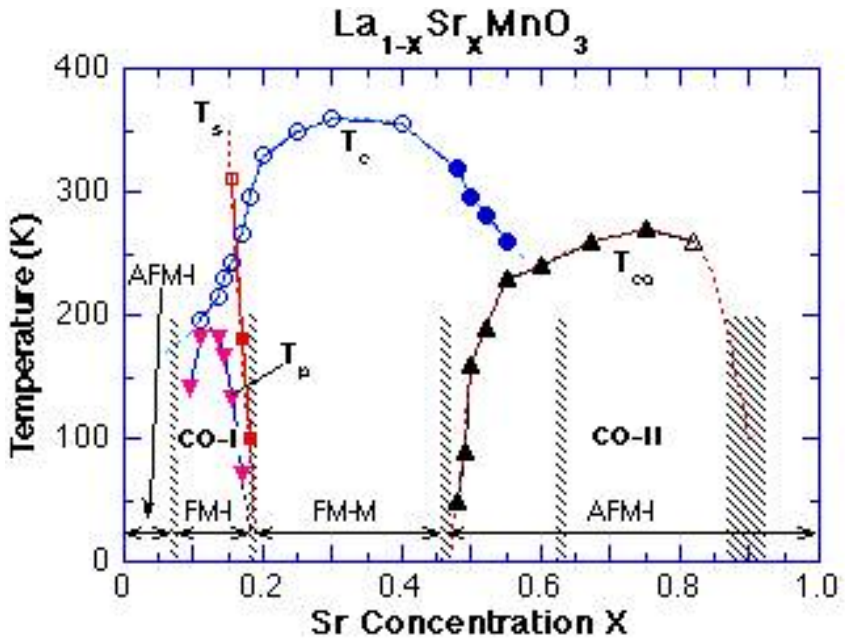

FIGURE 1.4: Phase diagram of $La_{1-x}Sr_xMnO_3$. AFM-I denotes antiferromagnetism insulator; CO denotes ordering; FM-I ferromagnetic insulator; FM-ferromagnetic metal
[31]

1.6.3 Literature review

Magnetic materials show an interesting anisotropic property when the particle sizes are reduced to the nano level. Magnetic anisotropy of CFO has been a fascinating field of study. Furthermore, at nanoscale length, magnetic materials display distinct competing "magnetic interactions" driven by extraneous influences, such as "size" and "shape", resulting in M switching process which will be different for different particles. Due to its significant MCA, increased H_C, and mild M_S, CFO was found as a good material for the indicated purpose among the ferrites.

The oxygen atoms have a face-centered cubic atomic structure, with Fe^{3+} and Co^{2+} occupying the tetrahedral (T_d) and octahedral (O_h) sites, respectively. Because of their structure, magnetic spinel nanoparticles are particularly intriguing. It is

possible to adjust the magnetic properties (e.g., MCA and M_S) of the two sublattices by varying the cation distribution between them. Magnetic characteristics can be influenced by changes in chemical composition, processing methods, and thermal treatments. The magnetic properties of spinel ferrite nanoparticles are greatly influenced by the presence of a "non-collinear" spin structure (i.e., "spin canting"). The "spin-canting" is caused by competing interactions between sublattices, as revealed by polarised neutron scattering and Fe^{57} Mössbauer investigations. The topology of surface magnetic moments and, as a result, the exchange integrals (through SE angles and/or distances between moments) are altered, resulting in a change in surface anisotropy. Surface disorder, cationic dispersion, and spin canting are the most important processes in ferrite nanoparticles with a spinel structure; therefore, their magnetic properties are the consequence of a complicated interplay of several processes [32].

Ortega et al., Martinetz et al., etc., studied the magnetic behavior of varying sized CFO nanoparticles having different morphology for permanent magnet-based application [33–35]. Shape-controlled nanoparticles of CFO have also been studied by Kumar et al. for the purpose of humidity sensing application [36]. Both these studies have opened up possibilities to explore the particle size and shape-dependent magnetic behavior in a systematic way with temperature as the defining parameter.

Similarly, thickness-dependent anisotropic studies have become a topic of interest in thin films of CFO in analogous to nanoparticle magnetic anisotropic behavior. Some other grows have shown the variation of "magnetic anisotropy" with the change in thickness [37]. In-plane and out-of-plane magnetization has been studied with the variation of the substrate by Dhakala et al. with the incorporation of "buffer layer" in Gao et al. Raghunathan et al. studied the effect of substrate temperature on anisotropy in CFO films deposited on SiO_2/Si(100), finding that the anisotropy decreased as the substrate temperature decreased [23, 38, 39]. A variety of factors can cause magnetic anisotropy. It can be caused by the crystal structure, such as crystallographic roughness, internal stress or strain, or the specific form or arrangement of particles, and any of these factors can become dominant under certain conditions. Apart from "intrinsic" anisotropy, the "extrinsic" one such as shape, stress, etc. are greatly improved in reduced symmetry systems such as thin films; they compete with each other and may result in anisotropy. Realizing the root causes of "anisotropies" and its "engineering" is, therefore, critical for their device application.

In the case of LSMO, the high T_C and high spin polarization make it a suitable material for RT applications [30]. Low magnetic damping is preferable for applications in magneto-dynamic devices, and having well-specified magnetic properties while the material is in nanoscale dimensions is critical [40]. The magneto-dynamic damping is an excellent phenomena, which may be quantified via "FMR spectroscopy" through "resonance". The resonance peaks' linewidth is made up of two components: an inhomogeneous contribution that is independent of frequency and a dynamic part which is frequency and the "damping parameter" (α) dependent.

The less damping shows that LSMO is a viable material for use in magneto-dynamic devices. Typical FM metals have damping parameter, $\alpha = 10^{-2}$, and less value indicates that LSMO is a suitable material for magneto-dynamic devices [41]. A group has previously examined α of LSMO thin films deposited on STO, masked by a metal film, finding a damping value of $\alpha = 1.6\text{x}10^{-3}$ for a "20 nm" thick LSMO at RT [42].

1.6.4 Objectives of the thesis

With an aim to study the basic properties of anisotropic ferrite and manganite particles for the purpose of device applications, the present work was taken in hand. In view of the low-power consumption and heat-free technology applications, thin films of CFO and manganites were investigated mostly to find potential applications in magneto-electric ultra-low power consumption devices.

With the above-mentioned aims in mind, the present work was taken up. To achieve the aims, at first, CFO and LSMO nanoparticles were synthesized. The CFO nanoparticles were studied systematically in varying sizes and shapes. Structural and morphological variation of nanoparticles of LSMO had also been studied. The interesting properties of CFO thus obtained from the size and shape variation anticipated to reveal fascinating magnetic properties. Hence magnetization measurements were carried out on the CFO samples. The magnetic anisotropy obtained from these experimental results conveys that the obtained properties might be helpful for device applications. Further, to investigate the possibility of getting an ultra-low-power device-making material, the two-dimensional (thin film) form of both CFO and LSMO were deposited. The magnetic property measurements showed that both the materials are FM in thin-film form with high magnetic anisotropy.

1.6.5 Organization of the thesis

The present chapter briefly introduces CFO and LSMO and its important features. In addition, this gives scope of the different literature on the anisotropy of CFO and LSMO. It also gives a brief review of magneto-dynamic damping in manganite thin films used for the purpose of spin-wave devices.

Chapter 2 consists of a detailed description of preparative techniques of nano/bulk and thin films from CFO and manganite (LSMO). Wet chemical synthesis (sol-gel) was used to prepare both the nanoparticles of CFO and LSMO. Further target preparation for the purpose of thin-film deposition has also been mentioned in this chapter. This chapter also consists of the working mechanism and principles of the instruments used.

Chapter 3 consists of a detailed study of influence of particle size on CFO and LSMO nanoparticles. In this chapter, the structural and morphological properties of CFO and LSMO were studied. The samples were further studied for their magnetic properties.

Chapter 4 consists of a structural, morphological, and magnetic study of CFO thin films with varying thickness. The chapter explores the factor responsible for out-of-plane magnetic anisotropy observed in the varying thickness samples.

Chapter 5 consists of structural and magnetic anisotropy studies of LSMO thin films grown on single-crystal piezoelectric PMN-PT oriented along [001], [011] and [111] directions.

Chapter 6 states the magneto-dynamic studies of LSMO/PMN-PT heterostructures oriented along [001], [011] and [111] directions and explores the possibility of application in spin-wave devices by investigating the Gilbert damping constant for the films.

Chapter 7 summarizes the entire thesis and mentions the outcome of the work carried out.

References

[1] S. Singh, H. Chawla, A. Chandra and S. Garg, Elect. Optic. Mater. **25** 319 (2021).

[2] J. Morley, K. Widdicks and M. Hazas, Energ. Res. Soc. Sci. **38** 128 (2018).

[3] J. Puebla, J. Kim, K. Kondou and Y. Otani, Commun. Mater. **24** 1 (2020).

[4] T. Dippong, E. A. Levei and O. Cadar, Nanomaterials **11** 1560 (2021).

[5] R. Ramesh and N. A. Spaldin, Nat. Mater. **6** 56 (2007).

[6] G. Venkataiah, E. Wada, H. Taniguchi, M. Itoh and T. Taniyama, J. Appl. Phys. **113** 17C701 (2013).

[7] T. Taniyama, J. Phys.: Condens. Matter **27** 504001 (2015).

[8] A. Hirohata, K. Yamada, Y. N. Ioan-Lucian, P. Bernard, D. Philipp and P. B. Hillebrands, J. Magn. Magn. Mater. **509** 166711 (2020).

[9] P. K. Amiri and K. L. Wang, Spin **2** 3 (2012).

[10] K. Manju, T. Smitha, S. N. Divya, E. K. Aswathy, B. Aswathy, T. Arathy and K. T. Binu-Krishna, J. Adv. Ceram. **4** 199 (2015).

[11] E. Swatsitang, S. Phokha, S. Hunpratub, B. Usher, A. Bootchanont, S. Maensiri and P. Chindaprasirt, J. Alloys Compd. **664** 792 (2016).

[12] M. A. G. Soler, E. C. D. Lima, S. W. Silva, T. F. O. Melo, A. C. M. Pimenta, J. P. Sinnecker, R. B. Azevedo, V. K. Garg, A. C. Oliveira, M. A. Novak and P. C. Morais, Langmuir **23** 9611 (2007).

[13] A. R. Bueno, M. L. Gregori and M. C. S. Nobrega, Mater. Chem. Phys. **105** 229 (2007).

[14] Z. Ding , W. Wang, Y. Zhang , F. Li and J Ping-Liu, J. Alloy. Compd. **640** 362 (2015).

[15] A. T. Raghavender, Sci. Technol. Arts. Res. J. **2** 1 (2013).

[16] B. D. Cullity, C. D. Graham, Introduction to magnetic materials IEEE Press, (2009).

[17] C. Kittel, Introduction to Solid State Physics (7th ed.). New York, (1996).

[18] M. Sugimoto, J. Am. Ceram. Soc. **82** 269 (1999).

[19] R. Nongjai, S. Khan, K. Asokan, H. Ahmed and I. Khan, J. Appl. Phys. **112** 084321 (2012).

[20] N. Sivakumar, A. Narayanasamy, C. N. Chinnasamy and B. Jeyadevan, Phys.: Condens. Matter **19** 386201 (2007).

[21] M. Guillot, Magnetic Properties of Ferrites, Materials Science and Technology, Wiley-VCH, Intenses, C. N. R. S., Grenoble Cedex, France (2006).

[22] A. Aharoni, Introduction to the Theory of Ferromagnetism, Oxford University Press, (1996).

[23] C. Zener, Phys. Rev. **82** 403 (1951).

[24] M. Azhar and M. Mostovoy, Phys. Rev. Lett. **118** 027203 (2017).

[25] B. Bechlars, D. M. DAlessndro, D. M. Jenkins, A. T. Iavarone, S. D. Glover, C. P. Kubiak and J. R. Long, Nat. Chem. **25** 362 (2010).

[26] J. Kanamori, J. Phys. Chem. Solids. **10** 87 (1959).

[27] S. Blundell, Magnetism in condensed matter, Oxford University Press, (2001).

[28] Q. Song and Z. J. Zhang, J. Phys. Chem. B **110** 11205 (2006).

[29] M. Lakshmanan, Phil. Trans. R. Soc. A **369** 1280 (2011).

[30] W. Zhang, A. Sun, X. Pan, Y. Han, X. Zhao, L. Yu, Z. Zuo and N. Suo, J. Magn. Magn. Mater **506** 166623 (2020).

[31] H. Fujishiro, T. Fukase and M. Ikebe, J. Phys. Sco. Jpn. **67** 2582 (1998).

[32] A. Omelyanchik, M. Salvador, F. D'Orazio, V. Mameli, C. Cannas, D. Fiorani, A. Musinu, M. Rivas, V. Rodionova, G. Varvaro and D. Peddis, Nanomaterials **10** 1288 (2020).

[33] B. Martínez, X. Obradors, L. Balcells, A. Rouanet and C. Monty, Phys. Rev. Lett. **80** 181 (1998).

[34] J. M. D. Coey, Phys. Rev. Lett. **27** 1140 (1971).

[35] A. L. Ortega, E. Lottini, C. J. Fernandez and C . Sangregorio, Chem. Mater. **27** 4048 (2015).

[36] Y. Kumar, A. Sharma and P. M. Shirage, RSC Adv. **7** 55778 (2017).

[37] A. Lisfi, J. C. Lodder, E. G. Keim and C. M. Williams, Appl. Phys. Lett. **82** 76 (2003).

[38] M. Gao, R. Viswan, X. Tang, C. M. Leung, J. Li and D. Viehland, Sci. Rep. **8** 323 (2018).

[39] A. Raghunathana, I. C. Nlebedim, D. C. Jiles and J. E. Snyder, J. Appl. Phys. **107** 09A516 (2010).

[40] V. Flovik, F. Macià, S. Lendínez, J. M. Hernàndez, I. Hallsteinsen, T. Tybell and E. Wahlström, J. Magn. Magn. Mater. **420** 280 (2016).

[41] S. Yoshii, R. Ohshima, Y. Ando, T. Shinjo and M. Shiraishi, Sci. Rep. **10** 15764 (2020).

[42] G. Y. Luo, J. G. Lin, W. C. Chiang and C. R. Chang, Sci. Rep. **7** 325 (2017).

Chapter 2

Experimental methods

2.1 Overview

In this chapter, the preparation methods of nanoparticle, bulk, and thin-film samples and the measurement protocols of the instruments used for characterization and physical property measurements have been discussed in detail. The basic principles involved in measurements were discussed both quantitatively and qualitatively by suitable schematic representations.

2.2 Preparation

2.2.1 Preparation of nano and bulk samples: CFO

Metal-oxide nanoparticles behave differently as compared to their bulk counterparts, making it interesting to investigate. In this case, the CFO nanoparticle, because of its high H_C , moderate M, and great "physical" and "chemical" stability, makes it worth studying at nanoscale. Generally, for synthesizing polycrystalline nanoparticles, wet chemical sol-gel and solid-state reaction techniques are widely used. In the present investigation, the "sol-gel synthesis" technique was adopted to synthesize the samples: "low processing temperatures", "good homogeneity", exact control on stoichiometry, "simple experimental design", and "inexpensive apparatus" are the advantages of this method. The temperature at which synthesis was carried out is low; which is suitable for preparing nanoscale samples. The molecular-level mixing of the ingredients during the synthesis method results in high purity of the sample.

2.2.1.1 Polymeric method via thermal decomposition

The physical properties of magnetic nanoparticles are highly affected by their dimensions hence their synthesis must be carefully tuned to produce the acceptable "size-dependent" properties [1, 2]. The evolution of easy and repeatable procedures for producing nanoscale particles of Fe_3O_4 and its variants is critical [3, 4]. The polyvinyl alcohol (PVA) is widely utilised as a binder in the production of magnetic nanoparticles since it is a non-toxic polymer. The use of PVA to regulate the synthesis process results in Fe_3O_4 and transition metal doped Fe_3O_4 with exact chemical

stoichiometry and crystal structure, excellent size dispersal, and "chemical stability". The thermal breakdown using a polymeric approach was used to create CFO nanoparticles [5, 6]. A 10 % of PVA solution was produced by adding the polymer to hot water at 70 °C and stirring the mixture for 24 h. The reagent quantities were estimated based on the molar ratios of "10:0.333:0.666, PVA : $Co(NO_3)_2.6H_2O$: $Fe(NO_3)_3.9H_2O$", respectively. The $Co(NO_3)_2$ was mixed to the polymeric solution first, and then $Fe(NO_3)_3$ was added. The combined mixture was stirred continuously for 24 h at 70 °C and, after solvent evaporation, cast on a glass plate at ambient temperature to create a homogenous film [12]. The CFO sample was then ground to make a powder. A flowchart of the preparation procedure has been shown below:

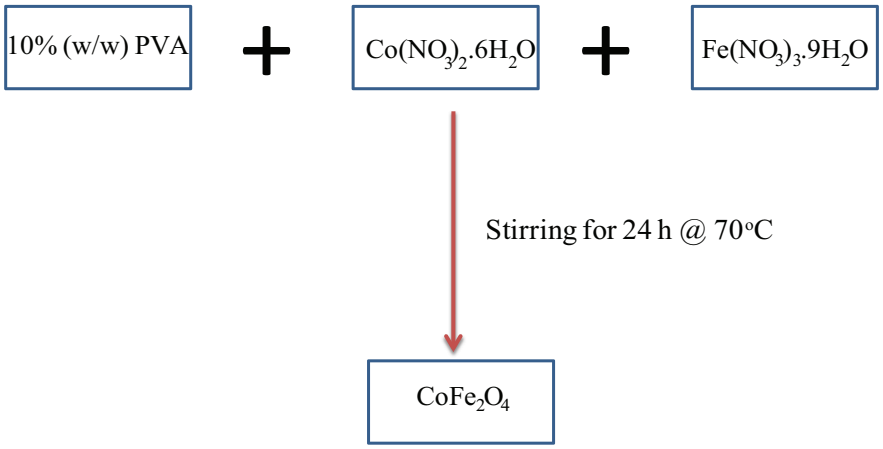

FIGURE 2.1: Flowchart of formation of CFO nanoparticles using thermal decomposition via PVA method.

2.2.2 Preparation of nano and bulk samples: LSMO

The LSMO was prepared by mixing an adequate amount of nitric acid with the starting precursor materials of metal oxides/carbonates/nitrates were created in stoichiometric proportions. To make it transparent, the converted nitrates were dissolved in doubly ionized water and thoroughly stirred. The metal nitrate solution was then treated with "citric acid" in a 1:1 "molar ratio". The pH of the mixture was setup at around 6.5-7 by mixing ammonia in order to speed up the reaction rate. This mixture was then heated on a hot plate in the range of 70 ° to 80 °C while stirring continuously. Following the slow evaporation of the mixture's water content, it resulted in a thick and viscous solution. A gelating agent, "ethylene glycol," was mixed in the ratio of 1:1.2 of the metal atoms that are existing in the solution. Further, heated at 160 °C to 180 °C on a magnetic stirrer with constant mixing to produce a thick gummy gel and this was ground and fired on a "Bunsen burner" to produce a black "fluffy porous mass". The obtained compound was pre-sintered at 700 °C for 4 h to make "single-phase material", and it was made into pellets; finally sintered at various sintering temperatures to obtain samples with varying particle sizes. The preparation procedure is depicted in a flowchart below:

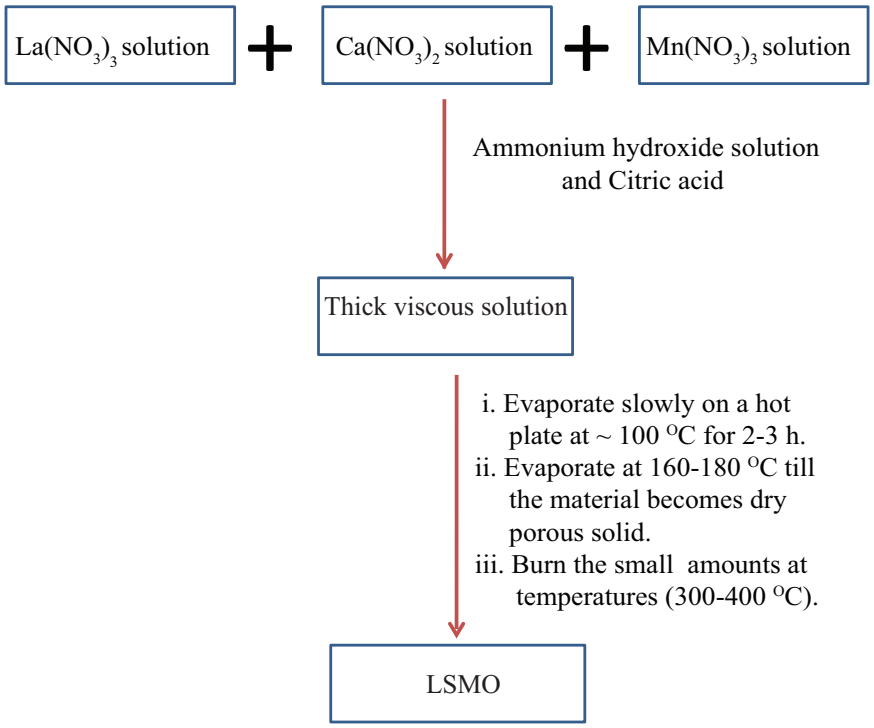

FIGURE 2.2: Flowchart for synthesis of LSMO using sol-gel method.

2.2.3 Preparation of PLD target: CFO

The CFO target for PLD has been prepared by thermal decomposition via the PVA method. The CFO targets used in the present investigation were made from $Co(NO_3)_2.6H_2O$ and $Fe(NO_3)_3.9H_2O$, respectively. The nitrates were dissolved in deionized water in a stoichiometric ratio of 1:2. After that, "citric acid" was added and then mixed properly at 60 °C for 1 h. For 24 h, the gel was dried. The obtained precursor was heated for 1 h at 400 °C.

The powder was molded up to about the same particle size and pressed onto a 25 mm and 5 mm diameter disc. The disc was sintered in the oven. The method comprised of three steps, 4 h and 100 °C, 4 h and 500 °C, 6 h at 1300 °C, ramping at 3 °C/min. Then it was steadily cooled to RT AT 3 °C/min. The density of the target was estimated and found to be 90 % compared with its theoretical density [20].

2.2.4 Preparation of PLD target: LSMO

The LSMO target was prepared using citrate-based sol-gel method. The LSMO target used in this study was synthesized from the corresponding metal nitrates. High purity chemicals were taken for the initial materials. The stoichiometric ratios available oxide and carbonate compounds were converted into their corresponding nitrates by mixing nitric acid and were with water to convert it into clear solution. The "citric acid" has been mixed with metal nitrates in a 1:1 molar ratio and pH value is adjusted at around 7 by adding ammonia solution. Then, the solution was allowed for evaporation to get a "sol", "ethylene glycol" was added, followed by firing to get

initial powder. The powder was sintered 1350 °C for 12 h to get bulk polycrystalline samples [20].

2.2.5 Thin films (PLD)

The PLD has been widely employed for growing oxide-based thin films since the 1960s. Smith and Turner were the first to use the ruby laser to grow thin films on semiconductors, dielectrics, and organo-metallic materials [8, 9]. The PLD is more popular due to its usage for many material preparations [10, 11]. It was heavily used for successfully developing high-temperature superconductor films [12]. The PLD is incredibly basic, both conceptually and practically, and is perhaps the simplest of all thin-film growing methods [13]. The PLD is, in essence, a laser-based sputtering technique. The main components are depicted in the schematic diagram. The most notable feature of PLD is its ability to cater to the appropriate stoichiometry in complex compounds [1, 9, 12].

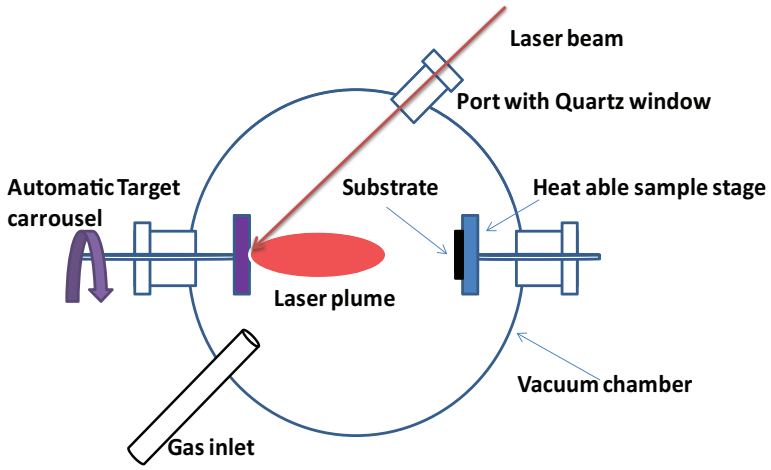

FIGURE 2.3: Schematic representation of PLD chamber and its deposition geometry.

2.2.5.1 Working principle

The PLD operations are based on the vapor pressure coming by the laser; the removal of the target surface leads to the formation of plasma that is deposited on the substrate. However, there are several growth parameters that must be considered, resulting in PLD being a complicated preparation technique. This method employs high-power laser pulses that pass on to the optic to fall on to the target in the chamber. This powered beam immediately raises the target's surface temperature to 2000-3000 °C. The laser beam is focussed onto the target's surface in the first stage. The constituents of the target's surface are swiftly heated when the energy density is sufficiently high, and the pulse length is sufficiently short. The material is separated from the target and ablates with same composition of the target. The rate of

immediate ablation is strongly dependent on the fluence of the laser that is irradiating the target. Many complicated physical processes, such as "collisional", "thermal", "electronic excitation", "exfoliation", and "hydrodynamics", are involved in ablation process. The released plume migrates towards the substrate as per the gas-dynamic principles [14]. Zhang et al. discovered that the spatial thickness is going to be changed as per cos(nϕ), where n$\gg$1 [15]. The size of the laser spot and the temperature of the plasma both have a major impact on the homogeneity of the deposited layer. Another characteristic that controls the angular spread of ablated materials is the target-to-substrate distance. The third stage is critical for determining thin film quality. The expelled high-energy species impact the substrate surface, causing various types of damage. These species expel some of the surface atoms, resulting in the formation of a collision zone between the incident flow and the sputtered atoms. The film begins to develop soon after the thermalized zone (collision region) forms. The area acts as a particle condensation source. The PLD technology consists of two main processing systems for the thin films, namely the loading chamber and the laser pulsing. The substrate and the aim are kept in the vacuum chamber while the film is growing. This guarantees that the expulsed substance does not contact with air and the deposition on the substrate of undesirable species. The turbo-molecular pump and rotary pump for the deposition chamber are utilized to achieve a high vacuum. Both pumps work as a single unit; the rotary pump is used as a backup pump in order to bring chamber pressure down from 10^3 Torr to high vacuum [11]. The optical components include a convex focusing lens, a window, and an opening. An aperture's role is to define a laser pulse's form and to provide the laser with highly homogenous energy distribution. In general, an optical system's efficiency is roughly 30%. The optics must be clean to guarantee the least loss of laser energy.

2.2.5.2 Growth of the film

In general, there are three kinds of film growth mechanisms that depend on the parameters, namely, the grids at the substratum and film interface, film surface energy, and interfacial energy [16]. Below are the growth modes:

- 3-D "island growth" – "Volmer-Weber growth"
- 2-D "full-monolayer growth" - "Frank – van der Merwe growth"
- 2-D "full-monolayer growth" followed by 3-D islands growth - "Stranski-Krastinov growth".

The standard of the film depends on the essential parameters, such as substrates, the temperature of the substrate at the time of film growth, etc. The different growth parameters can be tuned for achieving a good quality film [17, 18]. The PLD setup used to generate the thin film samples from the present study is presented in Figure 2.4.

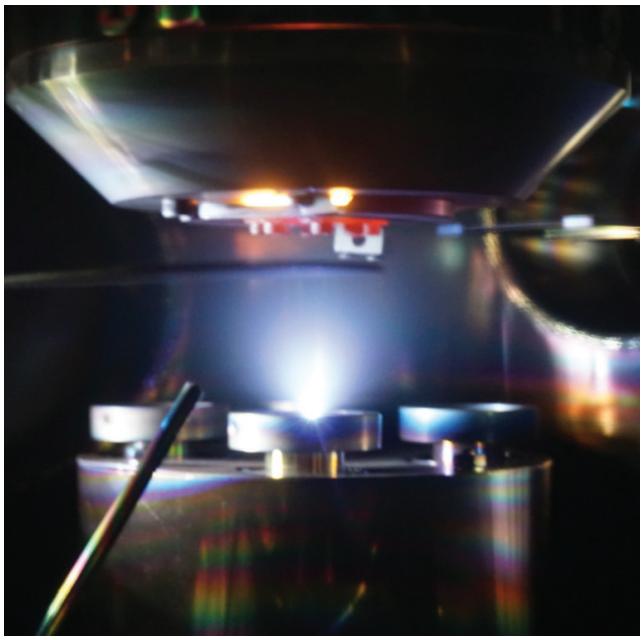

FIGURE 2.4: Inside view of PLD chamber during the growth process.

2.2.5.3 Deposition of CFO thin films

The Platinum coated both sided polished Silicon substrates having orientation along [111] direction were cleaned by "ultrasonic cleaning" with acetone and ethanol, then washed with double distilled water and then dried with nitrogen gas. The chamber's base pressure was kept at 2×10^{-7} Torr before each deposition was performed. With a focusing lens to the rotating CFO target the energy density was determined to be 1.5 J cm^{-2}; here the laser beam is KrF excimer (300 mJ, 248 nm wavelength). The laser repetition rate was regulated to 5 Hz, 4 cm was the distance between target and substrate. Following an advanced temperature profile, the substrates have been heated. The temperature of the substrate was varied between ambient temperature (27 °C) and 550 °C. When the substrate achieved the correct temperature, the working gas oxygen was supplied into the chamber via the nozzle by adjusting the needle valve of "turbomolecular pump". The thickness of the films was altered in this study. Immediately after the growth, the films were in-situ sintered at 650 °C and progressively cooled to room temperature over several hours at the same working oxygen partial pressure. When the temperature dropped below 60 °C, the substrate was removed from the chamber.

2.2.5.4 Deposition of LSMO thin films

An oriented LSMO (50 nm) was grown on single-crystal PMN-PT oriented along [001], [011] and [111] by using "PLD technique" with an "Nd: YAG laser" (λ = 532 nm). The preparation of LSMO was undertaken after achieving a base pressure of 3 x 10^{-8} Torr, with the pulse frequency of 10 Hz, maintaining deposition at 650 °C in 100 mTorr of "O_2" pressure.

2.3 Characterization

2.3.1 Structural : XRD

The wavelength of x-rays is in the range of 0.02 - 100 Å. Because of its small wavelength, the x-rays can penetrate deep into the lattice, as it matches the crystal plane distance and gives the material's structural information. It is a non-destructive analytical tool used to recognize the degree of crystallinity in materials. As shown in Fig. 2.5, the interaction between e and x-rays is detected in the form of reflection of "x-rays" by "crystal lattice planes" [22]. As the diffractive spacing plane(s) (d_{hkl}) is of the order of the wavelength of x-rays, (λ) in which the reflection typically occurs at a given "diffraction angle" (θ_{hkl}); the governing "Bragg equation" is,

$$2d_{hkl}sin\theta_{hkl} = n\lambda \tag{2.1}$$

The crystal structure can be obtained from the measured diffraction patterns. This technique has constructively interfered with monochromatic rays diffracted from the material. When Bragg's diffraction condition is achieved, constructive interference takes place. By scanning the sample with x-rays across the whole 2θ-angle range, it is easy to obtain all planes in the unit cell that meet the division peaks by means of powder samples because of the different d_{hkl} ranges available for x-rays to fulfill the Bragg's condition. The main characteristics of XRD are: (i) 2θ: the division angle of Bragg is linked to interplanar distance (d_{hkl}) for a fixed wavelength. Indeed, d_{hkl} depends on the unit cell dimensions. (ii) intensity: normalized peak intensity will depend on the number and arrangement of atoms in assigned lattice planes and incident reflecting primary x-ray beam [22]. The phase development of prepared manganites was confirmed in this case by using a "Phillips Expert diffractometer" with "Cu-Kα radiation (λ = 1.5405 Å)" source to measure XRD data at room temperature. The data were gathered in the range of 2θ ($20^\circ < 2\theta < 80^\circ$) with an interval of 0.05° and a scanning rate of 5°/min. Rietveld's technique of refinement with FULLPROF software [23] analyzed these data subsequently. The following is a brief schematic representation of the technique.

2.3.1.1 Rietveld analysis

A full-profile approach to the refining of neutron diffraction data was initially introduced in the Reitveld process. H. M. Rietveld demonstrated that powder neutron diffraction data might be used to accurately determine crystal and magnetic structures [24]. As a result, this method was used to analyze powder XRD data. The primary premise of this technique is to use theoretical calculations to compare experimental data with estimated XRD patterns. The least-square fitting algorithm is used in this method, which aims to reduce the error between "theoretical estimation" and "experimental data". The divergence is quantified by [25]

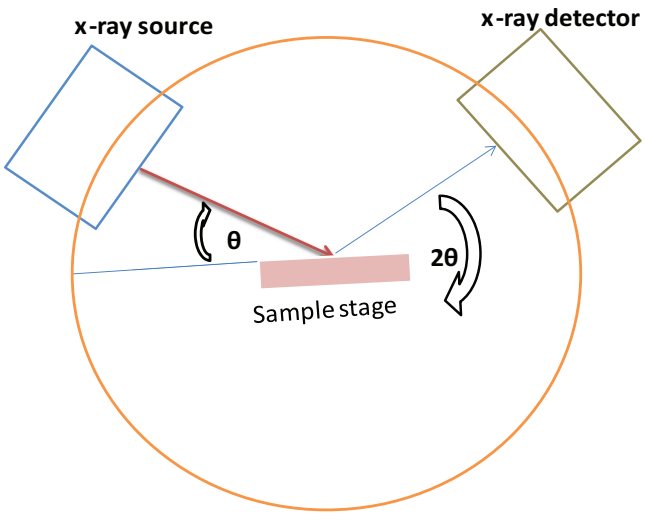

FIGURE 2.5: Schematic representation of x-ray diffractometer in θ-2θ geometry.

$$S_y = (y_i^{Obs} - y_i^{Cal})^2 w_i \tag{2.2}$$

where, w_i represents the "statistical weight" of the i^{th} point, y_{obs} depicts the whole obtained i^{th} point intensity. The final intensity y_{cal} at the point (i^{th}) is:

$$Y_i^{Cal} = Aps\eta \sum P_{hkl} L_{hkl} F_{hkl} (\theta_{hkl} - \theta_i) + b \tag{2.3}$$

The parameters "A, b, s, p, and η" correspond to the experiment's absorption, background noise, scale-factor, polarisation, and extinction, respectively. The "geometry" and "preferred orientation" characteristics are represented by L_{hkl} and P_{hkl}, respectively. These terms and parameters may be changed systematically throughout refinement cycles to increase the similarity between the estimated and experimentally acquired diffraction patterns. The evaluation process can include many numerical parameters to determine the refinement's quality. During the refining process, "unit cell", "background", "peak profiles", "scale", FWHM, "occupancies", shape, and atomic positions are systematically and frequently modified in a sequential way until the best feasible match is achieved. "Goodness of fit" (χ^2) confirms the best-fit patterns, and the corresponding best-fit phrases are expressed as:

$$R_p = \frac{\sum y_i^{\text{obs}} - y_i^{\text{cal}}}{\sum y_i^{\text{obs}}} \tag{2.4}$$

$$R_{\text{wp}} = \sqrt{\frac{\sum \left(y_i^{\text{obs}} - y_i^{\text{cal}}\right)^2 . w_i}{\sum w_i (y_i^{\text{obs}})^2}} \tag{2.5}$$

$$R_{\text{exp}} = \sqrt{\frac{N - P}{\sum w_i (y_i^{\text{obs}})^2}} \tag{2.6}$$

$$\chi^2 = \frac{\left(R_{\text{wp}}\right)^2}{\left(R_{\text{exp}}\right)^2} \tag{2.7}$$

For the best-fit patterns, it is to be noted that "R_p " ("pattern"), the "R_{wp}" ("weighted pattern") and "R_{exp} " ("experimental") values are to be as low as possible. The typical agreeable range of goodness of fit, χ^2 is < 5 for the software code engaged in the present study.

2.3.2 Structural : Raman spectroscopy

"Raman spectroscopy" is a non-destructive, surface-sensitive spectroscopic approach for determining crystallinity, stoichiometry, and phase transitions, among other things. The Raman spectrum is the sample's fingerprint and provides information about its chemical makeup. The Raman spectra of two phases of the same substance cannot be the same; therefore, they can be discriminated easily. Raman spectra are also not affected by the frequency of incoming light. Because the intensity of light is proportional to the number of excited molecules, it also provides data about atomic contents. This technique is based on monochromatic light's molecular vibrations (laser light). Rayleigh scattering occurs when the monochromatic coherent light is shone. A tiny portion of the dispersed light follows a frequency shift away from the source frequency. The "vibrational interaction" of laser light with the molecule causes this change. The Raman spectrum is obtained by plotting the shifted light intensity against the frequency of the source light. Both sides of the "Rayleigh frequency", the shifted frequency might exist. Strokes lines are lower frequency-shifted lines, whereas anti-strokes lines are higher frequency-shifted lines.

The advantages of Raman spectroscopy are: (1) "sample preparation" is not required, (2) "nondestructive technique", (3) can be done for "solid", "liquid" or "gas" samples, (4) less "measurement time", (5) analysis of the aqueous system, and (6) gives "quantitative" and "qualitative" data of the sample.

2.3.2 Morphology : FESEM

Using a FESEM, the grain morphology and its development in the samples were studied. EDX analysis, which was attached to the FESEM, was used to check the composition of the elements.

The grains and surface morphology are imaged using an electron beam in the FESEM technique. The applied electric field accelerates the energetic electrons from the source. Furthermore, the electrons are focused into a narrow beam by the electromagnetic lenses which scatter with the sample [26]. Different types of signals created by electron-sample contact can be used to extract microstructural information. The basic notion of "inelastic scattering of secondary electrons" and subsequent imaging is used in this device. Following scattering, the electrons are recognized and transformed into an electrical signal. The collected signal is enlarged, attributed as an

image to be seen on the screen of the computer system. For insulating samples, they must first be made conducting in order to avoid the accumulation charges onto the sample's surface and obtain a good image utilizing a FESEM. This can be accomplished by depositing a thin coating of gold/platinum (1.5- 3.0 nm) on the surface of the sample. The samples must be extremely stable under vacuum in order for physical attributes to remain unaffected by the loss of moisture or gases during the procedure. The method provides data on surface morphology such as microstructure, grain dimensions and shape, voids, and so on. The FESEM pictures used in this study were acquired with a Carl-ZEISS Make (Model no. ULTRATM-55). Figure 2.6 shows a photograph of the FESEM system used for measurements. To increase conductivity, the samples were wrapped in carbon tape and coated with gold.

FIGURE 2.6: Photograph of field emission scanning electron microscope

2.3.3 Energy dispersive x-ray (EDX) spectroscopy

The compositional analysis is performed using EDX spectroscopy. The FESEM has the EDX system as a standard feature. The sample is exposed to a high-energy electron beam during the study. When electrons interact with the material, the inner shell electrons of atoms are knocked off. High-energy electrons then take over the empty places from the outer shell. Here, the electron has to give up a part of its energy in the form of radiation by producing x-rays during the transfer process. The

produced x-rays can fingerprint the atomic structure of individual atoms because of their different atomic structure. The composition of the sample can be determined by examining the properties of x-rays obtained from it [27].

2.3.4 Microstructure Analysis : High resolution transmission electron microscopy (HRTEM)

The HRTEM was used for the microstructural examination. This approach can reveal information about the size, shape and crystallinity of the particles.

The TEM is considered to be an efficient and ultimate tool for estimating the nanoscale materials' particle size. The morphology, crystallography, and composition of samples can all be determined by TEM characterization. In particles, this comprises their shape, size, atomic spacings, orientations, defects, and so on. Additionally, EDX analysis can be used to verify the composition of nanometer-scale particles. The electron beam that collided with the material was split into three beams: transmitted, backscattered, and absorbed electrons. The first beam divides into three groups of (i) directly transmitted electrons: samples with a small change of direction as well as energy; (ii) electrons with elastic dispersion: atomic interactions preserving energy change in the direction; and (iii) electrons with a small inelastic change in the direction: directional changes and energy decline. The TEM image contrast depends on the proportion of electrons that are dispersed directly and elastically. The contrast is determined by mass density and reflections by Bragg on amorphous and crystalline samples. The sample must be prepared accordingly, given that the electron must transmit the samples for HRTEM technology. The preparation for TEM samples is a somewhat complex, and the below mentioned steps have been followed in this study. (1) To achieve a homogenous solution, the powdered materials were thoroughly mixed in ethanol and ultrasonicated for 10 minutes. (2) Later, a few drops of the solution were gently placed over carbon-coated copper grids. (3) The grid was dried at in an oven and prepared for TEM microstructure investigation.

A photograph of the TEM instrument used for the experiment is shown below.

2.3.5 Magnetic Force Microscopy (MFM)

The MFM is an imaging method based on atomic force microscopy. To study the magnetic orientation of the CFO thin film, MFM measurements have been carried out. In MFM, a sharp magnetic tip travels across a sample surface, capturing pictures of the magnetic structure of the sample. The MFM frequently employs a non-contact mode because the magnetic force of interaction is a greater range than the atomic force. It is not affected by surface contamination and may be carried out under normal conditions. The MFM measures the vertical component of the force between the sample and the tip. The following equation explains the motion of the cantilever

FIGURE 2.7: The photograph of transmission electron microscope.

for a damped harmonic oscillator [28]:

$$m\frac{d^2z}{dt^2} + \Gamma\frac{dz}{dt} + k(z - z_0) = F_{ex}(t) + F_z(z) \tag{2.8}$$

where, m denotes the "mass of the cantilever", Γ is the damping coefficient, $F_{ex(t)}$ denotes the sinusoidal driving force, z_0 denotes the cantilever's equilibrium position in the absence of a force, and $F(z)$ denotes the vertical component of force between the cantilever and the sample. Because, we are concerned only with magnetic force in this situation, $F(z)$ must be integrated across the whole magnetic volume on the tip and cantilever:

$$F_z = \frac{\partial}{\partial z}\int_{tip} dV\ \mu_0\left(\mathbf{m}_{tip}.\mathbf{H}\right) \tag{2.9}$$

here, m denotes "magnetic moment" of the tip and H denotes "stray field" originating of the sample.

Assuming F_z is small, the Taylor expansion of Eq. 2.9 gives:

$$m\frac{d^2z}{dt^2} + \Gamma\frac{dz}{dt} + k\left(z - z_0\right) = F_{ex}\left(t\right) + F_z\left(z = z_0\right) + \frac{dF_z}{dz_{z=z_0}}\left(z - z_0\right) \tag{2.10}$$

We define k_{eff} = k-dF_z/dz, the equation 2.10 can be rewritten as:

$$m\frac{d^2z}{dt^2} + \Gamma\frac{dz}{dt} + k_{\text{eff}}\left(z - z_0\right) = F_{\text{ex}}\left(t\right) + F_z\left(z = z_0\right) \tag{2.11}$$

The cantilever resonant frequency in the presence of a force gradient is given by

$$f_0' = \frac{1}{2\pi}\sqrt{\frac{k_{eff}}{m}} \tag{2.12}$$

The Taylor expansion of the equation 2.11 in the limits of $dF_z/dz \ll k$, then,

$$\frac{dF_z}{dz} = \frac{2k}{f_0}\Delta f \tag{2.13}$$

In either static (slope detection) or alternating current (AC) mode, the force gradient may be sensed (frequency modulation). The amplitude or phase of the cantilever is measured in the static mode [29]. At room temperature, this mode is widely used in commercial MFM. Improving the quality factor (Q) of the cantilever will increase detection sensitivity at the expense of lowering measurement bandwidth. The AC mode with frequency modulation technique bypasses high Q cantilevers' bandwidth constraint. Positive feedback is utilized in AC mode to oscillate the cantilever at its resonant frequency and measure f, which is often done using a laser interferometer [30].

$$\frac{dF}{dz_{\min}} = \frac{1}{A}\sqrt{\frac{4kk_0TBW}{\omega_0 Q}} \tag{2.14}$$

where, BW is the measurement of bandwidth, $\omega = 2\pi f_0$ and A is the amplitude of oscillation of the cantilever.

The magnetic sensitivity of MFM depends not only on the minimum detectable force gradient, but also on the tip shape and the magnetic field source.

2.4 Physical properties

2.4.1 Static magnetic properties

The PPMS from "Quantum Design" was used to measure the M of the prepared samples. An electromagnet based VSM has been employed to check the magnetic response of thin-films.

2.4.1.1 Physical property measurement system (PPMS)

The PPMS in VSM mode works as per the induction law of Faraday, i.e., changing the magnetic flux creates an electric field and can estimate the change in the magnetic field. The sample is oscillated by the outside H-field with a certain frequency (n). This results in changes to the magnetic flux and emf (V) in the coils [31]. The term for the generated emf is as follows:

$$V = -N\frac{d\phi}{dt} = -NA\frac{dB}{dt} = -NA\mu_0\frac{d(H+M)}{dt} \tag{2.15}$$

here "A, N, μ_0, and M" are "indicative of the area", the "number of turns in the coil", "magnetic permeability" and M of the sample. This leads to AC voltage in the pick-up coils, and is proportional to M. The "lock-in amplifier" acquires the pick-up coils' response. The AC signal that the coil apprehends is proportional to the sample's M. The magnetic hysteresis ($M - H$) loop is recorded with the assistance of a computer. In Fig. 2.8 a photograph of the PPMS device was displayed. In the present study, temperature-dependent magnetisation ($M - T$) measurements were conducted by PPMS set-ups in H-field of 9 T, over a temperature, 10 – 325 K of vibrational sample magnetometry.

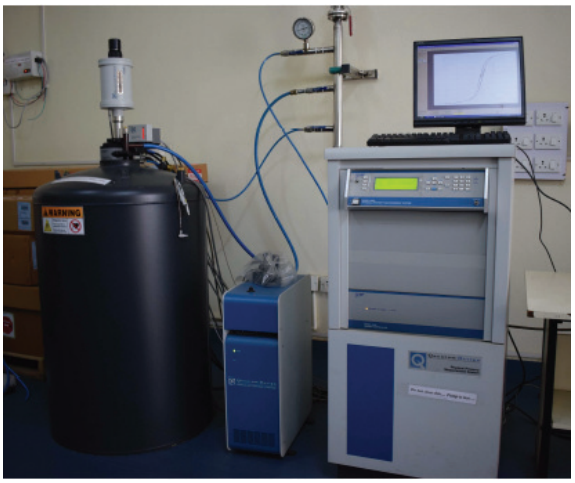

FIGURE 2.8: Photograph of physical property measurement system

2.4.2 Dynamic magnetic properties

2.4.2.1 Ferromagnetic resonance (FMR)

The resonant absorption of external microwave signal in FM materials is known as FMR. When a spin (e) works as a magnetic "dipole" in an external H-field of uniform intensity H, it precesses around the H-field's direction. The precession frequency (the "Larmor precession frequency") is proportional to H,

$$\omega_L = \gamma H \tag{2.16}$$

here, γ = gμ_B/h is the "gyromagnetic ratio" of e. The resonant absorption of energy can occur when this "magnetic dipole" is exposed to an external electromagnetic radiation applied perpendicular to H, and the resonance condition can be written as

$$\hbar\omega = g\mu_B H \tag{2.17}$$

This is the well-known "electron spin resonance" (ESR) phenomenon, which occurs in substances having unpaired e spins and non-interacting moments. The situation is much different in the case of FM substances than it is in the case of "non-interacting spins" as in PM materials. Griffiths [32] discovered the phenomena of FMR, which is the resonant microwave absorption in a system of highly interacting spins. This high exchange contact causes a parallel alignment of spins, which results in a significant resultant M or internal field. The resonance requirement is no longer true in the sense that in the instance at hand, the external field H must be substituted by an effective field H_{eff} that, in addition to H, takes into account the anisotropy fields inherent in FM materials [30].

An alternating magnetic field in the form of microwave power is provided at right angles to the static magnetic field via the coplanar waveguide (CPW). Resonance is found when the frequency of the microwave field coincides with the frequency of precession. A significant reduction in transmitted microwave power is observed at resonance. The atomic moments are dispersed in the 2J+1 energy level in the presence of the field. The potential energy of each atomic moment in magnetic field is (-μ_HH). The separation between the levels is given by

$$\Delta(E) = \Delta(\mu_{\mathrm{H}} H) = g\mu_B H \tag{2.18}$$

where, μH = g$\mathrm{M}_J\mu_B$, g is the spectroscopic splitting factor, M_J is the quantum number of J. The neighbouring value of M_J vary by one for every given value of J. At resonance, the energy difference between atomic levels (eq. 2.11) equals the energy of the microwave transmitted by the CPW, which is hν,

$$h\nu = g\mu_B H \tag{2.19}$$

The M precession around the effective H-field direction can be caused by both precessional torque and the damping term. Taking both factors into account, the effective torque may be given as "Landau-Lifshitz equation" [33]:

$$\frac{\partial \mathbf{M}}{\partial t} = -\gamma\,(\mathrm{M} \times \mathrm{H_{eff}}) - \lambda \frac{\mathbf{M}}{M^2} \times (\mathrm{M} \times \mathrm{H_{eff}}) \tag{2.20}$$

The first component in the preceding equation is the precessing torque, and the second term is the damping like torque with tunable damping parameter, which is described as λ and $\gamma = ge/2mc$, where c is the "velocity of light", m and e are the "mass" and "charge" of electron, respectively. An alternating damping like torque is proposed by Gilbert which is given below

$$\frac{-\alpha}{M}\left(\mathrm{M} \times \frac{\mathrm{dM}}{\mathrm{dt}}\right) \tag{2.21}$$

where

$$\alpha = \frac{\lambda}{\gamma M} \tag{2.22}$$

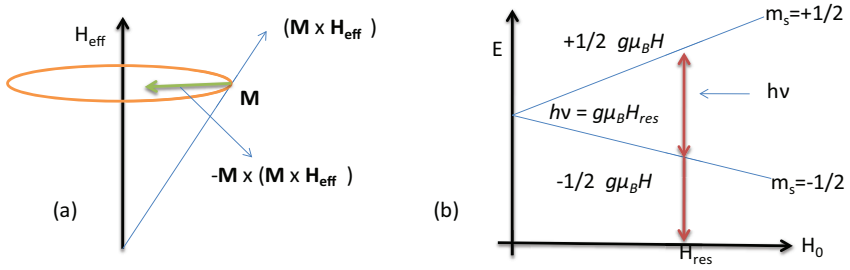

FIGURE 2.9: (a) Precession of the magnetic moment with a magnetization vector M towards the effective magnetic field direction due to the presence of damping like torque, (b) The splitting of the energy levels in the presence of magnetic field where the energy difference of the atomic levels at resonance $g\mu_B H_{res}$ is equal to the energy of the microwave power $h\nu$.

So, the "Landau-Lifshitz-Gilbert equation" is given as

$$\frac{\partial \mathbf{M}}{\partial t} = -\gamma\,(\mathrm{M} \times \mathrm{H_{eff}}) - \frac{\alpha}{M}\left(\mathbf{M} \times \frac{d\mathbf{M}}{\mathrm{dt}}\right) \tag{2.23}$$

Figure 2.10 shows the schematic of CPW geometry of FMR with the use of lock-in amplifier. In this FMR setup, we sweep the external applied H-field and hold the frequency of the perturbing field (h_{rf}) constant.

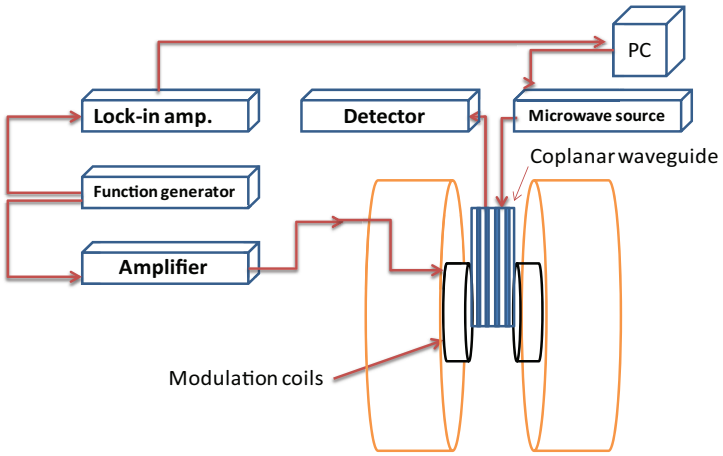

FIGURE 2.10: Schematic representation of co-planar wave guide based FMR.

The effective magnetic field is defined as [34],

$$H_{\mathrm{eff}} = H_{\mathrm{ext}} + H_{\mathrm{an}} + h_{rf} + H_{\mathrm{demag}} \tag{2.24}$$

where, H_{ext}, H_{an} and H_{demag} are the externally applied magnetic field, the anisotropy and the demagnetization fields, respectively.

We can write,

$$\frac{\partial \mathbf{M}}{\partial t} = -\gamma\,(\mathbf{M} \times \mathbf{H}_{\mathrm{in}}) \tag{2.25}$$

The demagnetizing field $H_d = -NM$, where, the demagnetization tensor is defined as [35].

The modified magnetic field can be written as; $H_{\text{in}} = H_0{}' - N_{\text{i}} M_{\text{i}}$

The oscillating component of magnetization in $x - y$ plane is defined as:

$$\frac{dM_x}{\text{dt}} = -\mu_0 \gamma \left[H_0^{'} + \left(N_y - N_z\right) M \right] M_y \tag{2.26}$$

$$\frac{dM_y}{\text{dt}} = -\mu_0 \gamma \left[H_0^{'} + \left(N_x - N_z\right) M \right] M_x \tag{2.27}$$

The solution of the equation is the Kittel equation and is mentioned as,

$$\omega_0^2 = \gamma^2 \mu_0^2 \left[H_0^{'} + \left(N_y - N_z\right) M \right] \left[H_0^{'} + \left(N_x - N_z\right) M \right] \tag{2.28}$$

A thin film with negligible in-plane anisotropy and $N_y = N_z = 0$ and $N_x = 1$,we have

$$\omega_0 = \gamma \mu_0 [H_0^{'} \left(H_0^{'} + M \right)]^{\frac{1}{2}} \tag{2.29}$$

here, the MCA also affects FMR precession frequency. In the presence of MCA, the above equation modifies to

$$\omega_0 = \gamma \mu_0 [(H_0^{'} + H_{\text{an}}) \left(H_0^{'} + H_{\text{an}} + M \right)]^{\frac{1}{2}} \tag{2.30}$$

where, $H_{an} = 2K_1/M_S$ is the anisotropy field.

FIGURE 2.11: Photograph of coplanar waveguide based FMR measurement system.

The M_S, spectroscopic splitting factor g, and magnetic anisotropy field H_{an} of thin films with in-plane M are calculated using the Kittel formula. The parameters such as the Gilbert damping constant and inhomogeneous linewidth broadening H_0 may be derived from the linewidth (ΔH) versus frequency (f). The lock-in amplifier performs phase-sensitive detection. It distinguishes the signal from the noise, which is several orders of magnitude larger than the signal. This technique modulates the FMR spectrum so that the output is the derivative of the absorption spectrum. After removing the rf component of the signal with a diode detector, the lock-in amplifier is utilized to determine the modulated response [36]. A photograph of the CPW technique used for FMR measurements is shown in Fig. 2.11.

2.5 Conclusion

In conclusion, the present chapter describes the working principles of instruments used for preparation, characterization and physical property measurement systems.

References

[1] F. Bodker and S. Morup, Europhys. Lett. **52** 217 (2000).

[2] C. Xu and A. Teja, J. Supercrit. Fluid. **44** 85 (2008).

[3] S. P. Gubin, Y. A. Koksharov, G. B. Khomutov and G. Y. Yurkov, Uspekhi Khimii **74** 539 (2005).

[4] L. F. Cotica, V. F. Freitas, D. M. Silva, K. Honjoya, I. A. Santos, V. CP. Fontanive, N. M. Khalil, R. M. Mainardes, E. S. Kioshima, R. Guo and A. S. Bhalla, J. Nano. Res. **28** 131 (2014).

[5] R. A. Bepari, P. Bharali and B. K. Das, J. Chem. Society **36** 136 (2014).

[6] S. Saha, A. Pathak and P. Pramanik, J. Mater. Sc. Lett. **14** 35 (1995).

[7] P. N. Oliveira, D. Alanis, R. D. Bini, D. M. Silva, G. S. Dias, I. A. Santos, L. F. Cotica, R. Guo and A. S. Bhalla, Int. Ferroelectr. **174** 88 (2016).

[8] J. A. Michael, Appl. Phys. A **93** 579 (2008).

[9] G. K. H. Douglas, and B. Chrisey, Pulsed laser deposition of thin films, John Wiley and Sons, Inc. (1994).

[10] T. Venkatesan and S. M. Green, Indian J. Phys. **2** 22 (1996).

[11] R. Eason, Pulsed laser deposition of thin films: Applications led growth of functional materials, John Wiley and Sons (2007).

[12] D. Dijkkamp, Appl. Phys. Lett. **51** 619 (1987).

[13] D. B. Chrisey and G. K. Hubler, Pulsed Laser Deposition of Thin Films, John Wiley and sons (1994).

[14] A. Namiki, T. Kawai and K. Ichige, Surf. Sci. **166** 129 (1986).

[15] S. Zhang, Springer (2014).

[16] C. Belouet, Appl. Surf. Sci. **96** 630 (1996).

[17] A. Swain, Charge order suppression and magnetization switching in manganites, Thesis, Chapter 2 (2019).

[18] C. C. Kock, Annu. Rev. Mater. Sci. **19** 121 (1989).

[19] L. Lu and M. O. Lai, Mechanical alloying (Kluwer Academic Publishers, Boston, 1998).

[20] Y. Jinahua, Microstructure and magnetic anisotropy of Cobalt ferrite thin films, Thesis Chapter 2, PP 34-35 (2009).

[21] B. D. Cullity, Elements of X-ray diffraction, Addison-Wesley Publishing Company, (1978).

[22] R. A. Young, The Rietveld Method, Oxford University Press, (1991).

[23] H. M. Rietveld, J. Appl. Crystallogr. **2** 65 (1969).

[24] J. R. Carvajal, Phys. B: Condens. Matter **192** 55 (1993).

[25] P. J. Goodhew, J. Humpphreys and R. Beanland, Electron microscopy and analysis, Taylor and Francis (2001).

[26] P. E. Champness, Electron diffraction in the transmission electron microscope, Gar-land Science (2001).

[27] L. Luan, Magnetic force microscopy studies of unconventional superconductors: Single vortex manipulation and magnetic penetration depth measurements, PhD Thesis, (2011).

[28] Y. Marin and C. C. Williams, Appl. Phys. Lett. **50** 1455 (1987).

[29] T. Albrecht, P. Grutter, D. Horne and D. Rugar, J. Appl. Phys. **69** 668 (1991).

[30] V. Siriguri, Investigation of the magnetic properties of amorphous alloys using ferromagnetic resonance and Mossbauer techniques, PhD thesis, (1998).

[31] B. D. Cullity and C. D. Graham, Introduction to magnetic materials, John Wiley and Sons, (2011).

[32] J. H. E. Griffiths, Nature **158** 670 (1946).

[33] T. L. Gilbert, IEEE Trans. Magn. **40** 3443(2004).

[34] G. Woltersdorf and B. Heinrich, Phys. Rev. B **69** 184417 (2004).

[35] S. Nayak, Static and dynamic magnetic properties of soft or hard ferromagnetic and ferromagnetic or antiferromagnetic bilayers, PhD thesis, (2020).

[36] C. Kittel, Phys. Rev. **73** 155 (1948).

Chapter 3

Structural, morphological, microstructural and magnetic properties of $CoFe_2O_4$ and $La_{0.7}Sr_{0.3}MnO_3$ bulk and nanoparticles

3.1 $CoFe_2O_4$

3.1.1 Introduction

When the particle size of magnetic materials is reduced from bulk to nanometer length scale, their physical properties show significant variation. The geometric constraints, reduced coordination number of the atoms present on the surface of magnetic nanoparticles are responsible for the change in physical properties such as effective magnetic anisotropy, coercivity, remanence and susceptibility compared to their bulk counterparts [1, 2]. On the other hand, the rare-earth-based permanent magnets are now essential components in everyday life applications such as electronic devices, hard discs, automobiles, wind turbines, and hybrid-electric vehicles [3, 4]. The widespread use of these rare-earth elements from restricted resources prompted the scientific community to consider alternatives. Therefore, hard-ferrites in bulk quantity with single-domain particles appear to be the best potential materials for permanent magnet applications. Because of its significant MCA, increased H_C, and mild M_S, the CFO was recognised as a good material for the indicated purpose among the spinel ferrites [5–9]. The hard-ferrites appear to have the potential to replace rare-earth magnets in a variety of applications, where lower performance is required [7–9]. The present study aims to synthesize a wide range of CFO particles (from 7 to 780 nm) with different shapes using a wet-chemical-based thermal-decomposition technique. The physical properties of CFO particles were carefully examined by classifying them into single domain and multidomain particles. The maximum energy product of single-domain nanoparticles was evaluated in order

to check for potential permanent magnet-based applications. Using the "law of approach to saturation" magnetization data was analysed as a function of particle size. The current study found a strong correlation between the size, shape, and magnetic properties of CFO particles. The current study presents the effect of particle size and shape on magnetic properties of CFO nanoparticles and their use permanent magnets in device applications at RT. Here, sintering at temperatures ranging from 300 °C to 1200 °C was done to produce a set of CFO samples with varying particle sizes and shapes.

3.1.2 Experimental

The thermal decomposition via polymeric method has been used for the synthesis of CFO samples. A 10% (w/w) solution of poly vinyl alcohol (PVA) was made by heating at 70 ^{o}C for 24 h [12]. The precursors, PVA, $Co(NO_3)_2.6H_2O$ and $Fe(NO_3)_3.9H_2O$ were mixed in the ratio 10:0.33:0.67. The aqueous solution of $Co(NO_3)_2.6H_2O$ was added to the solution of PVA at first followed by $Fe(NO_3)_3.9H_2O$. The solution thickens after being stirred for 45 min at a temperature of 70 °C. The water content from the slurry was removed by baking the sample after seperating in petri dishes at a temperature of 110 °C for 5 h. After that the sample was ground and calcined for 2 h at 250 °C. The obtained powder was sintered at a temperature ranging from 300 °C to 1200 °C at a ramp rate of 5 °C/min. The samples sintered at 300 °C, 450 °C, 600 °C, 750 °C, 900 °C and 1200 °C, were named as CFO-300, CFO-450, CFO-600, CFO-750, CFO-900 and CFO-1200, respectively.

The prepared samples were characterized structurally by XRD by using "Philips x-ray diffractometer" with Cu-Kα radiation source. The crystallite sizes of these samples were estimated by using the modified Scherrer's formula. The surface morphology and composition of the samples were analyzed by the FESEM ("Carl-ZEISS, ULTRATM-55") attached with EDX spectrometer. The microstructure, particle size and shape were analyzed by using ("FEI Tecnai 200 kV D2083") TEM. The *M-H* loops of the samples at different temperatures were measured by using PPMS in VSM mode.

3.1.3 Results and discussion

3.1.3.1 X-ray diffraction

The XRD patterns for the samples sintered at different temperatures are shown in Fig. 3.1. The CFO samples were found to crystallize in a single-phase with $Fd\bar{3}m$ space group of cubic structure without any impurity. The XRD data of these samples were also compared with standard data with (JCPDS no. 00-022-1086). As it can be observed from Fig. 3.1 that (111), (220), (311), (222), (400), (422), (511) and (440) are the dominant reflections proving that the samples are stabilizing in inverse spinel structure.

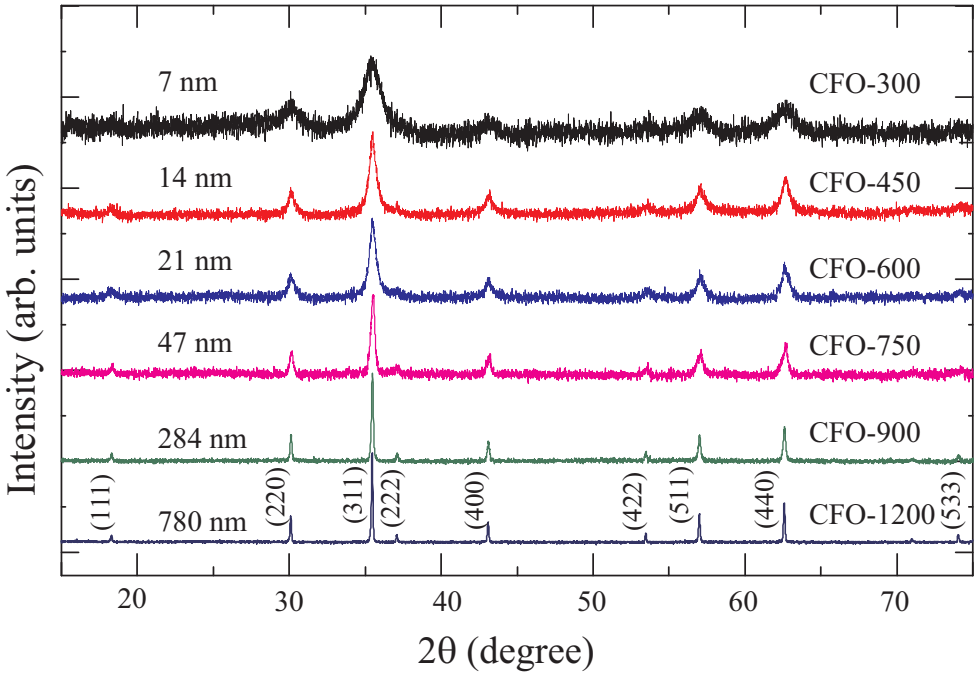

FIGURE 3.1: The room-temperature XRD patterns of CFO samples sintered at different temperatures.

As the sintering temperature increased, the intensity of the peaks enhanced but the FWHM decreased. The increase in intensity results from the increased crystallinity, whereas the reduction of FWHM is the result of increased particle size of the samples. The absence of any peak shift in XRD patterns as a function of sintering ensures the non-uniform strain in the crystallites. The peak broadening in the present case mainly arises due to (i) non-uniform strain associated with crystallites, (ii) reduced crystallite sizes and (iii) instrumental broadening. In the present case, the instrumental broadening was corrected by considering FWHM of standard SiO_2 material. The crystallite size of the samples was estimated by using the Williamson-Hall (W-H) equation [13],

$$\beta = \frac{k\lambda}{Dcos\theta} + \epsilon tan\theta \tag{3.1}$$

where, $\beta = \beta_e$-β_i; β_e represents the FWHM of diffraction peak and β_i represents the instrumental broadening, D is the average crystallite size, k is grain shape factor, λ is wavelength of Cu-Kα (1.5406 Å) radiation source and ϵ represents the microstrain present in the samples. The average crystallite size and microstrain of the samples were calculated from the y-intercept and slope of linear fit of $\beta cos\theta$ versus $sin\theta$ plots, respectively. Figure 3.2 shows the W-H plots of the CFO samples.

The XRD data of all the samples were analyzed by adapting the Rietveld refinement method using "FullProf" software based on $Fd\bar{3}m$ space group. The measured and simulated XRD patterns along with their difference are shown in Fig. 3.3. While refining the data, the lattice parameter, scale factor, shape parameter (u, v, w) and

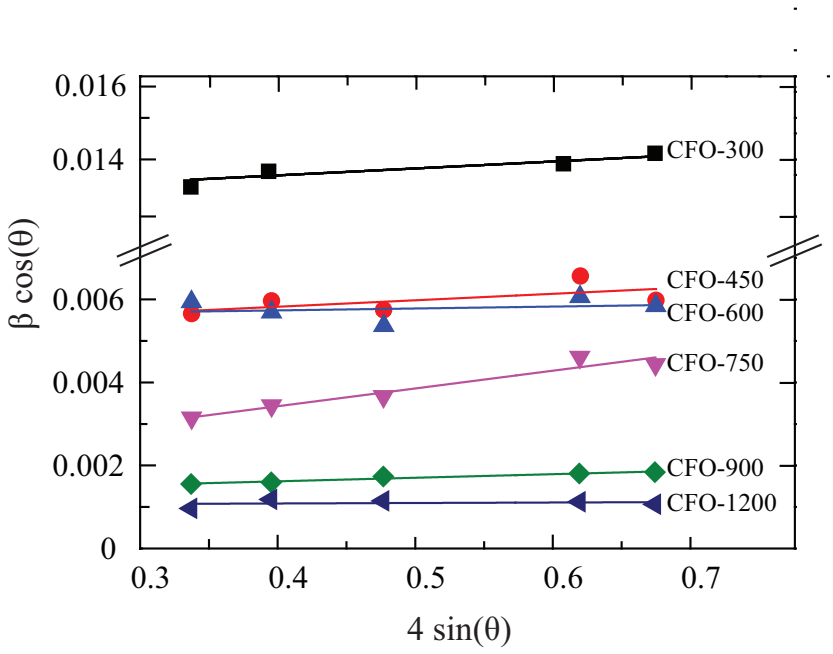

FIGURE 3.2: Williamson-Hall plot for the CFO samples.

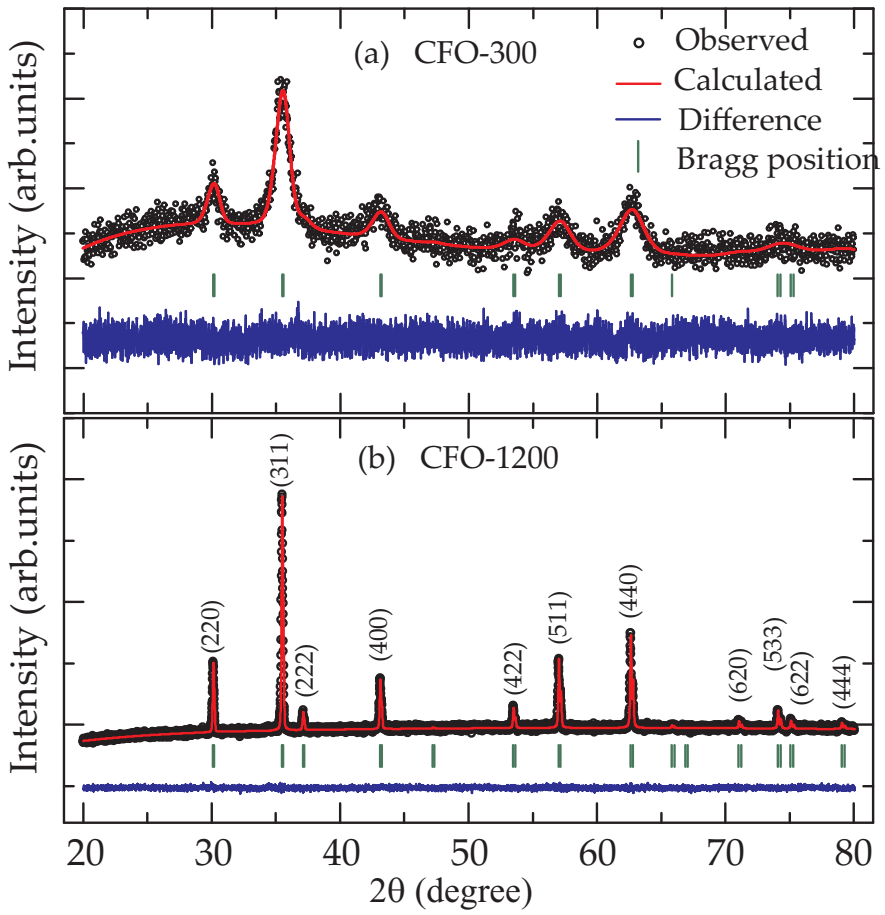

FIGURE 3.3: Rietveld refined XRD (solid red) patterns along with experimentally measured (black circles) ones for (a) CFO-300 (7 nm) and (b) CFO-1200 (780 nm) samples. The blue curve represents the difference in measured and simulated patterns. The marked vertical (green) bars represents the Bragg positions.

oxygen position ($x = y = z$) were taken as free parameters and carefully refined until an acceptable χ^2 value was obtained. The obtained crystallographic parameters are given in Table 3.1. As is evidenced from the table that, no systematic change in lattice parameters was observed with an increase in sintering temperature, which explains the absence of uniform strain in the samples. Here, it appears that the increase in sintering temperature may improve the coalescing nature of smaller crystallites to form a bigger one. To know more about the grain growth, particle size and microstructure of the samples as a function of sintering temperature, FESEM and TEM measurements were done and results are presented.

TABLE 3.1: Crystallographic and particle size data of CFO samples.

Parameters	**CFO-300**	**CFO-450**	**CFO-600**	**CFO-750**	**CFO-900**	**CFO1200**
$a = b = c$ (Å)	8.387	8.377	8.369	8.388	8.387	8.385
Volume	589	588	586	590	589	589
Density	5.28	5.30	5.31	5.28	5.28	5.28
Co ($x = y = z$)	0.375	0.375	0.375	0.375	0.375	0.375
Fe ($x = y = z$)	0	0	0	0	0	0
O ($x = y = z$)	0.25173	0.24387	0.24730	0.24294	0.24212	0.24365
R_p	67.0	50.9	51.1	81.3	46.2	26.6
R_{wp}	40.9	27.0	26.0	30.7	17.0	10.8
R_e	38.4	24.5	24.5	28.3	16	9.74
χ^2	1.134	1.212	1.130	1.180	1.130	1.223

3.1.2.2 FESEM

The FESEM analysis of these samples clearly revealing the change in morphology of the grains have been observed with increased annealing temperature. The increase in grain size has been observed as the sintering temperature is increased. The obtained results are in agreement with the XRD graphs. The surface morphology showed significant changes as the sintering temperature changed from 300 °C to 1200 °C. The corresponding microscopic images in Fig. 3.4 show that these grain shapes change as spheres (CFO-300), pyramids (CFO-450), lamellae (CFO-750), octahedra (CFO-900) and truncated octahedra (CFO-1200). Although almost all of the samples had a mixture of small and large grains, the grain shapes were found to be uniform over a large area of the samples' surface. These various shape grains are expected to have a significant impact on the physical properties of the current samples.

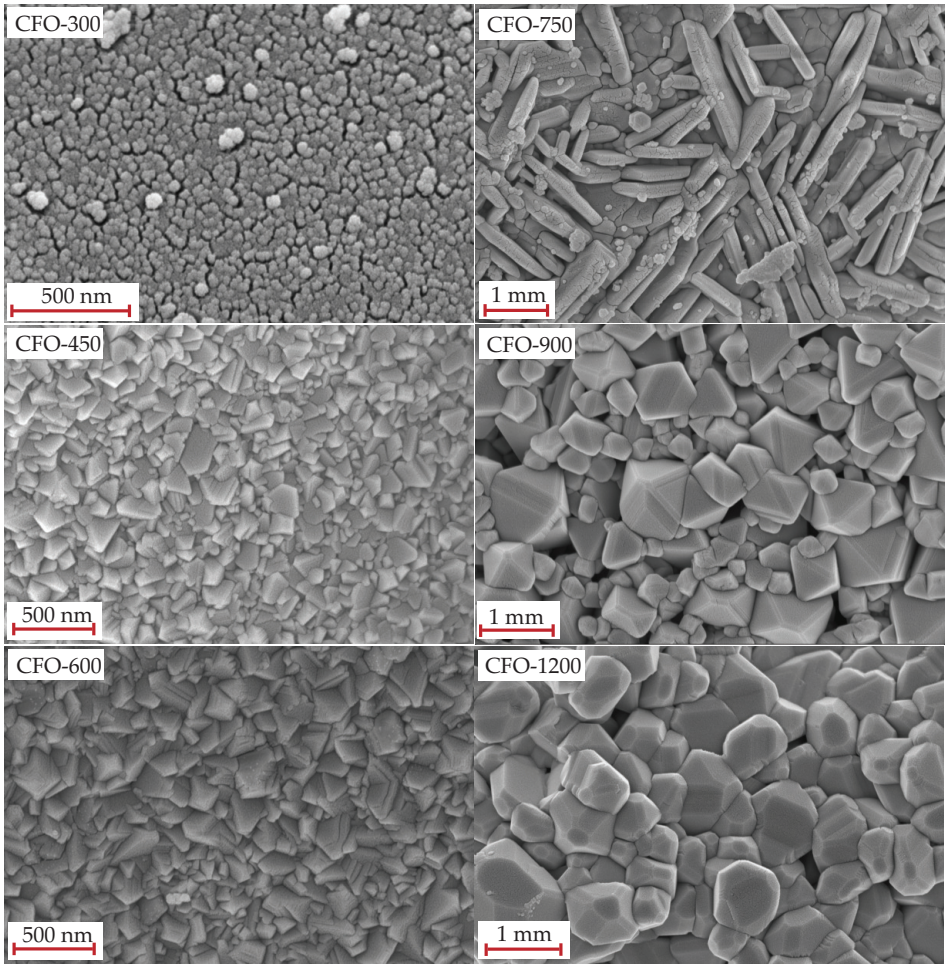

FIGURE 3.4: The FESEM micrographs of CFO samples.

3.1.3.3. HRTEM

With a view to know more about the growth aspects of these grain shapes and the morphological transformation of particles, the TEM measurements were carried out. As can be seen in Fig. 3.5, the transformation of the mentioned shapes was confirmed by analysing two-dimensional (2D) TEM pictures obtained from the respective samples. When sintered at 300 °C, the nanoparticles were found to be circular, but when sintered at 450 °C, 600 °C, and 750 ^{o}C, they became square/rhombohedra. These are, in fact, two-dimensional projections of one of the facets of corresponding three-dimensional shapes seen in FESEM micrographs. The particle sizes of sintered samples sintered at 900 °C and 1200 °C were found to be in the submicron to micron range. Due to bigger particles a clear TEM images were not possible as the non-transmission of electrons from these samples. In addition, as shown in the corresponding TEM image (see Fig. 3.5), electron diffraction patterns were used to understand the crystalline nature of these nanoparticles. The polycrystalline nature of the samples is clearly visible in the diffraction patterns and crystallinity was found to improve as the sintering temperature is raised.

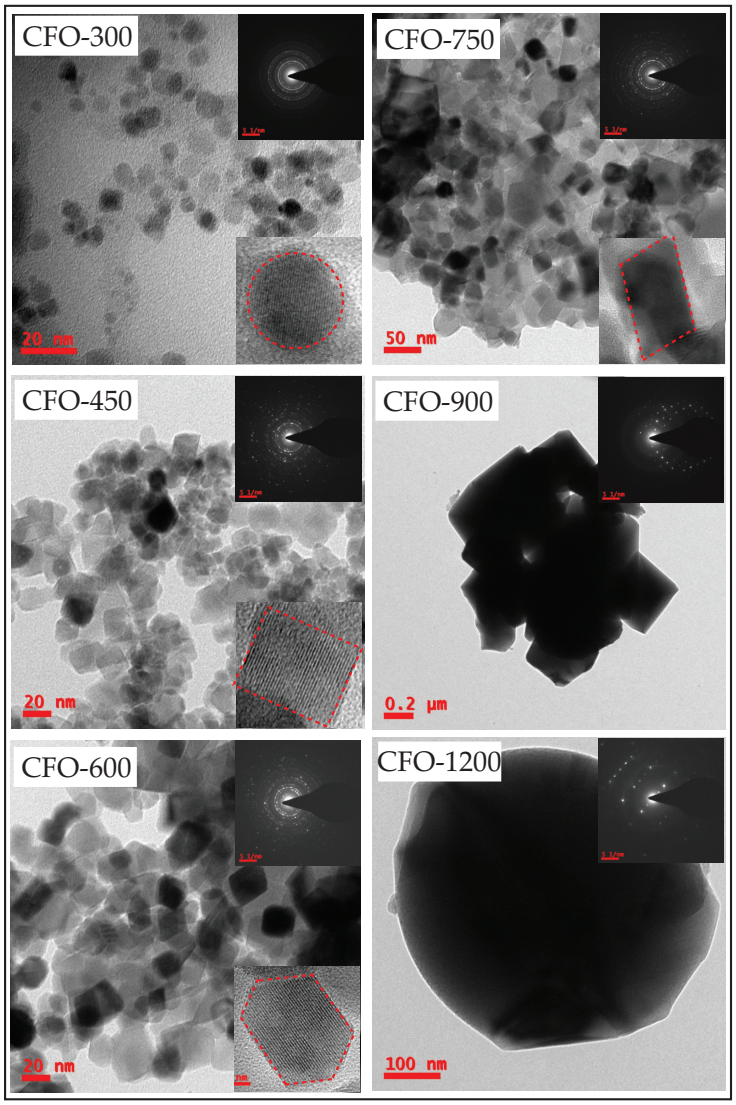

FIGURE 3.5: The tem micrograph images of CFO samples. The SAED patterns and high resolution images are shown in corresponding insets.

3.1.3.4 Growth mechanism

Based on morphological (FESEM) and microstructural (HRTEM) studies it has been understood that these shapes and sizes are following certain competing correlation between crystal growth and magnetic anisotropy. According to Moriyama et al, the CFO ferrite generates a "cubic crystal habit", anticipating preferential growth along the <100> direction [7, 15]. However, the current study (TEM micrographs) clearly shows that the formation of various shape particles appears to have a variety of other possible reasons. The particle shape of the CFO-300 sample became "spherical" to accommodate the minimum surface area due to dominant surface tension. Along with "pyramidal-shaped" particles (due to preferred growth direction), some "spherical-shaped" particles (due to surface tension) were found in the CFO-450 sample. This observation appears to imply that they have an effect on the magnetic properties

of the sample (discussed later). This finding suggests that an increase in particle size along the <100> direction compared to the <110> and <111> directions allows for a strong competition between surface tension and preferred growth direction, resulting in a mixture of "spherical" and "pyramidal" shape particles. In the case of the CFO-600 sample, however, the preferred growth direction completely dominates over the surface tension of the particles, resulting in "pyramidal" shape particles as seen in FESEM (Fig. 3.4) and the corresponding 2D projections as seen in HRTEM images (Fig. 3.5). The CFO-750 was noticed to have a "rectangular" plate-like structure, which was surprising. This drastic change in shapes could be attributed to the preferred direction along <100>. Besides this, when the sintering temperature was raised to 900 °C and 1200 °C, "octahedral" and "truncated octahedral" shapes were observed. These macroscopic shapes should theoretically be able to generate cubic habit from the cubic spinel structure with {100} facets; however, faster growth rate of CFO particles along <100> direction compared to <111> direction resulted in loss of {100} facets. A loss of this magnitude would result in {111} faceted octahedra, with {111} being the lowest energy facets. The sequence of surface energies associated with different crystallographic planes, as suggested by Wang [16], is (111) (100) (110). The major surface planes of a single-crystalline particle could be arranged in the following order: {111} > {100} > {110}. Also, based on the ratio (R) of growth rate in <100> to that in <111>, different shapes are expected for the particles. As a result, particles with a high growth rate in the <100> direction compared to the <111> direction with a large R (1.73) produce "octahedra" with {111} facets. Similarly, a "truncated octahedra" with {111} and {100} facets would result from particles with moderate growth along <100> compared to <111> with R (1.73). Increased temperature is thought to have caused different growth rates in different directions, resulting in a more"spherical" like "truncated octahedral" with eight {111} and six {100} facets, as shown in schematic representation of Fig. 3.6 [16,17]. However, additional experimental evidence is needed to confirm the current findings.

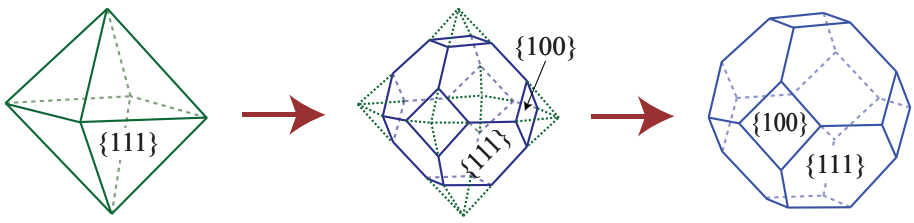

FIGURE 3.6: A schematic illustration of the transformation from octahedral shape to truncated octahedral shape of CFO nanoparticles.

According to Wang et al, self-assembled nanostructures, have the potential to maximise particle packing density by sharing common faces [16]. Except for the CFO-300 sample, due to preferential growth, any two particles would be in contact only when the planes of the same family were congruent to minimise the lattice mismatch. Otherwise, the crystals would rotate with each other to minimise the interface strain energy, which is defined as $\epsilon = | d_1 - d_2 | / d_1$, where d_1 and d_2 are

the inter-planar distances between two sets of planes. If there was an agreement between the similar surface planes, $d_1 = d_2$, then would be minimum and would form a coherent interface. As a result, in this case, the "coherent interface effect" was found to be quite prominent in all samples except the CFO-300 sample. This anomaly could be attributed to "high surface energy" and "finite-size effects".

3.1.3.5 Magnetic properties

(a) M-T measurements

Figure 3.7 shows the temperature dependent magnetization ($M - T$) measurements for all CFO samples. The T_C was obtained by applying a H-field of 100 Oe. The data ws collected by heating the samples from RT through the T_C at a rate of 5 °C/min. The T_C values were obtained from the minima of dM/dT versus T curves as shown in insets of Fig. 3.7. As expected, the M, decreases with increasing temperature and approaches to zero. From the graph it can be observed that the T_C is above RT. From this it can be confirmed that all CFO samples are showing FM behaviour at RT. This indicates that CFO nanoparticles are ideal for a wide range of technical applications above RT, such as in medical applications in which magnetocaloric characteristics can achieve local hyperthermia, to treat cancer spots.

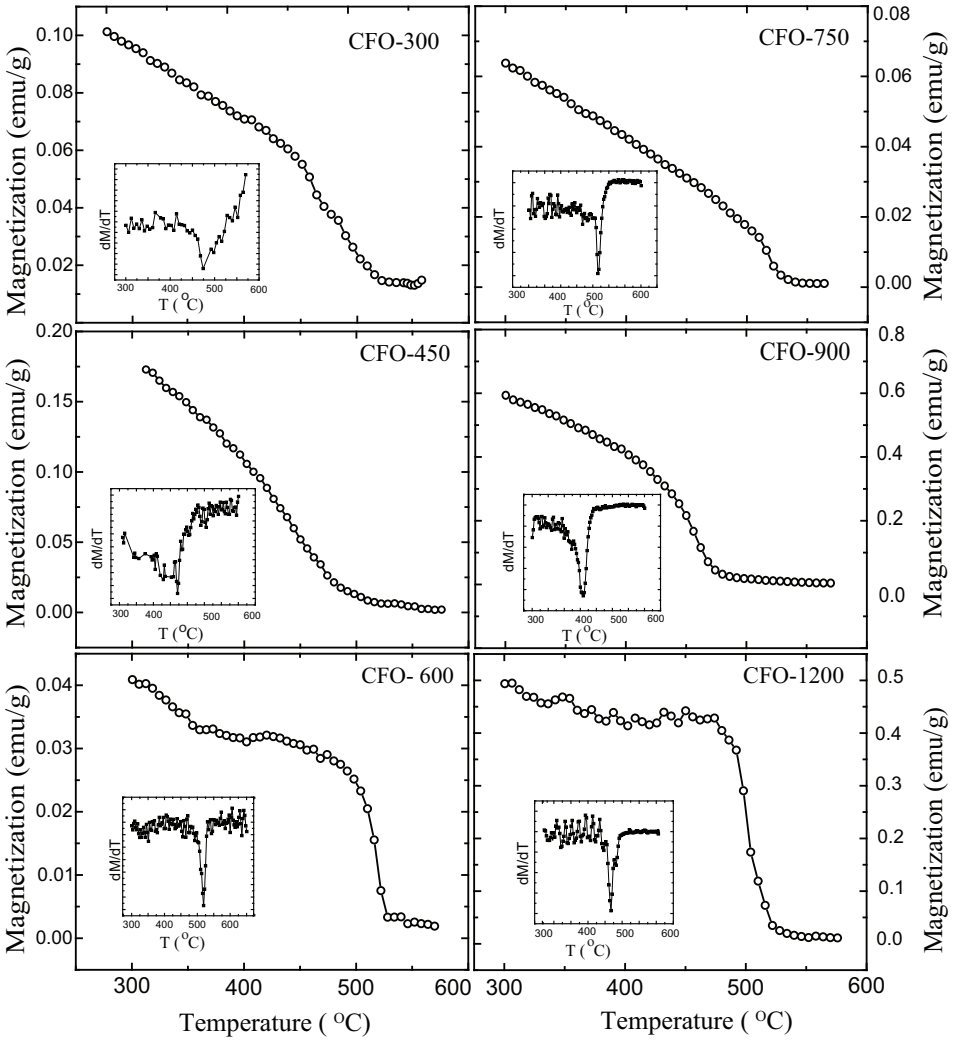

FIGURE 3.7: Temperature-dependent magnetization (M-T) curves of CFO samples. dM/dT versus T plots are shown in insets.

(b) M-H measurements

The *M-H* loops of CFO samples (presented in Fig. 3.8 (a) and (b)) measured at 300 K were found to saturate even in a 30 kOe applied H-field, whereas the *M-H* loops obtained at 5 K did not. That is, at low temperatures, the applied H-field is insufficient to orient spins in the direction of the applied H-field. Because there is less thermal energy in such an environment, the ratio of anisotropy energy to thermal energy increases, resulting in spin alignment in a preferred "easy" direction [6, 18]. Because of changes in spin arrangement, different magnetic properties are expected to be present in different shape and size particles. As the CFO is a ferrimagnet at RT with varying particle sizes and shapes, a strong correlation between microstructure and magnetic parameters is assumed. As a result, as shown in Fig. 3.9, the key magnetic parameters - H_C, M_S at 3 T, M_r, and "squareness ratio" ($S = M_r/M_{S3T}$) were extracted from *M-H* loops of CFO samples recorded at low (5 K) and room (300 K) temperatures. Figure 3.9 depicts the parameters plotted as a function of particle

size. Interestingly, with low H_C (13 Oe) and M_r = 0.109 emu/g, the CFO-300 sample was found to exhibit almost SP behaviour (H_C = 0 and M_r = 0) at RT, while the rest of the samples exhibited clear ferrimagnetic behaviour.

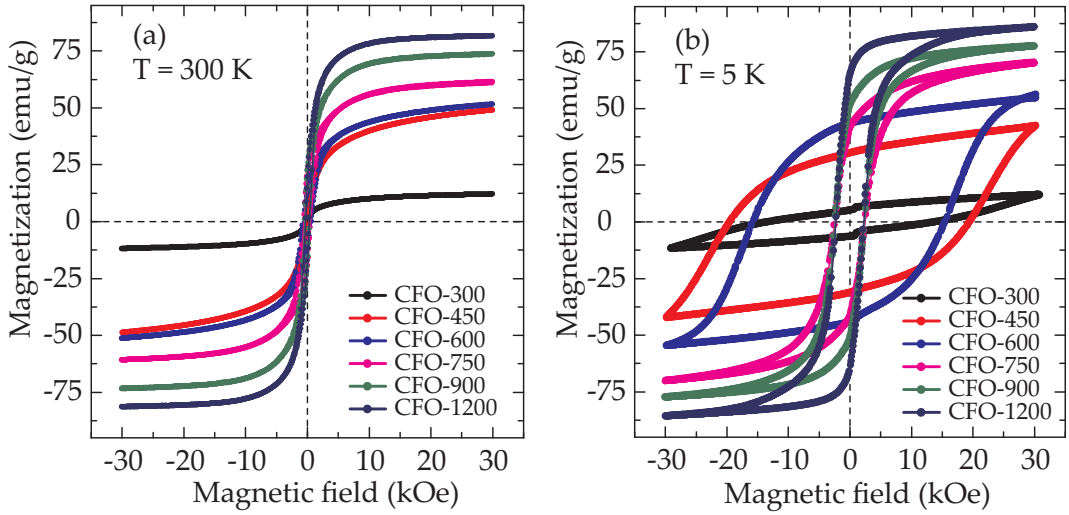

FIGURE 3.8: The M-H loops of set of CFO samples measured at (a) 300 K and (b) 5 K.

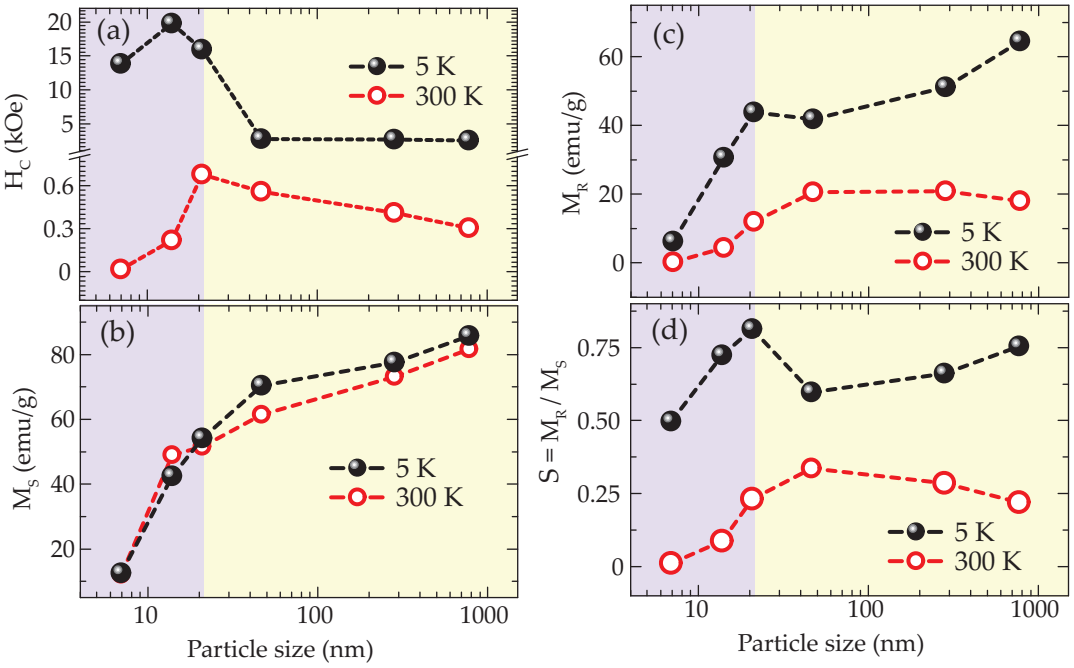

FIGURE 3.9: The plots of particle size dependence of (a) H_C, (b) M_S, (c) M_r and (d) squareness ratio for CFO samples measured at 5 K and 300 K, respectively.

The variation of H_C with particle size (for "spherical" and "pyramidal" shapes)

was found to increase initially up to 40 nm and then decrease. As previously reported [20, 21] the increase in H_C with particle size was observed to be a clear signature of "single-domain" particles. The decreasing trend of H_C with particle size greater than 40 nm suggests that a single domain particle is being transformed into a "multidomain" particle. Even after increasing the sintering temperature further, the "multidomain" nature of the particles with "lamellar", "octahedral", and "truncated-octahedral" shapes remains. The mechanism of M reversal in these particles can be in the following manner. Due to the SP nature of CFO-300 samples, the values of H_C of "spherical" shape particles were extremely small, whereas the coercive field was high for "pyramidal" shaped particles due to shape induced magnetic anisotropy. The coherent rotation of spins present in the sample is responsible for M reversal in single domain nanoparticles. In the case of large sized (multidomain) particles, the H_C values decreased as particle size increased. In the present study, not only did the particle's magnetic anisotropy play a role, but its shape also played a significant role in H_C. The mechanism underlying magnetization reversal in "multidomain" particles differed from that in "single-domain" particles. This has been shown schematically in Fig. 3.10.

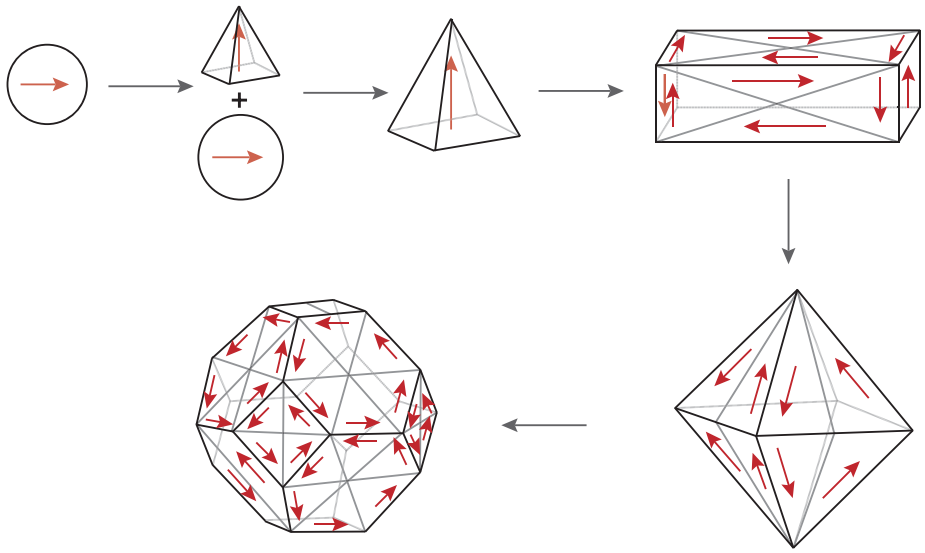

FIGURE 3.10: The schematic representations of possible magnetization orientations (solid red arrows) in different shape particles, proposed for CFO.

The curling rotation of magnetic spins, along with domain wall motion, is favoured by micromagnetic theory when the average diameter (size) of the spherical particle D exceeds a certain limit, D_0 (coherent diameter) [22]. $D_0 = 7.211\ l_{ex}$ for small spherical nanoparticles, where l_{ex} is the exchange length [23]. Based on the magnetic properties of bulk CFO, the exchange length,

$$l_{ex} = \sqrt{\frac{2A}{\mu_0 M^2}} = 5.26nm \tag{3.2}$$

was calculated by taking M_S = 81.36 (emu/g) $\approx$ 4.30$\times 10^5$ J/m, anisotropy constant K_{eff} = 0.74x10^5 J/m^3, and exchange stiffness constant A = 3.22x10^{-12} J/m into account [18, 24, 25]. The D_0 was estimated based on the obtained l_{ex} value and was found to be D_0 = 38 nm. As a result of these calculations, particles larger than 38 nm should exhibit crossover behaviour during M reversal from coherent to non-coherent rotation (curling rotation and domain wall motion). Surprisingly, the calculated D_0 value corresponded to the experimentally observed one (40 nm). The estimated critical particle size (volume, V_c) in this study was calculated as $V_c = \frac{25k_B}{K_{eff}} =$ 1.40x10^{-24}m^3. The average particle size in SP at RT was calculated using the V_c value [$D_c = (6V_c)^{1/3}$] and found to be 13.8 nm. In this case, the CFO-300 particle size (7 nm) was significantly smaller than the calculated critical size (13.8 nm). As a result, these calculations confirm the SP behaviour of the CFO-300 sample. Alongside from the previously mentioned reasons for the variation of H_C with particle size, size and shape-induced demagnetization effects cannot be ruled out, as evidenced by morphology and microstructure measurements. Fig. 3.9 (b) depicts a clear change in M_S obtained at 30 kOe from M-H loops measured at 5 K and 300 K. With increasing particle size, the value of M_S rises. The maximum values observed (M_S = 80-85 emu/g) for bulk sample (CFO-1200) measured at 300 K and 5 K agree with bulk CFO ferrites reported values [7, 10]. A "core–shell model" can explain the monotonous increase of M_S with particle size in the case of "single-domain" particles. The oriented magnetic domain is regarded as the core, while the surrounded magnetic dead surface layer, formed as a result of imperfect coordination of surface atoms, is regarded as the shell.

The ratio of "dead surface" ("shell") thickness to "domain volume" ("core") decreases as particle size increases, resulting in higher M_S values. The M_S values are expected to saturate as a function of particle size in the case of multidomain particles. The minimal increase in M_S values as a function of particle size, on the other hand, could be due to an insufficient applied H-field of 30 kOe to achieve magnetic saturation. Fig. 3.9 (c) and (d) show the relationship between M_r and "squareness ratio" (S = M_r/M_S) with particle size. At RT, the CFO-300 sample exhibits SP behaviour with nearly zero remanent and zero squareness ratio for 7 nm sized particles. According to the Stoner-Wohlfarth model, the observed values of S (0.23) for "single domain" particles in this case are well within the range of squareness values of non-interacting 3D random particles with uniaxial anisotropy [26]. The variation of M_r and squareness with particle size was identical to the variation of H_C with particle size, indicating a "single domain" particle crossover to "multidomain" particle behaviour [10]. The values of M_r and squareness measured at 5 K were found to be greater than the values estimated at 300 K, which could be due to the increased ratio of magnetic anisotropy to thermal energy at low temperatures [18].

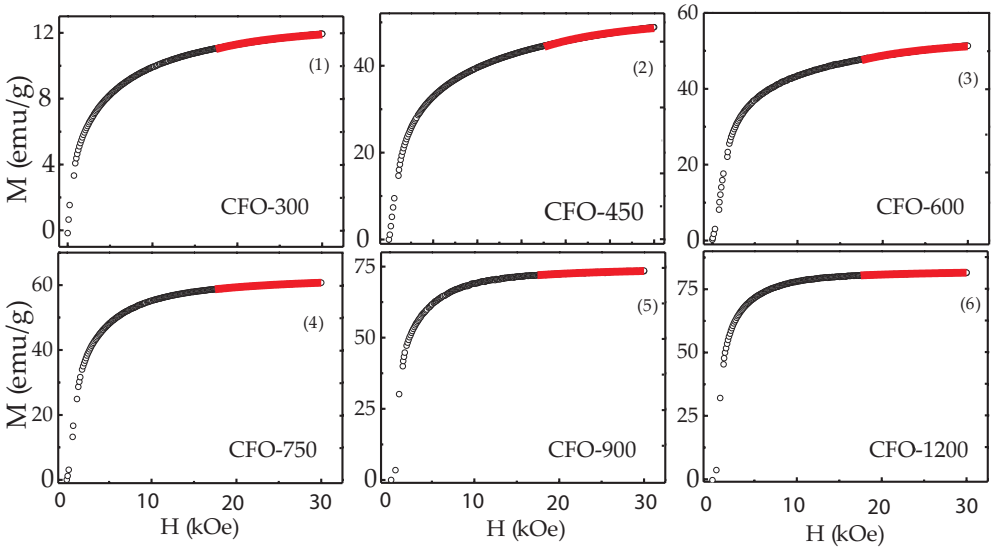

FIGURE 3.11: The law of approach to saturation fit to the *M-H* plots for CFO samples sintered at different temperatures.

The effective magnetic anisotropy constant (K_{eff}) is an important parameter for understanding the magnetic nature of particles and the underlying mechanism that causes M switching in applied H-fields. The value of K_{eff} was calculated by applying the law of approach to saturation given by [21] to a initial magnetization curve. The fittings have been shown in Fig. 3.11. The corresponding equation is shown below:

$$M = M_S(1 - \frac{b}{H^2}) + \chi H \tag{3.3}$$

where, M_S represents the saturation magnetization, $\frac{b}{H^2}$ represents the cubic anisotropy contribution of the CFO nanoparticles. The term χH is known as the induced M caused by a linear increase in M, especially at high fields and H is applied H-field. The parameter in the first term in the equation (3.3), b is given by the following equation,

$$b = 0.0762(\frac{K_{eff}^2}{\mu_0^2 M_S^2}) \tag{3.4}$$

where, K_{eff} is the "effective magnetic anisotropy constant" and μ_0 is the permeability of free space. The cubic anisotropy of random polycrystalline samples has a numerical coefficient of 0.0762 [21]. The equation (3.3) was used to fit the room-temperature experimental data of virgin curves, and the values of K_{eff} were calculated using the best-fit parameters.

Fig. 3.12 depicts the variation of K_{eff} with particle size (a). The K_{eff}'s variation with particle size was identical to the variation of H_C with particle size. The reason for this behaviour, as mentioned in the previous paragraph, is the cross-over of single domain to multidomain magnetic behaviour of the samples. However, the contributions of intrinsic and extrinsic effects such as shape, surface, stress, and so

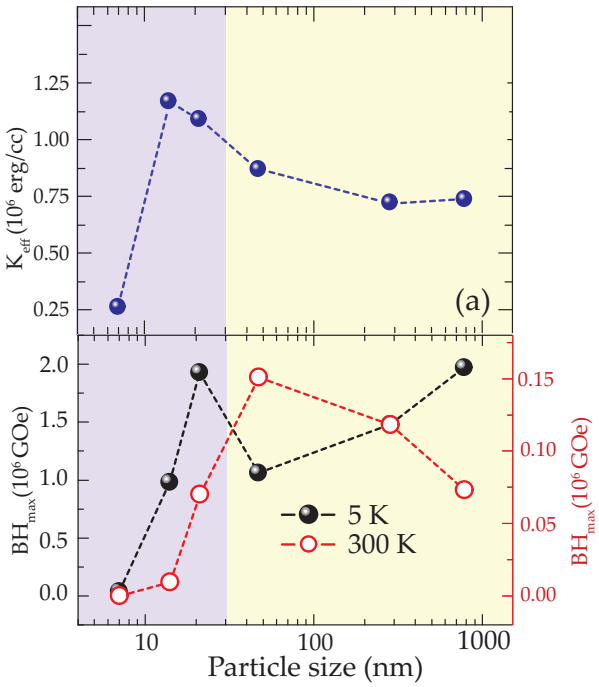

FIGURE 3.12: (a) Variation of effective magnetic anisotropy constant as a function of particle size for CFO samples at 300 K. (b) The values of BH_{max} as a function of particle size estimated at 5 K (black solid symbols) and 300 K (red hollow symbols).

on to the effective magnetic anisotropy are significant and must not be overlooked, especially when the particles change from magnetically "single domain" to "multidomain" as the sintering temperature rises. In any case, these issues are beyond the scope of the present work. "Maximum energy product" (BH_{max}) was estimated at 5 K and 300 K, where B and H are magnetic induction and applied magnetic field, respectively, in order to investigate the suitability of different shapes and sizes of CFO ferrite nanoparticles for permanent magnet applications. The BH_{max} is regarded as a permanent magnet's figure of merit [2]. At 5 K and 300 K, Fig. 3.12(b) depicts the variation of BH_{max} curves as a function of particle size. The observed behaviour is attributed to the strong "effective magnetic anisotropy" of the samples, as the values of BH_{max} at 5 K were found to be an order higher than the values obtained at 300 K. For 5 K and 300 K, the BH_{max} shows that K_{eff} and H_C have similar particle size dependences as a function of particle size, confirming the strong correlation between magnetic, particle size and shape. When the particle size is below the critical particle size of a "single domain", the state of the magnetic domain is related to particle size, as discussed in the previous sections. As a result, in the "single domain" case, BH_{max} increases as particle size increases, whereas in the "multidomain" case, domain wall motion is responsible for the rest of the variation in BH_{max} with particle size. It is clear that the critical size for CFO particles is 40 nm in this case. As a result, it is expected that a magnet made by compacting nanoparticles with critical particle sizes (40 nm) and oriented easy axes in a specific direction could be a promising material

candidate for developing "rare-earth-based permanent magnet" alternatives. In this case, these materials could be investigated for "permanent magnetic" applications in household appliances, computers, medical devices, and automobiles, where high magnetic performance in device applications at RT is not required [27].

3.2 $La_{0.7}Sr_{0.3}MnO_3$

3.2.1 Introduction

The half-metallic perovskite based manganites are arguably the most fascinating magnetic materials because of their enormous magneto resistance. Manganite with formula, $Ln_xAe_{1-x}MnO_3$; where, Ln = Lanthanide and Ae = alkaline earth metal. The Lanthanum and Strontium atoms occupy the 'A' sites in the ABO_3 perovskite, whereas the Manganese atoms occupy the 'B' sites. The electrons in the manganese atoms' $3d$ shell play a significant role in their electrical and magnetic behaviour. The interaction of the various manganese atoms determines the overall magnetic and electrical behaviour. The LSMO acts like a half-metal, suggesting that it might be used in spintronic applications [28]. Since it exhibits a FM with T_C at around 360 K with a significant magnetic moment at ambient temperature. Here, the LSMO is hole-doped manganite and is recognised to be an important material for device applications [29]. The ground states of a "spin-canted insulator", FM insulator, FM metal (FMM), AFM insulator and AFM metal are observed at low temperature ($T < T_C$), whereas paramagnetic insulator and metallic behaviour are observed at high temperatures ($T > T_C$) for various Sr doping concentrations [29]. In the process of preparation of LSMO target for PLD, the LSMO has been synthesized by using sol-gel method and sintered at different temperatures. Here we present result for two different particle size materials and studied the structural, morphological and magnetic properties.

3.2.2 Experimental methods

The LSMO was synthesized by considering nitric acid with the initial precursor materials of metal oxides/carbonates, metal nitrates in stoichiometric quantities. To make a clean transparent solution, the converted nitrates were put in double distilled water and carefully stirred. The metal nitrate solution was then mixed with "citric acid" in a 1:1 "molar ratio". The "pH" value is adjusted at around 7 by the addition of ammonia in order to speed up the reaction rate. This combination is next stirred by keeping on a hot plate in the range of 70-80 °C continuously. After the gradual evaporation of the water content in the combination, it resulted in a concentrated solution. To make a thick viscous gel, "ethylene glycol," was mixed, followed by maintaining at 150-160 °C on a magnetic stirrer with continuous mixing. This hardened gel was crushed into powder and it was heated at 700 °C for 4 h to get

monophasic material. Finally, it was made into pellets and heated at 700 °C and 1200 °C . The samples were named as LSMO-700 and LSMO-1200.

The prepared samples were characterized structurally by XRD measurements by using "Philips x-ray diffractometer" with Cu-Kα radiation source (λ = 1.5406 Å). The surface morphology and composition of the samples were analyzed by FESEM (Carl-ZEISS, ULTRATM-55) attached with EDX spectrometer. The microstructure, particle size and shape were analyzed by using (FEI Tecnai 200 kV D2083) TEM. The *M-H* loops of the samples at different temperatures were measured by using VSM (LakeShore' 7410, USA) .

3.2.3 Results and discussions

3.2.3.1. X-ray diffraction

The XRD measurements were carried out for LSMO-700 and LSMO-1200 samples at RT. The measured diffraction patterns has been shown in Fig. 3.13. From the figure it is clear that polycrystalline single phase of LSMO is successfully synthesized. The Rietveld refinement also confirms the quality of the samples. The XRD data of these samples were also compared with standard data with (JCPDS no. 00-022-1899). It is having a rhombohedral structure with $R\bar{3}c$ space group. As it can be observed from Fig. 3.13 that (012), (110), (202), (024), (116), (214), (208) and (036) are the dominant reflections proving that the samples are stabilizing in perovskite structure. As the sintering temperature increases, the intensity of the peaks are enhancing, but the FWHM decreasing. The increase in intensity results in increased crystallinity, whereas the reduction of FWHM results in increase in particle size of the samples.

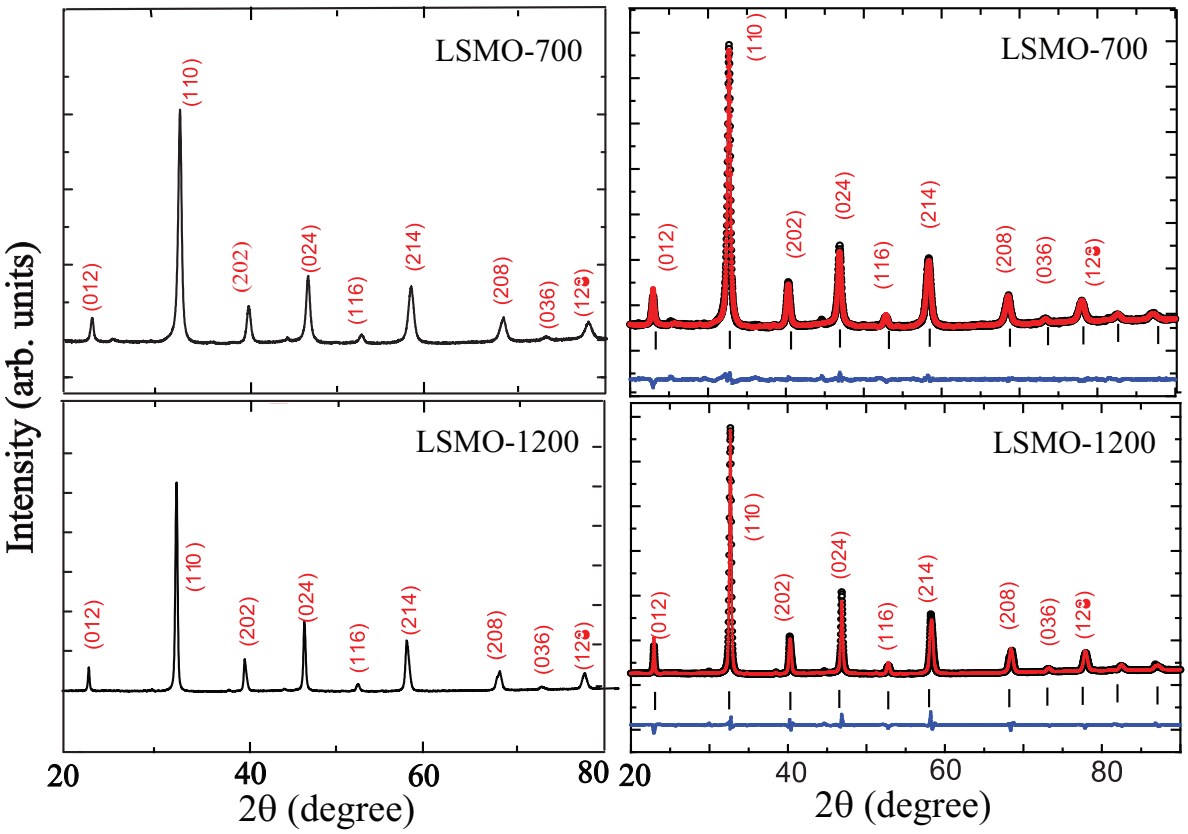

FIGURE 3.13: The room-temperature XRD patterns of LSMO samples along with Rietveld refinement of the patterns.

TABLE 3.2: The crystallographic data of LSMO samples.

Sample	LSMO-700	LSMO-1200
a (Å)	5.504	5.499
b (Å)	5.465	5.467
c (Å)	7.729	7.750
Volume	232.5	233.1
R_p	11.8	13.1
R_{wp}	9.28	11.4
R_{exp}	5.25	4.41
Crystallite size (nm)	37	64
La (x, y, z)	0.0118, 0.0112, 0.2500	0.0105, 0.0110, 0.2500
Sr (x, y, z)	0.0118, 0.0112, 0.2500	0.0118, 0.0112, 0.2500
Mn (x, y, z)	0.5000, 0.0000, 0.0000	0.5000, 0.0000, 0.0000
O (x, y, z)	0.0108, 0.4921, 0.2500	0.0006, 0.5038, 0.2500

From Rietveld refined data, the lattice parameter values have been obtained. All the crystallographic parameter values are tabulated in Table 3.2. The "Scherrer's formula" was employed to estimate the crystallite size.

$$\beta = \frac{k\lambda}{Dcos\theta} \tag{3.5}$$

where, β denotes the experimental "FWHM" of XRD peak, D is the "average crystallite size", k is "grain shape factor", λ is "wavelength" of Cu-Kα (1.5406 Å) radiation source. It has been found that with increasing temperature from 700 °C to 1200 °C, the crystallite size increases, which shows that the crystallites are coalescing to form bigger crystals. The average crystallite size and microstrain of the samples were calculated from the y-intercept and slope of linear fit of $\beta cos\theta$ versus $sin\theta$ plots, respectively. Figure 3.14 shows the W-H plots of the LSMO samples.

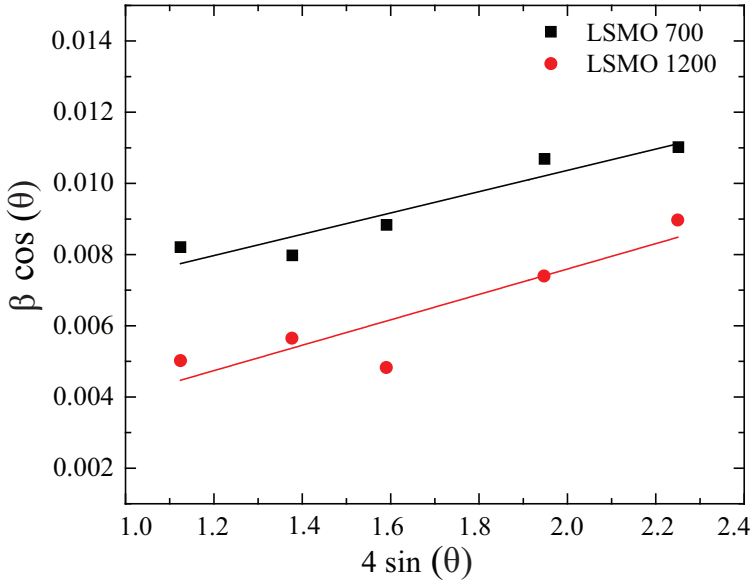

FIGURE 3.14: The Williamson-Hall plot for the LSMO-700 and LSMO-1200 samples.

3.2.3.2. FESEM

In the case of LSMO, the morphological characterizations are done for LSMO-700 and LSMO-1200. Fig. 3.14 (a) and (b) shows the FESEM images of LSMO-700 and LSMO-1200, respectively. As it can be seen, the size of the grains are larger in case of LSMO-1200 as compared to LSMO-700, meaning that the grains are coalescing and become bigger in turn decreasing the surface energy of the system.

3.2.3.3. TEM

Fig. 3.15 (c) and (d) shows the TEM images of the LSMO-700 and LSMO-1200 sample. As it can be seen, a little change in "particle size" with increase in temperature. The inset in Fig. 3.15 (d) shows the SAED pattern of the sample. This confirms the polycrystallinity of the samples.

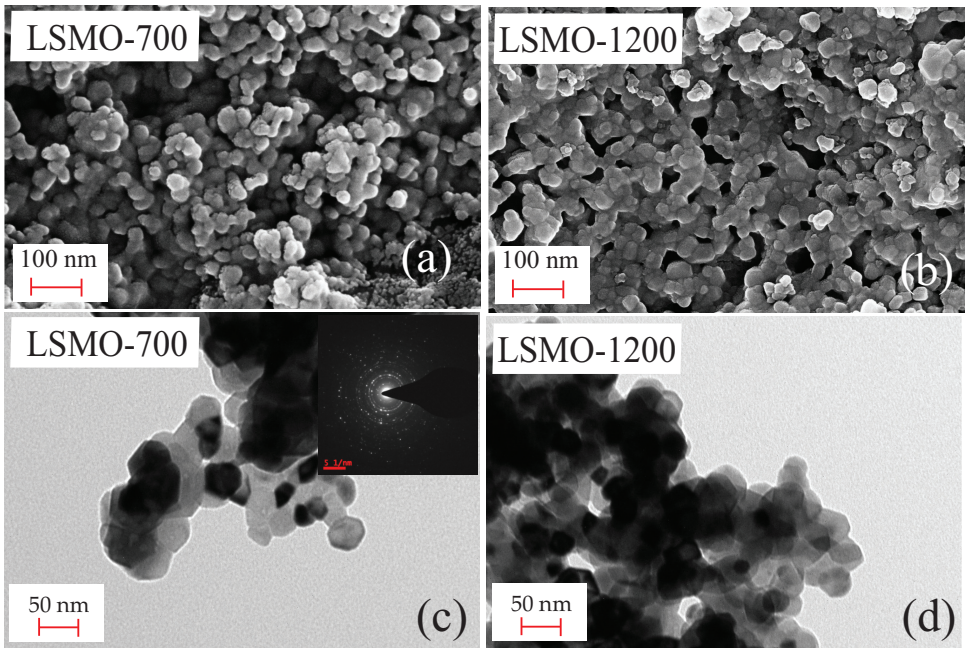

FIGURE 3.15: The FESEM micrographs of LSMO samples.

3.2.3.4. Magnetic properties

Fig. 3.16(a) and (c) shows the *M*-*H* loop of the LSMO samples sintered at different temperatures. Fig. 3.16 (b) and (d) shows the *M*-*T* measurement for LSMO-700 and LSMO-1200 respectively. From the "*M*-*H* loop" at 300 K for LSMO particles and exhibits FM behaviour at RT and the value of M_S comes out to be 37 emu/g and is in agreement with the existing literature [30]. As it can be observed, the coercivity has decreased with increase in temperature. This can be attributed to the "pinning of spins" at the grain boundaries. The dM/dT versus T graphs (shown in inset of Fig. 3.16 (b) and (d)) obtained from *M*-*T* plots of LSMO sample shows a sharp FM to PM transition, which supports the nature of "single-phase" of LSMO.

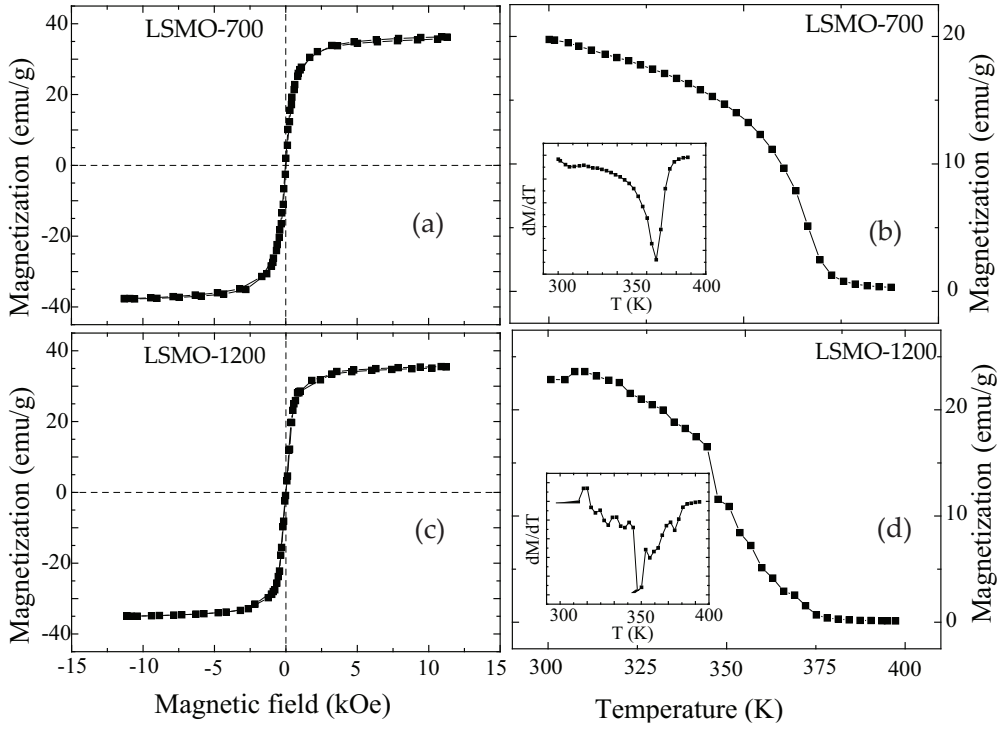

FIGURE 3.16: (a) and (c) M-H loops of LSMO-700 and LSMO-1200 respectively; (b) and (c) M-T plots of LSMO-700 and LSMO-1200 respectively

3.3 Summary

In summary, different shapes and sizes of CFO particles (from 7 to 780 nm) were successfully prepared by varying the sintering temperature (from 300 to 1200 °C) using a polymetric method via the thermal decomposition process. The XRD confirmed the samples' "single-phase" formation, and Rietveld refinement of the XRD data confirmed the cubic crystal structure with $Fd\bar{3}m$ space group. The morphology, microstructure, and particle size of samples changed dramatically when the sintering temperature was changed, resulting in "spherical", "pyramidal", "lamellar", "octahedral", and "truncated octahedral" shapes. The transition of M switching mechanism from "coherent rotation" ("single domain") to "non-coherent rotation/domain wall motion" is clearly demonstrated by the variation of magnetic parameters as a function of particle size in these samples ("multidomain"). These "single-domain" nanoparticles—"spherical" and "pyramidal" (14 nm) and "pyramidal" (21 nm)—show BH_{max}, at 5 K and 300 K, because of a strong correlation between magnetic anisotropy and particle shapes. In appropriate device applications, samples with significant BH_{max} and "single-domain" nature in compressed bulk form can be suitable alternatives to "rare-earth permanent magnets".

Also, LSMO samples were prepared successfully at 700 °C and 1200 °C by sol-gel method. The morphology and particle size shows an increase in grain and particle

size respectively with increase in temperature. The temperature dependent magnetic measurements shows it to be FM well above RT. Hence this material can be used for making magnetic devices and sensors for RT applications.

References

[1] A. P. Guimaraes, Principles of nanomagnetism (New York: Springer) p 19 (2009).

[2] J. M. D. Coey, IEEE Trans. Magn. **47** 4671 (2011).

[3] D. Goll, R. Loeffler, J. Herbst, R. Karimi and G. J. Schneider, J. Phys.: Condens. Mater. **26** 064208 (2014).

[4] P. C. Dent, J. Appl. Phys. **111** 07A721 (2012).

[5] R. B. Falk and G. D. Hooper, J. Appl. Phys. **32** S190 (1961).

[6] C. N. Chinnasamy, B. Jeyadevan, K. Shinoda, K. Tohji, D. J. Djayaprawira, M. Takahashi, R. J. Joseyphus and A. Narayanasamy, Appl. Phys. Lett. **83** 2862 (2003).

[7] A. L. Ortega, E. Lottini, C. J. Fernandez and C . Sangregorio, Chem. Mater. **27** 4048 (2015).

[8] S. Oyarzun, A. Tamion, F. Tournus, V. Dupuis and M. Hillenkamp, Sci. Rep. **5** 14749 (2015).

[9] D. Peddis, C. Cannas, G. Piccaluga, E. Agostinelli and D. Fiorani, Nanotechnology **21** 125705 (2010).

[10] M. Y. Rafique, L. Pan, Q. Javed, M. Z. Iqbal and L. J. Yang, J. Nanopart. Res. **14** 1189 (2012).

[11] N. Murillo, Nanotechnology **15** S322 (2004).

[12] P. N. Oliveira, D. Alanis, R. D. Bini, D. M. Silva, G. S. Dias, I. A. Santos, L. F. Cotica, R. Guo and A. S. Bhalla, Int. Ferroelectr. **174** 88 (2016).

[13] G. K. Williamson and W. H. Hall, Acta Mater. **1** 22 (1952).

[14] S. Laureti, G. Varvaro, A. M. Testa, D. Fiorani, E. Agostinelli, G. Piccaluga, A. Musinu, A. Ardu and D. Peddis, Nanotechnology **21** 315701 (2010).

[15] A. Moriyama, V. Madigou, C. Pereira-de-Souza and C. Leroux, Powder Technol. **256** 482 (2014).

[16] Z. L. Wang, J. Phys. Chem. B **104** 1153 (2000).

[17] Z. L. Wang and X. J. Feng, Phys. Chem. B **107** 13563 (2003).

[18] R. M. Bozorth, E. F. Tilden and A. J. Williams, Phys. Rev. B **99** 1788 (1955).

[19] S. Chikazumi, Physics of ferromagnetism (New York: Oxford University press) p 506 (1997).

[20] I. C. Nlebedim, Y. Melikhov and D. C. Jiles, J. Appl. Phys. **115** 043903 (2014).

[21] S . Chakraverty and M. J. Bandyopadhyay, J. Phys.: Condens. Mater. **19** 216201 (2007).

[22] S. A. Majetich, J. H. Scott, E. M. Kirkpatrick, K. Chowdary, K. Gallagher and M. E. McHenry, Nano Struct. Mater. **9** 291 (1997).

[23] A. P. Guimaraes, Principles of nanomagnetism (New York: Springer) p 37 (2009).

[24] K. H. J. Buschow, Hand Book of Magnetic Materials (Amsterdam: Elsevier) p 212 (1995).

[25] D. J. Craik, Magnetic Oxides part 2 (New York: Wiley) p 703 (1975).

[26] T. Ibusuki, S. Kojima, O. Kitakami and Y. Shimada, IEEE Tran Mag. **37** 2223 (2001).

[27] O. Gutfleisch, M. A. Willard, E. Bruck, C. H. Chen, S. G. Sankar and J. P. Liu, Adv. Mater **23** 8219 (2011).

[28] S. Ravi and A. Karthikeyan, Physics Procedia **54** 45 (2014).

[29] M. Saleem and D. Varshney, RSC Adv. **8** 1600 (2018).

[30] S. P. Pati and T. Taniyama, J. Phys. D: Appl. Phys. **53** 054003 (2019).

Chapter 4

Structural, morphological and magnetic properties of CFO thin films

4.1 Introduction

The thin films of CFO are excellent systems for "high-density magnetic and magneto-optic" recording due to their high H_C, "magnetic anisotropy", and T_C well above the RT. The chemical stablity of this ferrite is an additional advantage for device applications [1–4]. In many magnetic device, CFO thin film has been used as a "pinning layer" in "spin valve" structures and as a "spin filter" in "magnetic tunnel junctions" [5]. However, the enhancement of M of the CFO layer for some of its prospective uses, technological solutions are necessary. The bulk CFO exhibits an "inverse spinel structure", with half of the Fe^{3+} ions on "tetrahedral" (A) sites and the other half on "octahedral" (B) sites [6]. The CFO has been extensively studied for MEs in bulk and heterostructure forms, owing to its magnetoelastic characteristics [7]. The crystallographic structure, residual stresses, thickness, etc., may play a significant role in defining its attributes mostly because of its implementation [8]. The interface effect and microstructure have been acknowledged as major factors in determining coercivity and other magnetic characteristics in related investigations [9]. The growth behaviour was investigated as function of thickness which has been varied by changing the deposition time. The deposited films were characterized and physical properties were studied in connection with the deposition conditions.

4.2 Experimental

PLD was used to produce CFO films of various thicknesses on Pt-coated Silicon substrates by changing the number of laser pulses. For all of the deposited films, a "KrF excimer" gas laser with a λ of 248 nm, a laser fluence of 1.15 J/cm^2 and a repetition rate of 5 Hz has been used. A series of six thin film samples with varying thicknesses

of 115 nm, 125 nm, 160 nm, 175 nm, 250 nm and 300 nm were deposited. The corresponding deposited films named as CFO-115, CFO-125, CFO-160, CFO-175, CFO-250 and CFO-300 respectively. The deposition was carried out in an Excel Instruments chamber with the target kept at 45 ° to the laser pulse and collinear to the substrate, which is maintained in a vertical position. The substrate was maintained at 4 cm distance from the target. Prior to each growth, the base pressure is maintained at 3×10^{-6} Torr. Infact, several factors that affect film quality, namely substrate temperature (T_s), oxygen partial pressure (P_{O2}), and annealing temperature (T_a), are adjusted by systematically to determine the appropriate condition for film deposition. Here in the present case, T_s was fixed at 550 °C, P_{O2} was kept at 1.3×10^{-2} Torr throughout deposition, and the T_a was kept at T_a = 650 °C with an increased P_{O2} of 250 Torr for 2 h. The XRD (PANalytical X'Pert3) was used for structural characterization. The morphological analyses was carried out by utilising a "Carl-ZEISS, ULTRATM-55 FESEM" coupled with EDX spectrometer to validate the composition of the deposited films. The film thickness was estimated by using surface profilometer at three different locations and the average thickness was estimated. The surface smoothness and topography of the films were investigated by using AFM. The magnetic topography of the films were also examined by using MFM. As the magnetic flux emanating from the sample surface is strong enough for domain creation, the lift height was kept constant at 30 nm for the thickest sample and it was followed for the next subsequent samples. VSM has been used to carry out magnetic measurements both "in-plane" (IP) and "out-of-plane" (OP) (LakeShore' 7410, USA) with a maximum applied H-field of 20 kOe. For the OP measurements, the sample was kept perpendicular to the field direction.

4.3 Results and discussion

4.3.1 Structural analysis

The XRD data collected for CFO films deposited on Pt-coated Silicon substrate (Pt-Si) shows the formation of single phase with no trace of any secondary phase. The XRD pattern of the target and the films have been presented in Fig. 4.1(a) and Fig. 4.1(b) respectively. The XRD pattern confirms the growth of the CFO films to be oriented along its [111] direction. The reason behind was explained by Mishra et al., according to them, in spinel ferrites closed packed (111) planes have the lowest surface energy making it energetically favorable for the growth [10]. The peaks corresponding to the Miller indices (311) and (511) also appears and intensifies with the increase in thickness. A systematic variation in peak position with the change in thickness was not observed showing the presence of non-uniform strain in the films.

The percentage of lattice mismatch (δ) between platinum coated silicon substrate and CFO films was calculated taking the lattice parameter of Platinum (a_{Pt} = 3.920 Å) and CFO (a_{CFO} = 8.390 Å)

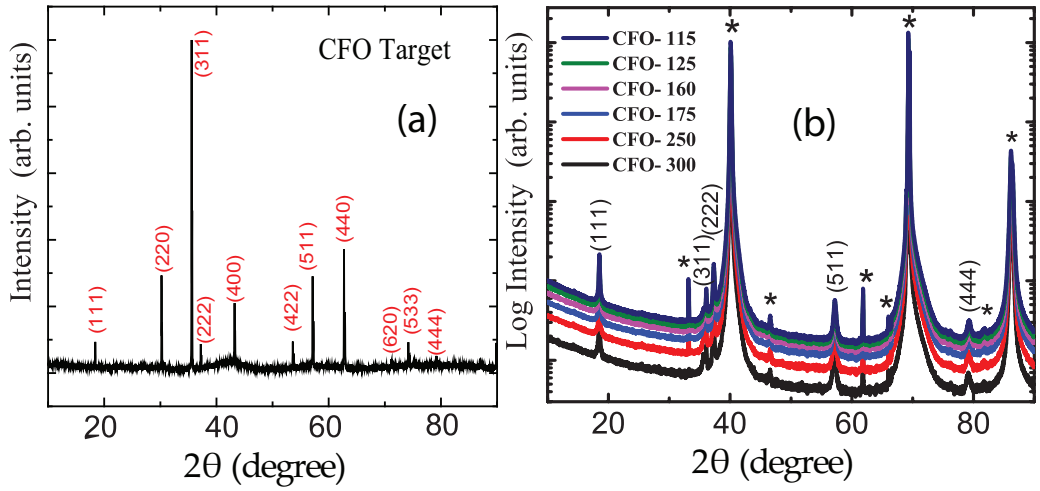

FIGURE 4.1: XRD peaks of cobalt ferrite thin films with varying thickness.

$$\delta = (2a_{Pt} - a_{CFO})/a_{CFO} \tag{4.1}$$

The δ value comes out to be -6.2%, indicating a compressive strain imposed on the CFO film due to substrate. In general, there are two types of residual stress in thin films: intrinsic and extrinsic residual stress [11]. The film growth circumstances such as the stress due to epitaxial nature, stress due to phase transition i.e. changes in phase or structure, stress due to defect, etc. will contribute to intrinsic residual stress (related to the defects). The stress due to epitaxial and phase transition are unlikely to exist in our films, although stress due to defect is possible. The difference in the "thermal expansion coefficient" of the film and the substrate causes extrinsic residual stress. An IP "isotropic" tension will be produced in CFO film as a result of this mismatch after cooling from deposition temperature to RT. Despite its thinness, the Pt under layer has a thermal expansion coefficient of around K_1 = 9x10^6 °C, which is lower than CFO, meaning that the heat expulsion rate differs for these two materials and hence a strain will be generated. This generated strain is expected to have influence on morphology.

As it can be noticed from the XRD pattern, CFO films have grown in an oriented way. One set of plane is oriented towards [111] and has been considered as symmetric planes; the (311) and (511) planes are considered as asymmetric planes. The lattice parameter is calculated for both the cases separately. It is observed that there is an increase in the value of lattice parameter as the film thickness increases for the symmetric planes. Similar trend has been observed for the asymmetric planes. This change in lattice parameter can be ascribed to the strain generated in the film by the substrate because of lattice mismatch. The strain generated has been calculated using,

$$Strain\% = (a_{sample} - a_{bulk})/a_{bulk}) \times 100\% \tag{4.2}$$

The calculated strain values are tabulated on Table 4.1. The tabulated values indicate that there is reduction in strain with the enhanced film thickness. This shows that as the increase in film thickness effects the strain gradually and resulting the value of lattice parameter close to the values of bulk sample (a_{bulk} = 8.362 Å). The negative sign indicates that there is a tensile strain in the lattice.

TABLE 4.1: Variation of lattice mismatch, induced strain with the change in thickness of CFO films.

Sample code	Lattice parameter (symmetric) a_s (Å)	Lattice parameter (asymmetric) a_a (Å)	a_s-a_a (Å)	Strain % (symmetric) (Å)	Strain % (asymmetric) a_s (%)	δ_s(%) (symmetric) a_a (%)	δ_a(%) (asymmetric)
CFO-115	8.332	8.304	0.028	-0.35	-0.691	-6.282	-5.919
CFO-125	8.332	8.304	0.028	-0.35	-0.691	-6.282	-5.918
CFO-160	8.337	8.304	0.029	-0.332	-0.691	-6.301	-5.919
CFO-175	8.337	8.306	0.032	-0.291	-0.669	-6.344	-5.942
CFO-250	8.339	8.306	0.034	-0.262	-0.669	-6.376	-5.942
CFO-300	8.344	8.308	0.036	-0.212	-0.642	-6.429	-5.971

4.3.2 Morphological analysis

4.3.2.1 FESEM

Figure 4.2(a-f), shows the surface FESEM micrographs of the grown CFO films. Figure 4.2(g) depicts the composition of the film estimated from EDAX. The estimated compositions of the constituent elements are in agreement with the nominal composition of the CFO proving the quality of the CFO films. Figure 4.2(h) shows the thickness of the film obtained through cross sectional FESEM and it comes out to be 300 nm which is in agreement with the surface profilometer measurement. The 3-D cluster island growth also can be observed from these micrographs. As the thickness of the film is increasing, the cluster size is also found to increase significantly. This kind of growth mechanism is referred to as Stranski-Krastinov growth (details are already mentioned in Chapter-2).

The arrival of constituent atoms of the film on empty substrate regions or pre-existing "cluster" surfaces usually determines the film growth (nucleation) pace on a substrate. The "diffusion" of these atoms over the substrate or cluster surface results in the formation of mobile or stationary clusters. The atoms can also attach to pre-existing film-atom clusters. The atoms can also re-evaporate from the substrate/cluster. Also the atoms can get separated from a "cluster" and exist on the surface of the substrate. The overall "free energy" of a cluster in relation to the collection of the atoms will determine the balance between growth and dissolution of the cluster. If the "derivative of the free-energy" change with respect to an atom in the cluster is positive. Then the cluster is unstable and will decrease further. If the derivative is negative, the cluster size is stable and will expand at a constant rate.

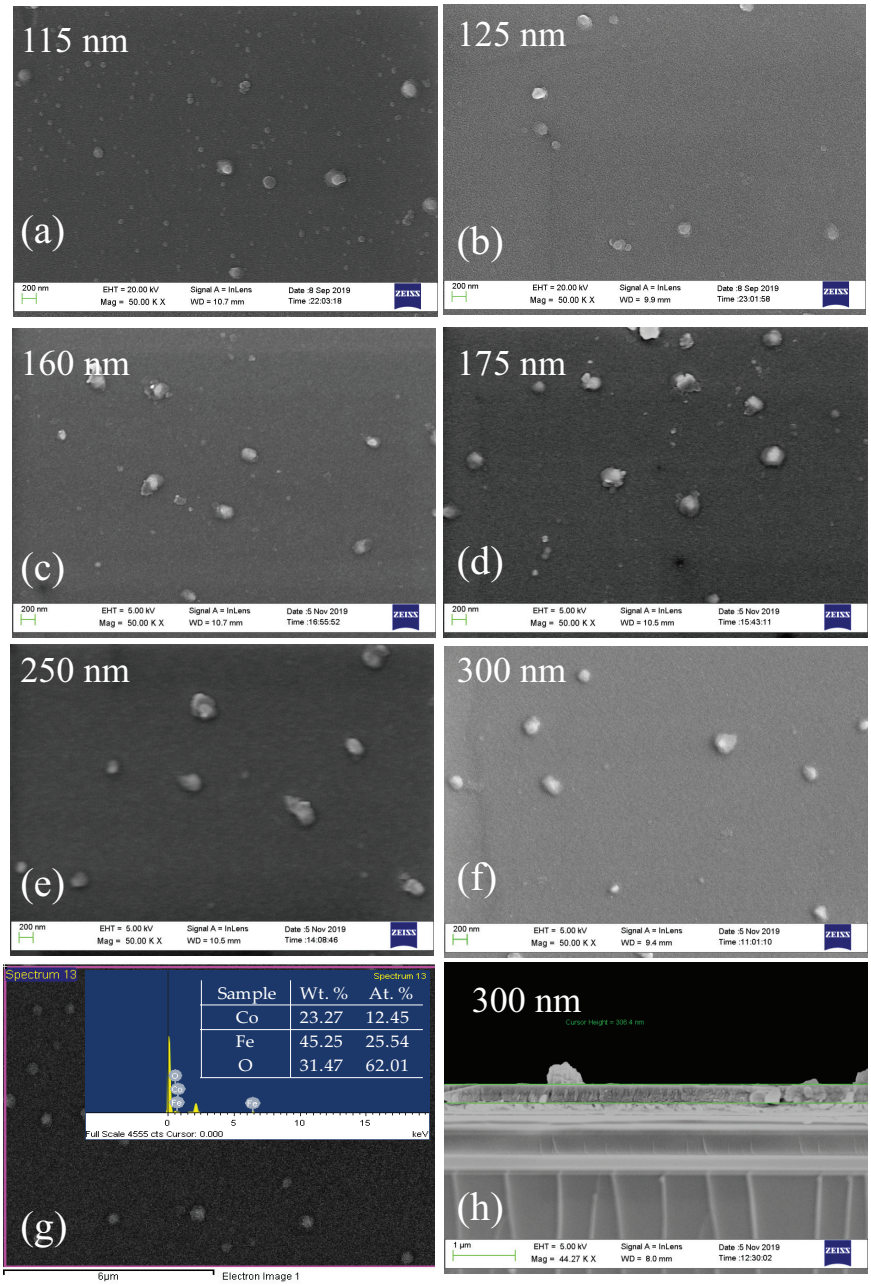

FIGURE 4.2: (a)-(f) FESEM images of the sample with varying thickness. (g) Inset shows the composition of the samples obtained through EDAX. (h) Thickness of a 300 nm film obtained through cross sectional FESEM.

The cluster nucleation rate will grow as the size of the negative "volume free energy" increases [12]. The "volume free energy per unit volume" of the cluster is given by,

$$\Delta G_v = -\frac{k_B T}{\Omega} ln(P/P_e) \tag{4.3}$$

here, P is "pressure of the arriving atoms", P_e is "equilibrium vapour pressure of the film atoms", k_B is "Boltzmann's constant", T is "absolute temperature" and Ω is "atomic volume" of atoms in film. When the cluster is small, the addition of atom increases the cluster size and hence the total "free energy", till a critical nuclear size is reached and from there it decreases upon addition of furthermore atoms. This happens when the volume free energy is negative and the net "surface energy" is positive. The negative gradient of cluster "number density" with respect to cluster size will balance the net negative growth rate of clusters smaller than the "critical size" in steady state [13].

4.3.2.2 MFM and AFM

To observe the magnetic morphology of the surface, the MFM imaging was recorded. Figure 4.3 (a-h) shows the MFM images. As it can be observed, the bright spots refers to the repulsive magnetic force gradient and dark spots refers to attractive magnetic force gradient.

The reason behind the formation of domains (shown in Fig. 4.3(a-h)) can be attributed to minimization of the competing energies arising because of "magneto-static interaction" among exchange coupling, spins, anisotropy and Zeeman energy due to applied field and "magneto-elastic interactions" [14]. The domain formation in thin films is determined by the link between "magnetostatic energy" and "anisotropy energy". The film's "effective anisotropy" (k_{eff}) is the sum of its surface and volume anisotropy. The volume anisotropy increases as the thickness increases, and when it is similar to the "surface anisotropy", the system separates into domains. In this case, the "magnetostatic energy" generated by flux closure is sufficient to sustain domain creation. In the present investigation, MFM of CFO films was probed using a magnetic tip with a height of 30 nm from the film's surface. Here the magnetic domains with two distinct contrasts are visible in our MFM photographs. Because MFM is an important tool to measure OP signal and can be used to capture the MFM picture at equilibrium, the M is classified as parallel or antiparallel to the surface normal. The "domain size" is assessed by running a line scan through the domains at various points, and it is found to be growing. This impact might be caused by the enhanced thickness fast deposition at high temperature [12].

It can be seen in AFM imaging (Fig. 4.3 (g-l)) that as the film thickness grows, the brighter spots of the sample gradually increase, indicating that the roughness of the deposited films increases, which may be the plausible reason for the growth of clusters or islands. The surface morphology changes when misfit dislocations arise in thicker films due to the presence of strain field around the dislocations [15].

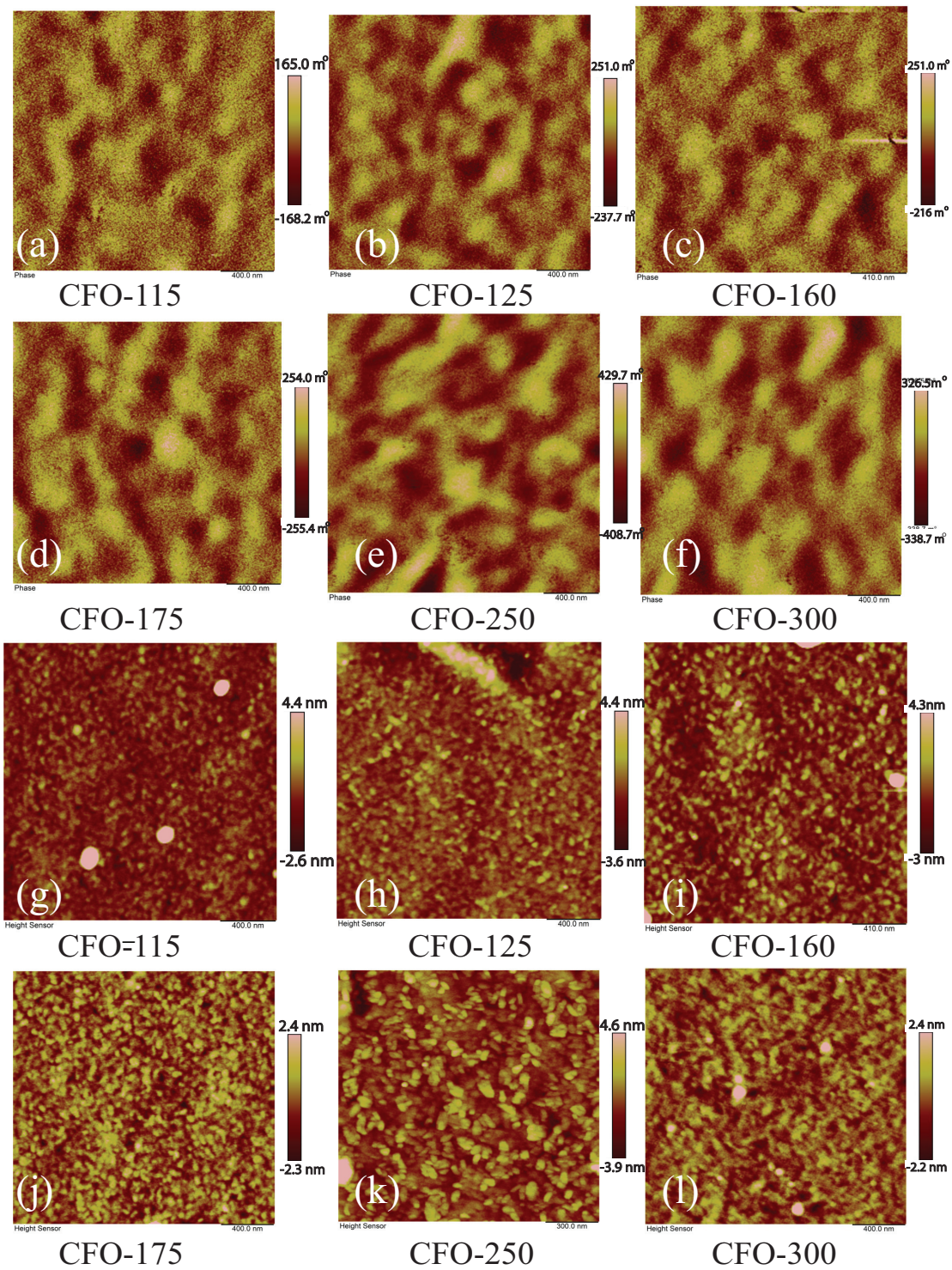

FIGURE 4.3: (a)-(f) Magnetic force microscopic images of the samples showing re-orientation of the spin of the samples with increasing thickness. (g)-(l) Atomic force microscopic images of the samples showing the graineness of the samples with increasing thickness.

The islands occur on the surface when dislocations nucleate resulting the roughness in the systems, and this islands may be seen in AFM images. The existence of islands/roughness indicates that the film is getting relaxed and dislocations are forming [15].

4.3.3 Magnetization

The *M-H* loops of the CFO films, measured by VSM at RT and are presented in Fig. 4.4 (a-f). Both IP and OP magnetic measurements were carried out on the samples. The diamagnetic correction was done by subtracting the M values of the substrate from the deposited sample. It is evident from the graphs that the H_C of the CFO thin films shows a change for both the IP and OP measurements as the thickness of the films increases. As it is clear from the figures,that with the increase in thickness of the films, the M_S also shows a similar behaviour as H_C, both for IP and OP M values. The observation is according to the "Stoner– Wohlfarth model" of oriented uniaxial anisotropy that the "easy axis" of M is IP and "hard axis" is OP [16]. To attribute this strong "in-plane magnetic anisotropy" in CFO films, many parameters should be taken into account, and they add to the magnetic energy [8].

The parameters, M_S and H_C, are given in Fig. 4.5. It is important to observe that here M_S is not the actual M_S of the film and only reported as technical M_S at 20 kOe. The values of in-plane M of films are in the range of 100–175 emu/cc and 30-105 emu/cc for OP M at 20 kOe, which are compatible with polycrystalline CFO films deposited using PLD on Pt coated SiO_2/Si substrate at PO_2 = 0.13 mTorr and at a temperature 550 °C. However, these values are less than M_S of bulk CFO (425 emu/cc) [11].

The reduction in IP M_S with increasing film thickness suggests that the cation distribution is reaching its thermodynamic equilibrium condition for higher film thicknesses. This finding demonstrates that a local heating occurs during the deposition of thicker films, causing the temperature of the already formed layer to increase above room temperature. As the film thickness increases, the latter portion of the film will be grown efficiently at a higher T_S, resulting in a decreased cooling rate. This would result in a cation distribution that is significantly closer to the inverse spinel ferrite's thermodynamically equilibrium distribution, and hence a smaller M_S is obtained. Thus we get an understanding about our result, why the M_S is found to decrease with the increasing film thickness, in spite of the increasing "grain size" [17]. In addition, as seen in the figure, the M_S decreases sharply when the thickness of the film is reduced (below 150 nm), which might be due to thin layer with different magnetic characteristics near to the film interface [8, 18–20]. Moreover, in the case of OP M_S, when the thickness is less, the number of clusters or islands are less and obviously the resulting M will be less. But with the increase in thickness, the cluster number and size increases resulting in an increase in OP M (which includes parallel and anti-parallel OP, and tilted ones). As more and more number of CFO molecules are orienting in that direction increasing the M till a critical thickness is

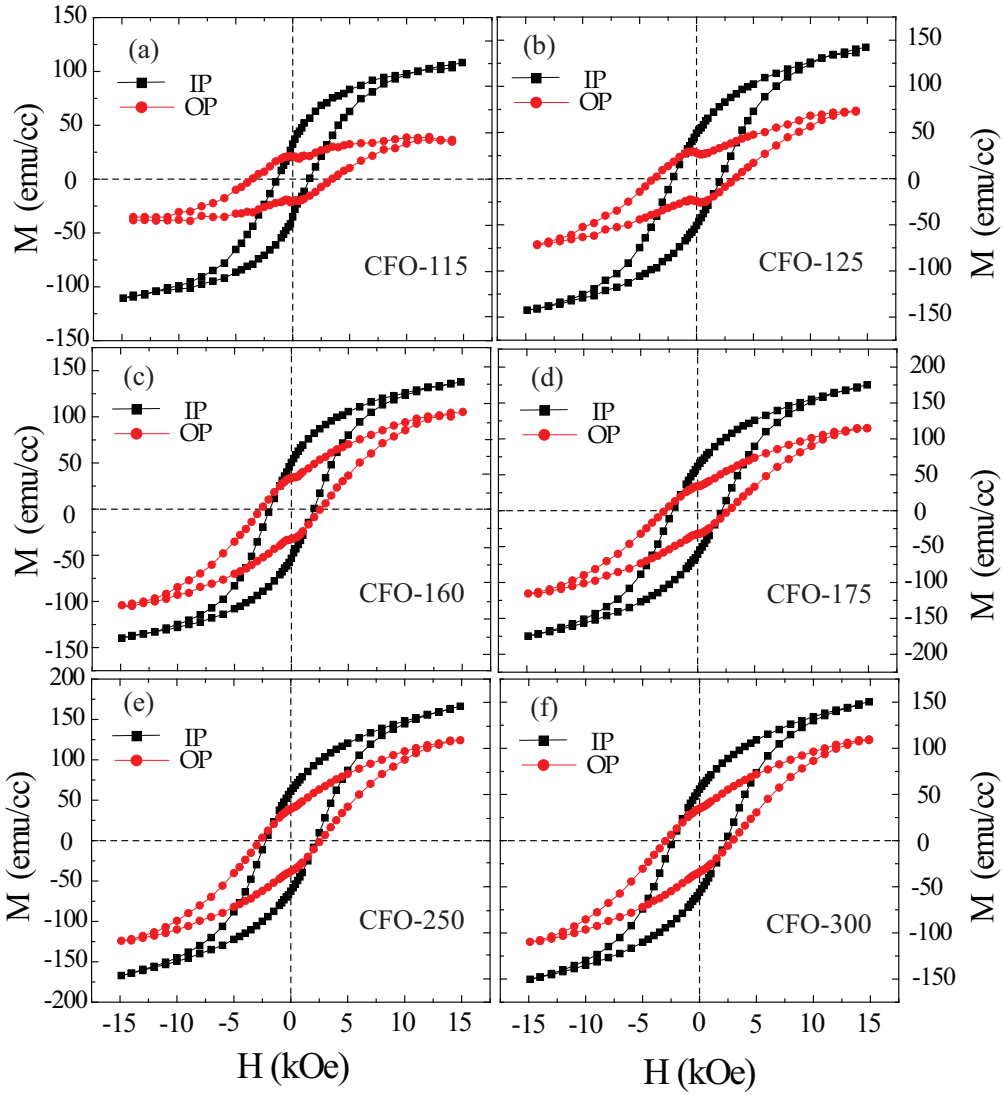

FIGURE 4.4: (a)-(f) IP (represented by black dots) and OP (represented by red dots) $M - H$ loops with the change in film thickness at RT.

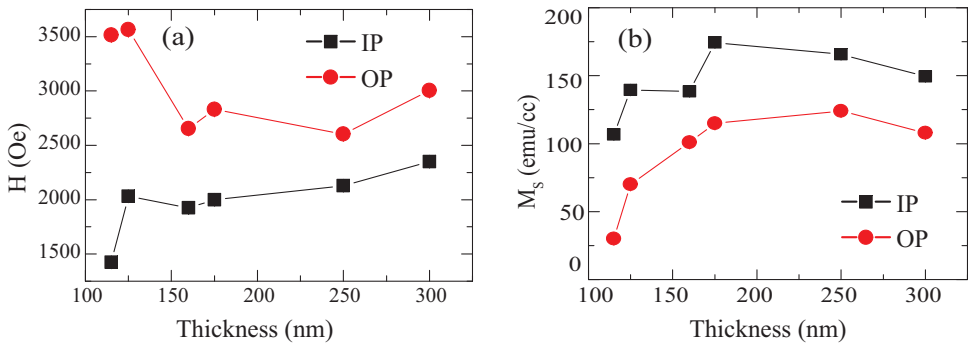

FIGURE 4.5: (a)Variation of H_C for IP and OP samples with increase in thickness.(b)Variation of M_S for IP and OP samples with increase in thickness.

reached. After crossing that critical thickness, the contribution from other two directions (parallel or anti-parallel/anti-parallel or tilted/tilted or parallel) increases resulting in the decrease in M.

The H_C is affected by several factors, viz., grain size, strain, defects and MCA. The increase in H_C makes easier for the "domain walls" to move [17].

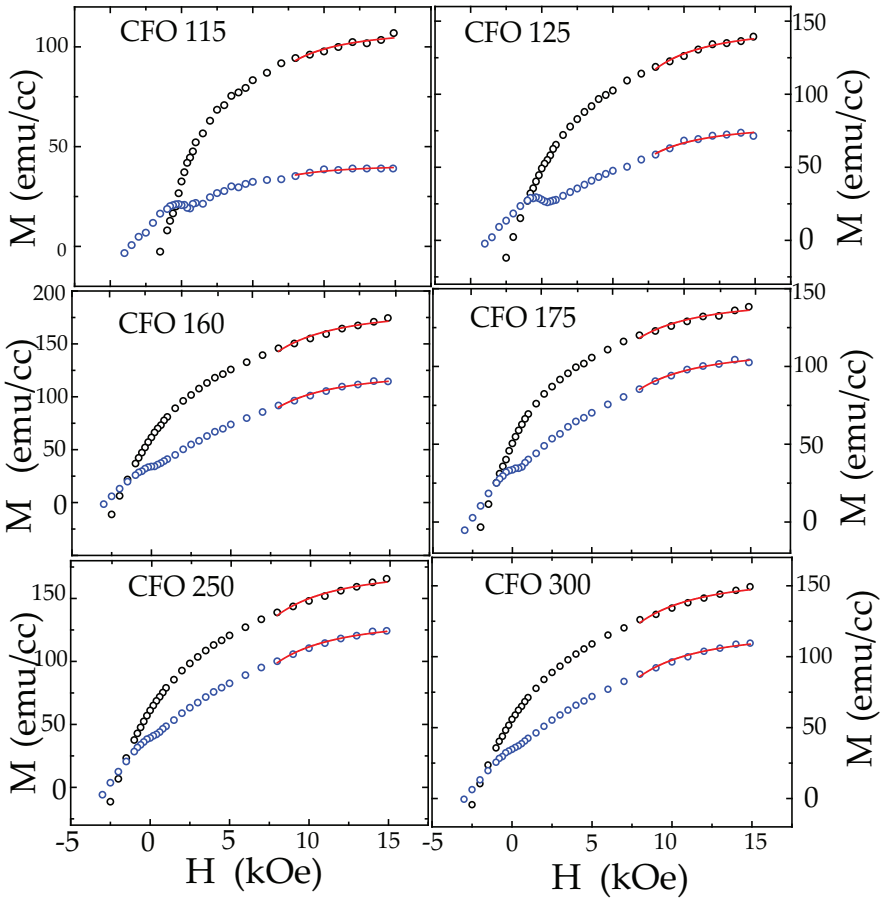

FIGURE 4.6: Law of Approach to saturation fit for CFO thin films of varying thickness.

Figure 4.6 shows the fittings of the IP and OP M-H loops. The "effective magnetic anisotropy constant" (K_{eff}) is an important parameter for understanding the magnetic nature of thin films. The value of K_{eff} was calculated by applying the "law of approach to saturation" given by Chikazumi to a initial M curve. The corresponding equation is shown below:

$$M = M_S(1 - \frac{b}{H^2}) + \chi H \tag{4.4}$$

where, M_S represents the saturation magnetization, $\frac{b}{H^2}$ represents the anisotropy contribution. The term, χH is the induced M arising due to linear increase in M, at high fields and H is "applied magnetic field". The parameter b is given by the following equation,

$$b = 0.0762(\frac{K_{eff}^2}{\mu_0^2 M_S^2}) \tag{4.5}$$

where K_{eff} is "effective magnetic anisotropy constant" and μ_0 is permeability of free space. The equation (4.3) has been used to fit the RT experimental data of virgin curves, and the values of K_{eff} were calculated using the best-fit parameters.

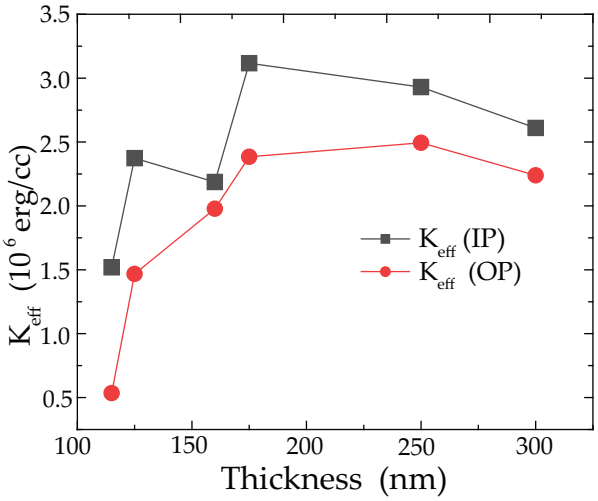

FIGURE 4.7: Variation of effective magnetic anisotropy constant for "in-plane" and "out-of-plane" samples of CFO thin film with increase in thickness.

Figure 4.7 shows the plot of effective magnetic anisotropy constant with the change in thickness. From the figure it is seen that, both IP and OP magnetic anisotropy plot trends similar to H_C. One more interesting observation which can be noted from the plot is that, the obtained anisotropic value is many times larger than the intrinsic MCA of the bulk CFO value [22]. This shows the high values of anisotropy observed in the film deposited on Pt-Si potentially originates from the large stress arising due to the film and substrate "mismatch" [23].

4.3.4 Raman spectroscopy

"Raman spectroscopy" is a fingerprint method for recognising various chemical species in a sample by studying the varied "vibrational modes" of the atoms situated in different places in lattice. It also provides quantitative information on cation arrangement, notably in ferrites. The Raman measurements are beneficial in the current investigation to determine the cation distribution of CFO. Raman measurements are also extremely sensitive to the structure's of the crystal. In light of this, the "Raman spectra" of all the materials were measured at 300 K in the frequency range, 50-2000 cm^{-1}, and the associated spectra are presented in Fig. 4.8. According to group theory, an AB_2O_4 spinel ferrite with $Fd\bar{3}m$ and cubic unit cell shows the following collection of "optical phonon modes" [24, 25].

E_g(R)+ $3T_{2g}$(R)+A_{1g}(R) +4 T_{1u}(IR)+ T_{1g}(IN)+ $2A_{2u}$(IN) +2 Eu(IN)+ $2T_{2u}$(IN)

here, "R, IR and IN" indicated in brackets represent the "Raman", "infrared" and "inactive" vibrational modes, respectively. The subscript "g" and "u" denotes the "symmetric" and "antisymmetric" modes with respect to "centre of inversion". Out of all, the five modes are "Raman active" (viz., E_g + $3T_{2g}$ + A_{1g}) and the next four (viz., T_{1u}) are "IR active", respectively. where, the "vibrational modes" with the designation "T", "E", and "A" denotes the modes in 3-D, 2-D, and 1-D, respectively [26].

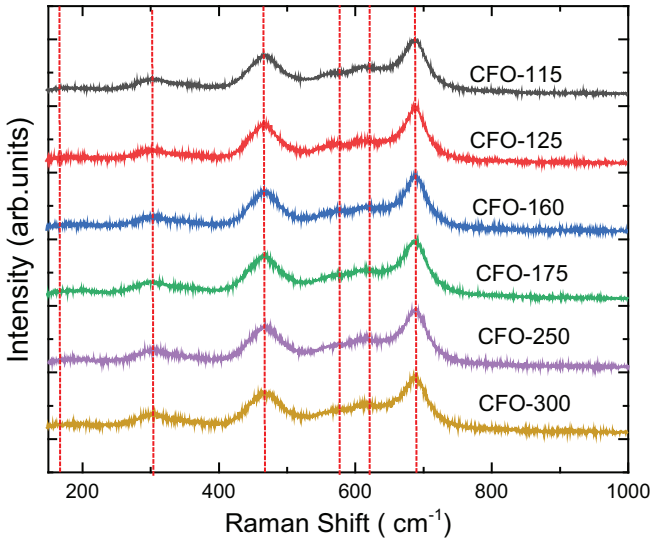

FIGURE 4.8: The room temperature Raman spectra of CFO thin films of varying thickness.

The Raman active modes (E_g + $3T_{2g}$ + A_{1g}) are represented by the spectral peaks found in the range 170 - 800 cm^{-1}. The existence of five Raman peaks in the specified energy range, at first look, suggests the cubic spinel phase, which has been confirmed by XRD data [27]. Due to "symmetric stretching" of "O" atoms with Fe^{2+}, Fe^{3+}, and Co^{2+} cations in the tetrahedra, the high wavenumber first-order broad Raman peak $A_{1g}(1)$ at approximately 690 cm^{-1}, consists of "two shoulder peaks" $A_{1g}(2)$ and $A_{1g}(3)$ at roughly 680 cm^{-1} and 620 cm^{-1} [28]. The prominent $T_{2g}(2)$ "vibrational modes" noticed at 475 cm^{-1} are caused by "antisymmetric stretching" of "Fe" with "O", whilst the noticed sub-peak at 460 cm^{-1} is caused by "antisymmetric stretching" of "Co" with "O" in the cubic spinel structure's octahedral sites. The T_{2g} (3) "vibrational modes" discovered at roughly 570 cm^{-1} indicate the 'antisymmetric' bending of "O" with regard to the metal of the "octahedral" group. The $T_{2g}(1)$ "vibrational mode" is identified at around 170 cm^{-1} due to the "translational motion" of the "tetrahedron", i.e. metal cation at the "tetrahedral" site in conjugation with "O". The 'E_g' mode is caused by the "symmetric" bending of an "O" atom with respect to the metal atoms in "octahedral" locations [29–31]. In fact, the position and intensity of the "Raman" peaks are determined by the vibrating atom's characteristics and quantity, which further accounts for the variations and its polarization nature.

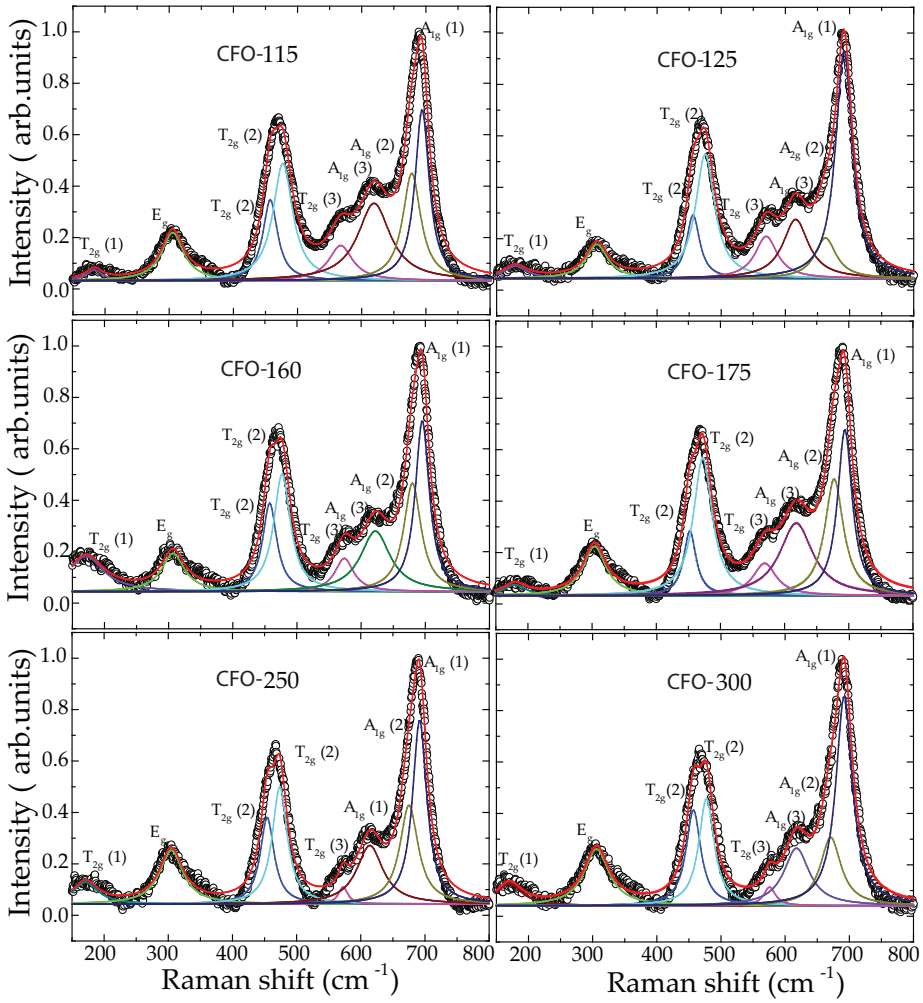

FIGURE 4.9: Lorentzian profile fitted Raman spectra of CFO films at different thickness.

The "symmetric stretching" of Fe, Co ions in the centre of a specific site will vibrate at various frequencies, resulting in wide vibrational peaks in this example. Table 4.2 lists the various vibrational peaks associated with various ions.

TABLE 4.2: The deconvoluted Raman peak positions of CFO samples with varying thickness.

Sample code	$A_{1g}(1)$ (cm^{-1})	$A_{1g}(2)$ (cm^{-1})	$A_{1g}(3)$ (cm^{-1})	$T_{2g}(1)$ (cm^{-1})	$T_{2g}(2)$ (cm^{-1})	$T_{2g}(2)$ (cm^{-1})	$T_{2g}(3)$ (cm^{-1})	E_g (cm^{-1})	$\frac{I(T_{2g}(2)}{I(A_{1g}(1)}$
CFO-115	694	678	619	183	457	477	567	305	0.487
CFO-125	691	662	616	179	456	475	570	306	0.619
CFO-160	695	679	622	171	457	476	573	306	0.522
CFO-175	693	677	617	176	454	473	569	305	0.535
CFO-250	691	675	614	170	454	473	572	304	0.676
CFO-300	692	670	617	170	457	477	575	305	0.471

As shown in the above discussion, the "Raman vibrational modes" above 600 cm^{-1} are caused by "tetrahedral" (AO_4) sub-lattice oscillations, while the "vibrational modes" below 600 cm^{-1} are caused by "octahedral" (BO_6) sub-lattice vibrations, and these findings are consistent with previous studies for other ferrites [27–31]. In order to comprehend the vibrations of the sublattice (viz., "octahedral" and "tetrahedral") and cation site-occupancies as a function of increasing sample thickness, the noticed "Raman peaks" were deconvoluted by "Lorentzian" profile fitting, and best-fitted curves are given in Fig. 4.9. Table 4.2 shows the best-fit peak location values. Because the strength of a "Raman" peak is related to the number of cations in the sub-lattice, the existence of more than one kind of cation results in "shoulder-like" Raman intensity peaks. As a consequence, in this condition, the primary intensities and placements of $A_{1g(1)}$ and $T_{2g(2)}$, which represent the "tetrahedral" and "octahedral" sites, respectively, were thoroughly investigated, and the findings are given in Table 4.2. The ratio of intensity the deconvoluted peaks of $A_{1g}(1)$ and $T_{2g}(2)$ was computed using $I[T_{2g}(2)]/I[A_{1g}(1)]$, and the findings are displayed in Table 4. 2. The ratio, $I[T_{2g}(2)]/I[A_{1g}(1)]$ was used to compute the ratio between $A_{1g}(1)$ and $T_{2g}(2)$. Because all of the samples had the same makeup, the ratios were found to be almost same for all of them. In this situation, the occupancy of many atoms in the "tetrahedral site" is very low, resulting in constant $I[A_{1g}(1)]$, but the occupancy of many atoms in the octahedral sites affects $I[T_{2g}(2)$. As seen in Table 4.2, the vibrational peaks moved towards the lower wavenumber as the thickness increased. This peak shift may be measured by determining the vibrating cation's effective force constant. Since a compound's vibrational frequency is proportional to its "force constant (K)", the force constants of octahedral (K_O) and tetrahedral (K_T) ions were computed using the equations below, [28, 32],

$$K_T = 7.62 \times M_T \times \nu_T^2 \times 10^{-3} \tag{4.6}$$

$$K_O = 7.62 \times M_O \times \nu_O^2 \times 10^{-3} \tag{4.7}$$

where, "M_T" and "M_O" denotes the "molecular weights" of ions in "tetrahedral" and "octahedral" sites. Here, the ν_T and ν_O denotes the frequencies corresponding to the $A_{1g}(1)$ and E_g peaks, respectively. The values estimated for K_T and K_O are shown in Table 4.3.

TABLE 4.3: The force constant, cation distribution and magnetic moment values of CFO samples for different thicknesses.

Sample code	K_T x10^5	K_O x10^5	Cation distribution	Magnetic moment
CFO-115	2.0821	1.1281	$(Co_{0.281}Fe_{0.719})_T$ $(Co_{0.719}Fe_{1.281})_O$	4.819
CFO-125	2.0583	1.1329	$(Co_{0.244}Fe_{0.756})_T$ $(Co_{0.756}Fe_{1.244})_O$	4.543
CFO-160	2.0863	1.1311	$(Co_{0.295}Fe_{0.705})_T$ $(Co_{0.705}Fe_{1.295})_O$	4.918
CFO-175	2.0812	1.1213	$(Co_{0.329}Fe_{0.671})_T$ $(Co_{0.671}Fe_{1.329})_O$	5.168
CFO-250	2.0615	1.1207	$(Co_{0.258}Fe_{0.742})_T$ $(Co_{0.742}Fe_{1.258})_O$	4.649
CFO-300	2.0617	1.1311	$(Co_{0.229}Fe_{0.770})_T$ $(Co_{0.770}Fe_{1.229})_O$	4.442

The obtained K_T and K_O values in Table 4.3 were discovered to decrease as the sample thickness increased. With increasing thickness, the fluctuation in K_T and K_O values may be explained as follows. The "force constant" is inversely proportional to the bond length in general (viz., Fe-O and Co-O). These bond lengths in ferrites will, in fact, affect the lattice parameter. As the thickness increases, the lattice parameter increases, and the Raman peak moves to the lower wavenumber side. Based on the intensity ratio of the obtained Raman data, the cation distribution of these CFO samples have been determined by using the following formula,

$$n_{Raman} = M_B - M_A \tag{4.8}$$

where, "M_A" and "M_B" represent the atomic magnetic moments at A and B positions, respectively. Further, the cation arrangement deduced from Raman measurements (given in Table 4.3), confirms the "inverse spinel nature" of the samples. Further, the approximated cation distribution, the "magnetic moment" (n_{Raman}) values of CFO thin film samples were obtained using "Neel's sublattice model". The estimated magnetic moment (n_{Raman}) given in Table 4.3. The magnetic moment values are in agreement with the values estimated for CFO bulk/nano samples (discussed in the previous chapter).

4.4 Summary

The CFO samples with varying thickness were successfully prepared using PLD technique. The XRD results revealed the films are having single phase with polycrystalline nature. The morphological study shows that there is formation of clusters showing the film to be Stranski-Krastinov growth. The observed clusters on the film indicates an increase in stress due to mismatched lattice between substrate and deposited film. The magnetic measurements clearly show the RT FM behaviour.The

OP magnetic component increases with the increasing thickness that might be because of increment in cluster size or islands. Raman measurements also verify the formation of single phase CFO. Moreover, the magnetic moment was also calculated from the Raman data by analyzing cation distribution of CFO thin films of varying thickness. In this chapter a correlation has been established between the structural and magnetic properties of CFO thin films by studying the structure, morphology and magnetic properties.

References

[1] S. Maat, M. J. Carey, E. E. Fullerton, T. X. Le and P. M. Rice, Appl. Phys. Lett. **81** 520 (2002).

[2] M. J. Carey, S. Maat, P. Rice, R. F. Marks and A. Kellock, Appl. Phys. Lett. **81** 1044 (2002).

[3] A. Lisfi, J. C. Lodder, E. G. Keim and C. M. Williams, Appl. Phys. Lett. **82** 76 (2003).

[4] M. Grigorova, H. J. Blythe, V. Blaskov, V. Rusanov, V. Petkov and V. Masheva, J. Magn. Magn. Mater. **183** 163 (1998).

[5] A. V. Ramos, T. S. Santos, G. X. Miao and M. J. Guittet, Phys. Rev. B **78** 180402 (2008).

[6] A. Goldman, Modern ferrite technology, p 36, second ed., Springer, New York, (2006).

[7] J. Grafe, M. Welke, F. Bern, M. Ziese and R. Denecke, J. Magn. Magn. Mater. **339** 84 (2013).

[8] M. Khodaei, S. A. Seyyed Ebrahimi, Y. J. Park and S. H. Choi, Thin Solid Films **571** 62 (2014).

[9] W. Huang, L. X. Zhou, H. Z. Zeng, X. E. Wei, J. Zhu, Y. Zhang and Y. R. Li, J. Crys. Growth **300** 426 (2007).

[10] R. K. Mishra and G. Thomas, J. Appl. Phys. **48** 4576 (1977).

[11] M. Khodaei, S. A. S. Ebrahimi, Y. J. Park, J. M. Ok, J. S. Kim, J. Son and S. Baik, J. Magn. Magn. Mater. **340** 16 (2013).

[12] V. M. Kumar, A. Srinivas, A. Talapatra, S. Asthana, J. Mohanty and S. V. Kamat, J. Mater. Sci.: Mater. Electron. **28** 446 (2016).

[13] Z. Chen, C. H. Shek and J. K. L. Lai, Phys. B: Condens. Matter **358** 1 (2005).

[14] B. D. Cullity, C. D. Graham, Introduction to Magnetic Materials, p 50, 2nd edn. (Wiley, New Jersey) (2009).

[15] R. Comes, M. Gu, M. Khokhlov, J. Lu and S. A. Wolf, J. Magn. Magn. Mater. **324** 4 (2012).

[16] E. C. Stoner and E. P. Wohlfarth, Philos. Trans. Royal Soc. A **240** 826 (1948).

[17] S. C. Sahoo, N. Venkataramani, S. Prasad, M. Bohra and R. Krishnan, Appl. Phys. A **106** 931 (2011).

[18] T. Niizeki, Y. Utsumi, R. Aoyama, H. Yanagihara, J. Inoue, Y. Yamasaki, H. Nakao, K. Koike and E. Kita, Appl. Phys. Lett. **103** 162407 (2013).

[19] F. Rigato, J. Geshev, V. Skumryev and J. Fontcuberta, J. Appl. Phys. **106** 113924 (2009).

[20] R. Lin, J.H. Liao, L.J. Hung and T.B. Wu, J. Appl. Phys. **103** 07320 (2008).

[21] S. Chikazumi, Physics of ferromagnetism (New York: Oxford University Press) p 506 (1997).

[22] A. Das, K. K. Bestha, B. Prakash and V. Gorige, Nanotechnology **31** 335716 (2020).

[23] T. Dhakala, D. Mukherjee, R. Hyde, P. Mukherjee, M. H. Phan, H. Srikanth and S. Witanachchi, J. Appl. Phys. **107** 053914 (2010).

[24] P. Chand, S. Vaish and P. Kumar, Phys. B **524** 53 (2017).

[25] G. P. Nethala, R. Tadi, G. R. Gajula, P. V. P. Madduri, A. V. Anupama and V. Veeraiah, Mater. Chem. Phys. **238** 121903 (2019).

[26] V. G. Ivanov, M. V. Abrashaev, M. N. Ilaev, M. M. Gospodinov, J. Meen and M. I. Aroyo, Phys. Rev. B **82** 024104 (2010).

[27] S. Thota, S. C. Kashyap, S. K. Sharma and V. R. Reddy, Mater. Sci. Eng. B **206** 69 (2016).

[28] B. Nandan, M. C. Bhatnagar and S. C. Kashyap, J. Phys. Chem. Solids, **125** 298 (2019).

[29] A. Kumar, P. Sharma and D. Varshney, Ceram. Int. **40** 12855 (2014).

[30] J. Jacob and M. A. Khadar, J. Appl. Phys. **107** 114310 (2010).

[31] P. N. Anantharamaiah and P.A. Joy, J. Phys. D: Appl.Phys. **50** 435005 (2017).

[32] R. D. Waldron, Phys. Rev. **99** 1727 (1955).

Chapter 5

Structural and magnetic properties of LSMO/PMN-PT heterostructures

5.1 Introduction

"Magnetic anisotropy" is one of the essential properties of "magnetic materials" and plays a crucial role in many device applications, such as magnetic recording, magnetic "switching" devices, and "magnetoresistive sensors". The magnetic anisotropy of materials in hetero-layers will most likely deviate from the anisotropy of their bulk counterparts due to interfacial relations between the substrate and the corresponding film. As a result, understanding the relationship between strain and magnetic anisotropy of the magnetic material is critical [1]. A suitable choice of substrates, interlayers, and other factors might be used to tune the anisotropy.

The "perovskite" oxides, such as doped manganites, $Re_{1-x}Ae_xMnO_3$(Re = "rare earth metal", Ae = "alkaline earth metal") are an exciting class of materials because they depict a substantial connection between "electron transport", "magnetism", and "crystal lattice distortions", arriving at them very amenable to "charge"- and "strain"-related changes. An oxygen octahedron surrounds a manganese ion in these perovskite structured compounds in manganites. In the case of manganites, the distribution of Mn^{3+}/Mn^{4+} in a formula unit responsible for many physical properties is defined by the doping concentration of "Ae", resulting in a complex phase diagram [2]. This distribution can be affected by interfacial charge, and strain can produce rotations of MnO_6 structure and variations in Mn-O bond [3]. The strain affects orbital occupancy as well. The triply degenerate t_{2g} and doubly degenerate e_g levels of Mn^{3+} in an octahedral crystal field are split into three non-degenerate t_{2g} energy levels, and two non-degenerate e_g energy levels. The Jahn-Teller effect lifts the degeneracy of the e_g orbital occupancy, resulting in a MnO_6 octahedra distortion [3]. By decreasing the symmetry of the crystal field, epitaxial strain exerts a similar effect, favoring one direction of MnO_6 distortions. The conflict between the localizing impact of a strong "electron-lattice coupling" and the e_g electron itinerancy leads to FM because of DE coupling, which governs the physics of doped manganites [2]. Here, in this chapter, the strain-induced changes in M of LSMO has been discussed. The LSMO deposited on PMN-PT substrates of different orientations induces strain,

which propagates through the magnetic layer making M of the LSMO film orient in a particular direction. This chapter clearly demonstrates the magnetic anisotropy of the LSMO films originating because of the orientation of the PMN-PT substrate, and the underlying mechanism has been presented.

5.2 Experimental

The LSMO film with 50 nm thickness was deposited on PMN-PT single crystal substrates orientated along [001], [011] and [111] by using PLD. An Nd: YAG laser with a wavelength of 266 nm was used for the deposition. The substrate was ultrasonicated to eliminate the physisorbed contaminants prior to mounting it in the deposition chamber. The chamber's base pressure was pumped down to 3 $\times 10^{-8}$ Torr. The P_{O_2} of 0.5 Torr was maintained in the chamber, and the substrate temperature was kept at 650 °C. While deposition, the repetition rate of 10 Hz was used for the laser and it's energy was kept constant at 32 mJ. The deposited LSMO film was removed from the chamber and characterized by using XRD. The XRD experiment was carried out using a "Bruker D8 Discover diffractometer" with a Cu-K_α radiation source (λ = 1.5405 Å). The thickness of the deposited layer was examined using a surface profilometer. A VSM (Lakeshore Cryotronics, Inc., 7407) was used to detect IP M-H loops at various rotation angles. The M-T measurements were carried out in the temperature window, 200-400 K with an applied H-field of 100 Oe.

5.3 Results and discussion

5.3.1 Structure

The structural characteristics of LSMO thin films deposited on PMN-PT substrate oriented along [001], [011] and [111] were studied by using the high resolution XRD for OP (θ-2θ) mode. Figure 5.1 depicts the measured XRD patterns of LSMO/ PMN-PT with different orientations. It is worth to note from the figure that the LSMO (0 l l) reflections appear along with the PMN-PT (0 l l) reflections. A thorough examination of PMN-PT XRD data indicates that it has a cubic structure, with $P4mm$ and the estimated lattice parameter of 4.0166 Å, 4.0135 Å, and 4.0062 Åfor PMN-PT oriented along [001], [011] and [111] respectively. The lattice mismatch of the pseudocubic LSMO film was computed taking (001), (011), and (111) reflections of LSMO and found to be -4.3%, -4.06%, and -3.7%, respectively. It is found that a strained interface causes a change in lattice parameters. The negative sign here indicates the presence of "tensile strain" in the LSMO film [4]. As the size of the lattice mismatch is less than 5 %, LSMO growth on PMN-PT comes out to be epitaxial/oriented, as evidenced by the (001), (011) and (111) reflections of the XRD pattern for three different oriented samples [5]. The substrate's preferred orientation promotes the epitaxial development of the film, LSMO. The film's epitaxial development on the substrate

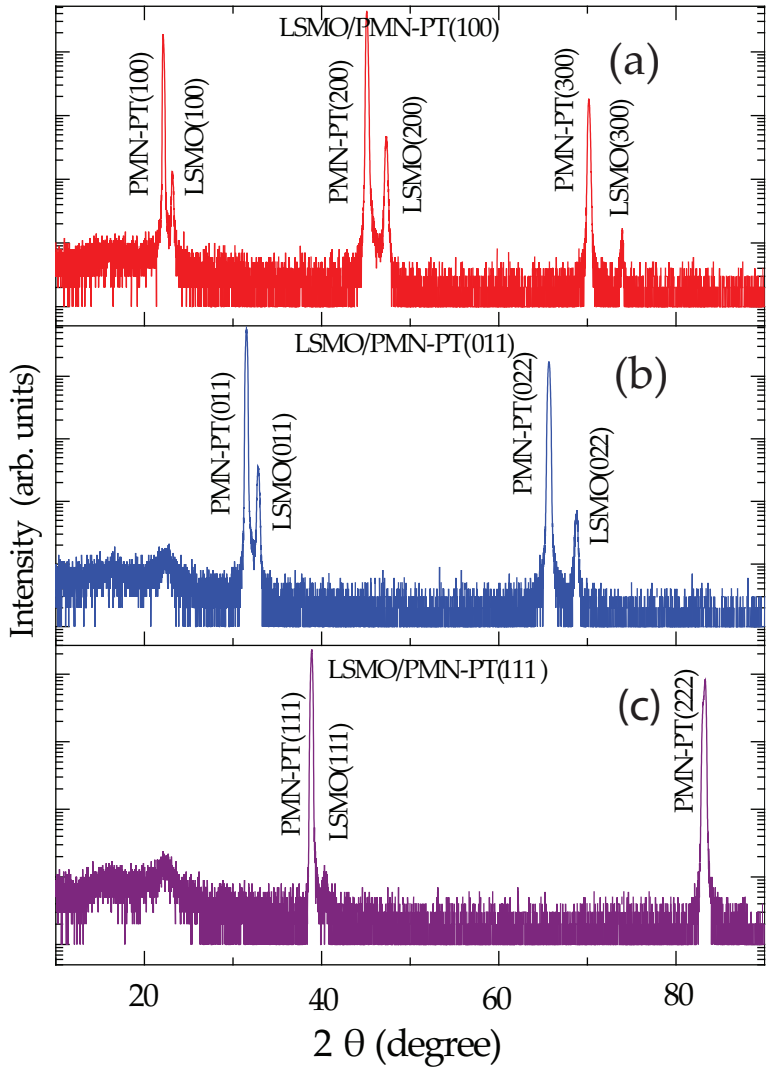

FIGURE 5.1: XRD (θ-2θ) patterns for LSMO films deposited on PMN-PT substrates oriented along [001], [011] and [111] directions.

causes the material to link smoothly with the substrate in order to avoid the creation of "dangling bonds", causing the film to create an IP tensile strain [4]. The LSMO/PMN-PT heterostructure produced epitaxial strain is fit-in by a minute IP rotation of the LSMO lattice [6]. As a result, substrate-induced strain causes a change in the LSMO unit cell's lattice parameter without affecting its structure. The magnetic structure of the LSMO film is controlled, which alters the easy axis of M [7]. As a result, a link between structure and static magnetic characteristics has been addressed in relation to the growth condition of LSMO on PMN-PT. Despite the fact that the lattice strain effect in FM thin films induced by substrate has been widely investigated, a proper exploration of the impact is still required, both in terms of basic and practical factors. For device manufacture, it would be especially beneficial to develop quantitative correlations between the characteristics of thin films and associated lattice strain effects.

5.3.2 Magnetic Properties

The magnetic response of LSMO/PMN-PT heterostructures were carried out by using a VSM. Figure 5.2 depicts the plot of M as a function of temperature. From the plot, it can be observed that at RT, the LSMO film exhibits strong IP FM behavior. The M-T graph is obtained while heating, followed by zero-field cooling below the RT. The M-T data was measured by applying an IP H-field of 100 Oe. The M-T has a "Brillouin-like" curve that indicates a reduction in M as temperature rises. The film exhibits a magnetically soft behavior with M_S very close to that of the stoichiometric bulk LSMO. The M-T measurements were used to test the LSMO film's magnetic resilience. From M-T curves, dM/dT has been plotted as a function of temperature and has been shown in Fig. 5.2 (inset). The plot shows that the T_C remains the same for all the samples, indicating their RT FM behavior.

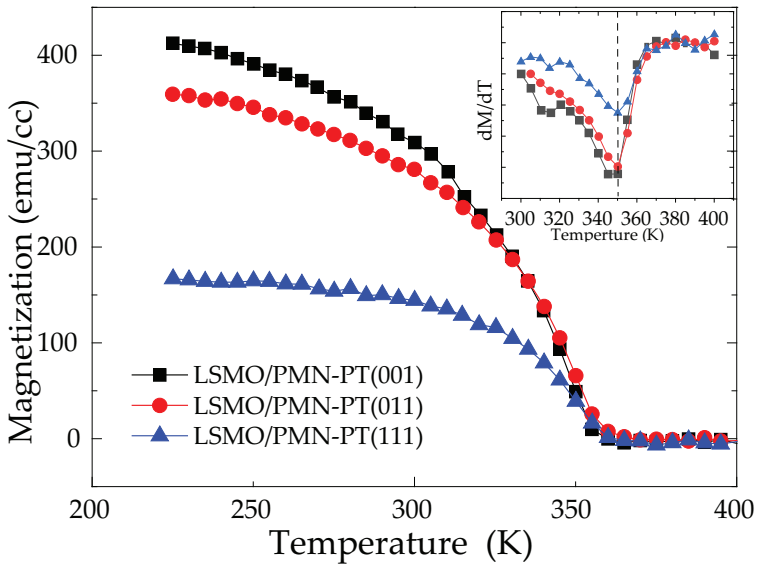

FIGURE 5.2: The *M-T* data of LSMO deposited on PMN-PT(001) (represented by black squares), PMN-PT(011) (represented by red dots), PMN-PT(111) (represented by blue triangles) and (inset) shows the corresponding dM/dT versus T plots.

5.3.2.1 LSMO/PMN-PT(001)

Figure 5.3 demonstrates the *M-H* loops for LSMO deposited on PMN-PT(001). The sample has been rotated in-plane parallel to the applied H-field, with an angular difference of 15° while measuring the individual loops in the in-plane applied H-field.

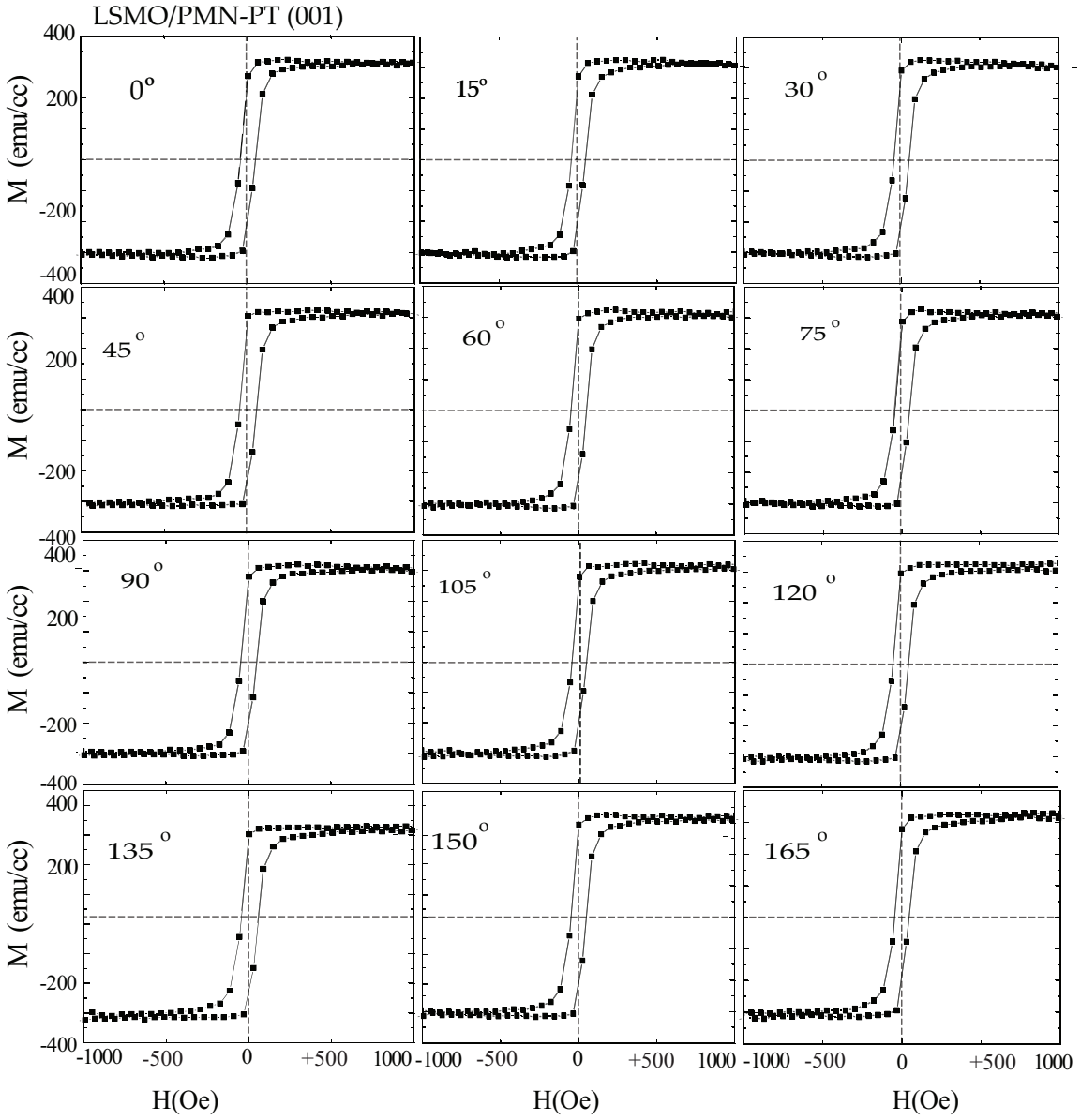

FIGURE 5.3: In-plane *M-H* loops measured in different orientations of the LSMO sample deposited on PMN-PT(001).

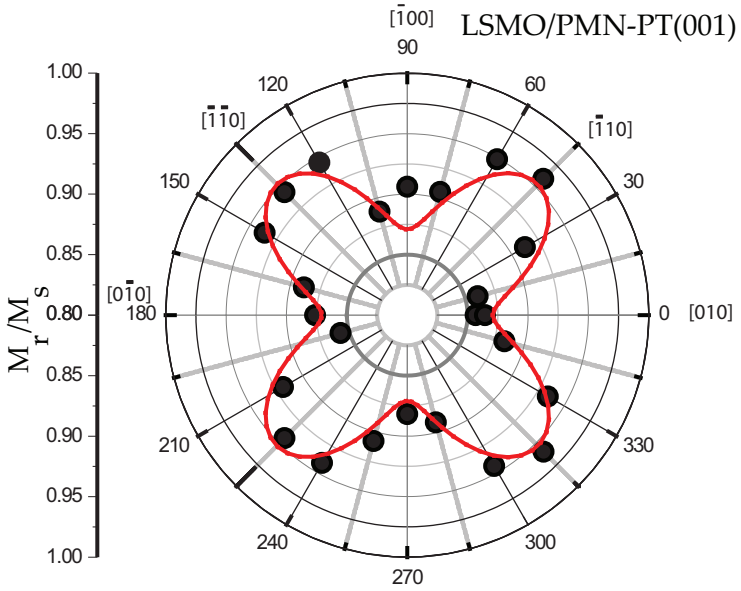

FIGURE 5.4: Polar plot of M_r/M_S versus rotation angle of LSMO/PMN-PT(001) heterostructure.

The data shows that the film having an orientation towards [001] has an in-plane M_S of 320 emu/cc. The H_c of the sample is 50 Oe. This shows that the sample is soft FM in nature. The ratio of M_r and M_S obtained after diamagnetic correction and plotted as a function of the "azimuthal angle", θ. A clear difference has been observed, revealing the presence of IP anisotropy of the LSMO film. Figure 5.4 shows the M_r/M_S versus θ plot in polar form. The resulting graph shows an in-plane biaxial anisotropy for LSMO deposited on PMN-PT(001). The obtained graph has been fitted using the mathematical equation: $|\sin\theta|$ for LSMO deposited on PMN-PT(001)(shown in a solid red curve).

The reason behind the 4-fold anisotropic behavior of LSMO/PMN-PT(001) can be attributed to the fact that PMN-PT(001) has 8 intrinsic polarization directions along [$\bar{1}$10], [$\bar{1}\bar{1}$0], [1$\bar{1}$0] and [110], which corresponds to 4 structural domains. The projections of the polarization directions give the resultant polarization directions. The resultant polarization directions of the PMN-PT drive the M vector of LSMO towards these directions. The mechanism has been shown schematically in Fig. 5.5. In Fig. 5.5(a), the unit cell of PMN-PT(001) with polarization directions along [001] is shown. The top view of the (001) plane with projections of polarization directions is depicted in Fig. 5.5(b) and (c), which depicts the 90° orientation of the polarization direction with each other. Fig. 5.5(d) shows the orientation of LSMO along the [001] direction of the PMN-PT.

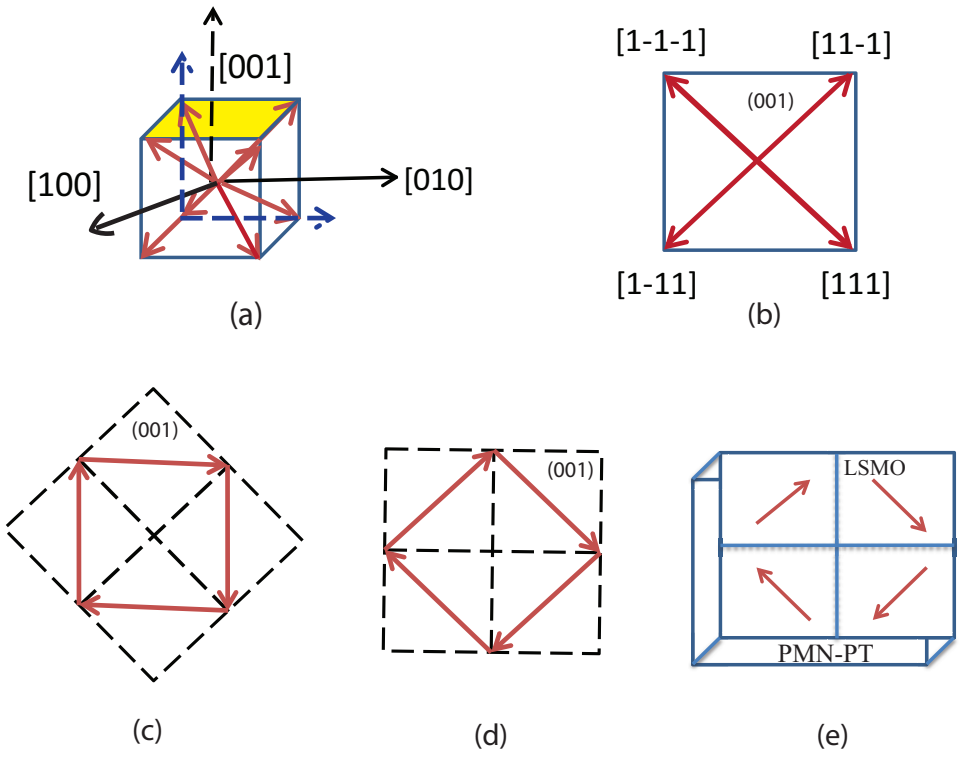

FIGURE 5.5: (a) Unit cell of cubic PMN-PT(001), (b) represents the 2-D view of the polarization directions of PMN-PT(001) plane, (c) the solid lines represents the magnetization direction of LSMO and (d) the projections of magnetic orientations of LSMO with respect to the polarization directions of the PMN-PT and (e) The projected directions of LSMO on PMN-PT.

5.3.2.2 LSMO/PMN-PT(011)

Figure 5.6 shows the *M-H* loops for LSMO/PMN-PT(011). The sample was rotated in-plane parallel to the applied H-field, with a difference of 15° while measuring the individual *M-H* loops in an applied H-field.

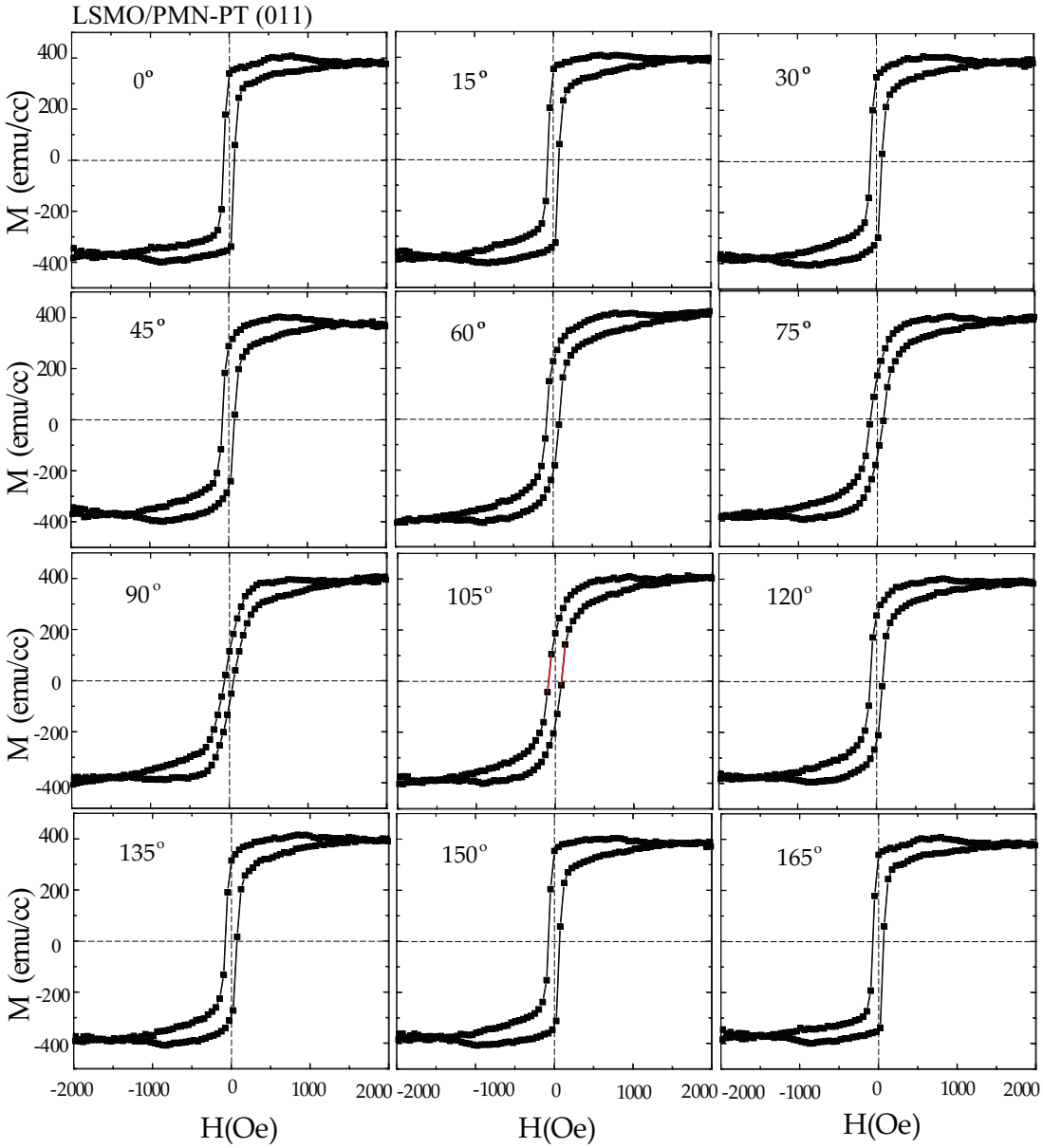

FIGURE 5.6: In-plane *M-H* loops measured for different in-plane orientations with respect to applied field of the LSMO sample deposited on PMN-PT(011).

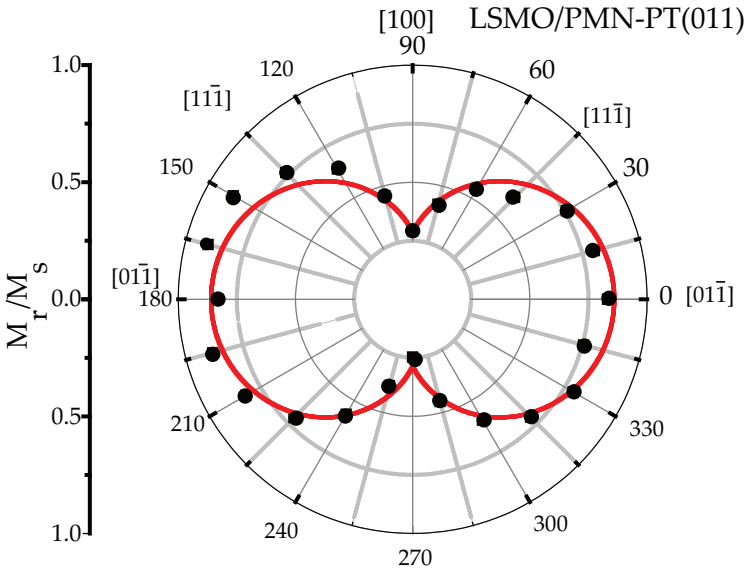

FIGURE 5.7: Polar plot of M_r/M_S versus rotation angle of LSMO/PMN-PT(011) heterostructures.

For LSMO having orientation [011], the in-plane M_S shows 400 emu/cc. The H_c of the sample is 70 Oe. The ratio of M_r and M_S obtained after diamagnetic correction was plotted as a function of the azimuthal angle, θ. A clear difference has been observed due to the in-plane anisotropy in the sample. Figure 5.7 shows the (M_r/M_S) plot in polar form. The resulting graph shows an in-plane uniaxial anisotropy for LSMO deposited on PMN-PT(011). The obtained graph has been fitted using the mathematical equations: $|\cos\theta|$ for LSMO deposited on PMN-PT(011) (shown in a solid red curve).

The reason for the observed uniaxial anisotropy of LSMO grown on PMN-PT has been explained by the illustrations presented in Fig. 5.8. This figure shows the unit cell of cubic PMN-PT with the polarization directions along [011]. The polarization directions have been displayed in Fig. 5.8 (b). Figure 5.8(c) depicts the resultant polarization direction of PMN-PT. A uniaxial LSMO growing along [100] and [01$\bar{1}$] influenced by the consequent polarization direction of PMN-PT is illustrated in Fig. 5.8 (d).

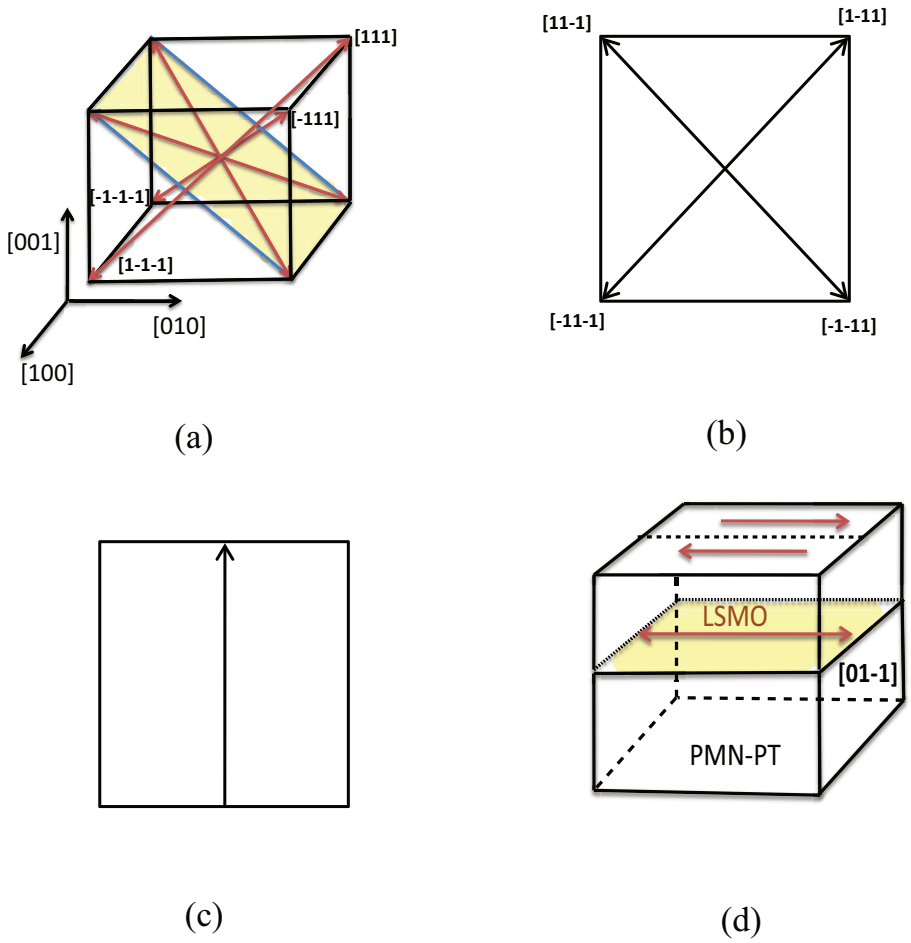

FIGURE 5.8: (a) Unit cell of cubic PMN-PT(011), (b) solid lines represent the polarization directions, (c) the resultant polarization direction and (d) the orientation of LSMO with respect to PMN-PT.

5.3.2.3 LSMO/PMN-PT(111)

Figure 5.9 shows the *M-H* loops for LSMO/PMN-PT(111) sample. The sample was rotated in-plane parallel with the applied H-field, with a difference of 15°. The individual *M-H* loops were measured in an in-plane applied H-field.

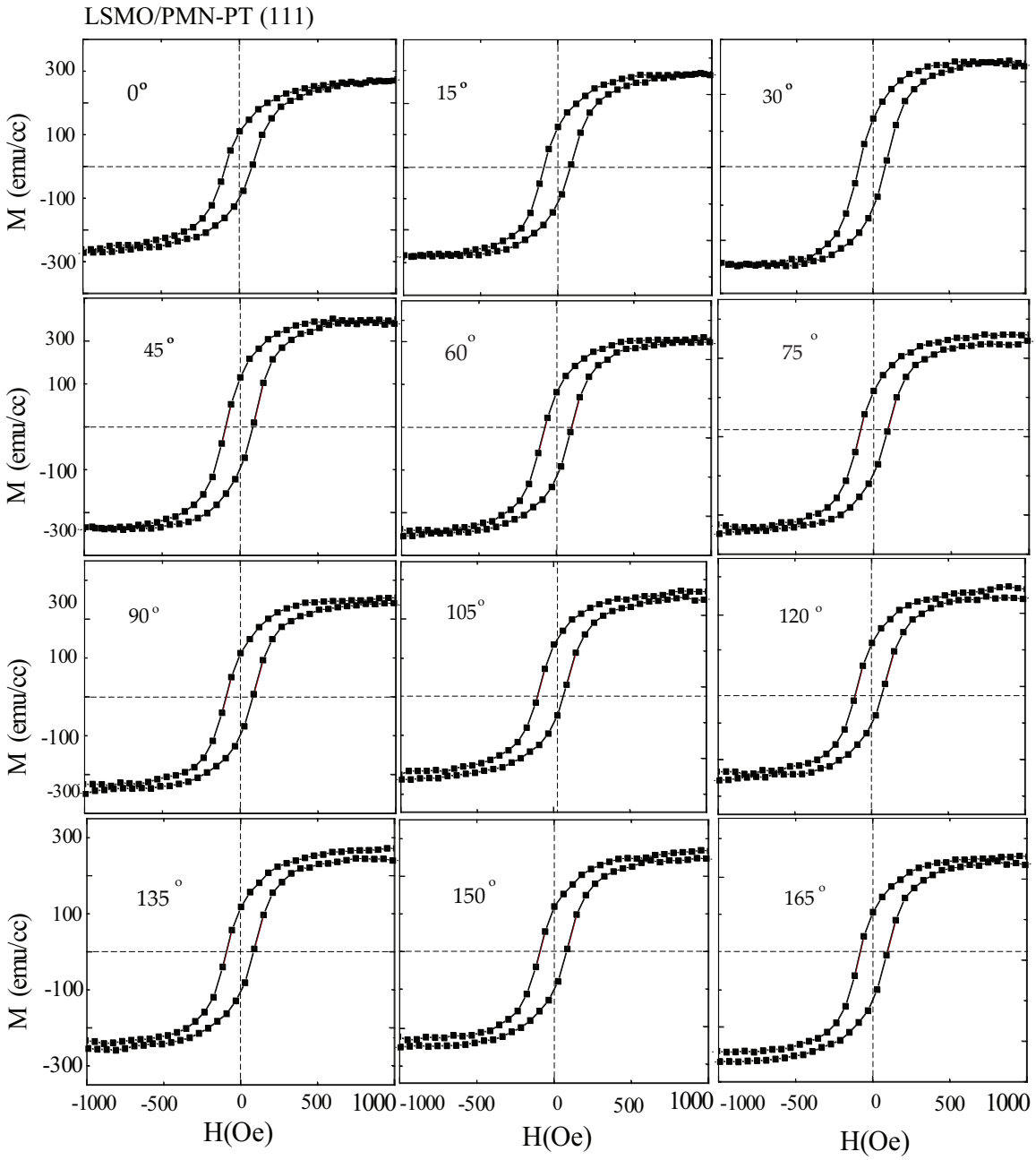

FIGURE 5.9: In-plane *M-H* loops of the LSMO sample deposited on PMN-PT(111) in different orientations.

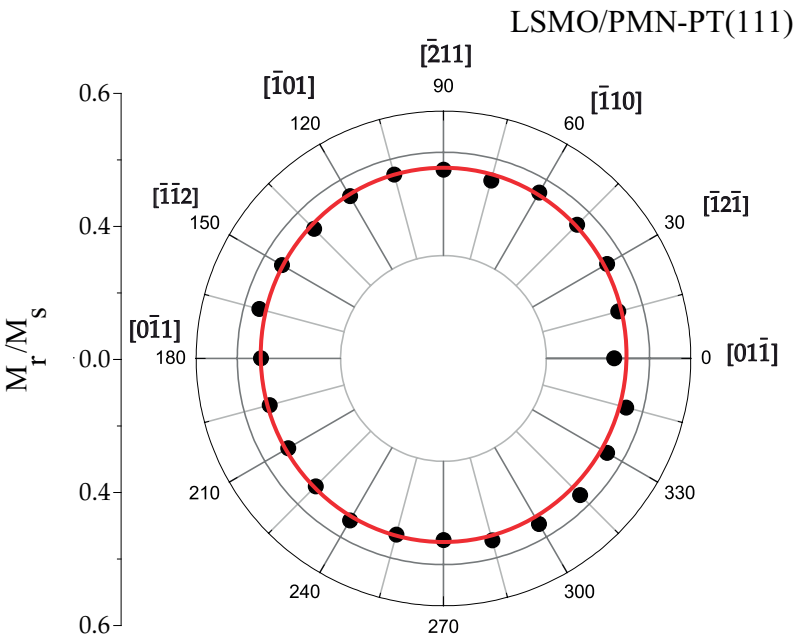

FIGURE 5.10: Polar plot of M_r/M_S versus rotation angle for LSMO/PMN-PT(111) heterostructure.

For LSMO having orientation [111], the M_S shows 270 emu/cc of M_S. The H_c of the sample is 80 Oe. The ratio of M_r and M_S obtained after diamagnetic correction was obtained as a function of the "azimuthal angle", θ. The plotted graph indicates that the LSMO/PMN-PT(111) is magnetically isotropic. Figure 5.10 shows the M_r/M_S versus θ plot in polar form. The obtained graph has been fitted using the mathematical equation: $\sin^2\theta + \cos^2\theta$ (shown in a solid red curve).

The polarization of PMN-PT along [111] shows 3-fold symmetry. The XRD measurement suggests that the (111) plane of LSMO has grown epitaxially on PMN-PT(111) plane. The in-plane magnetic measurements suggest that LSMO deposited on PMN-PT orients its spin along the direction of polarization of PMN-PT. An illustration of the IP lattice arrangements of the pseudocubic LSMO unit cell on the cubic PMN-PT substrate is shown in figure 5.11. Figure 5.11(a) shows the cubic unit cell of PMN-PT along with the (111) plane. Figure 5.11(b) shows the resultant polarization on the (111) plane. Figure 5.11(c) shows the 2-D view of the PMN-PT(111) surface along with the polarization direction [8]. Figure 5.11(d) shows the magnetization direction of LSMO. Figure 5.11(e) depicts the orientation of M direction of LSMO along PMN-PT(111).

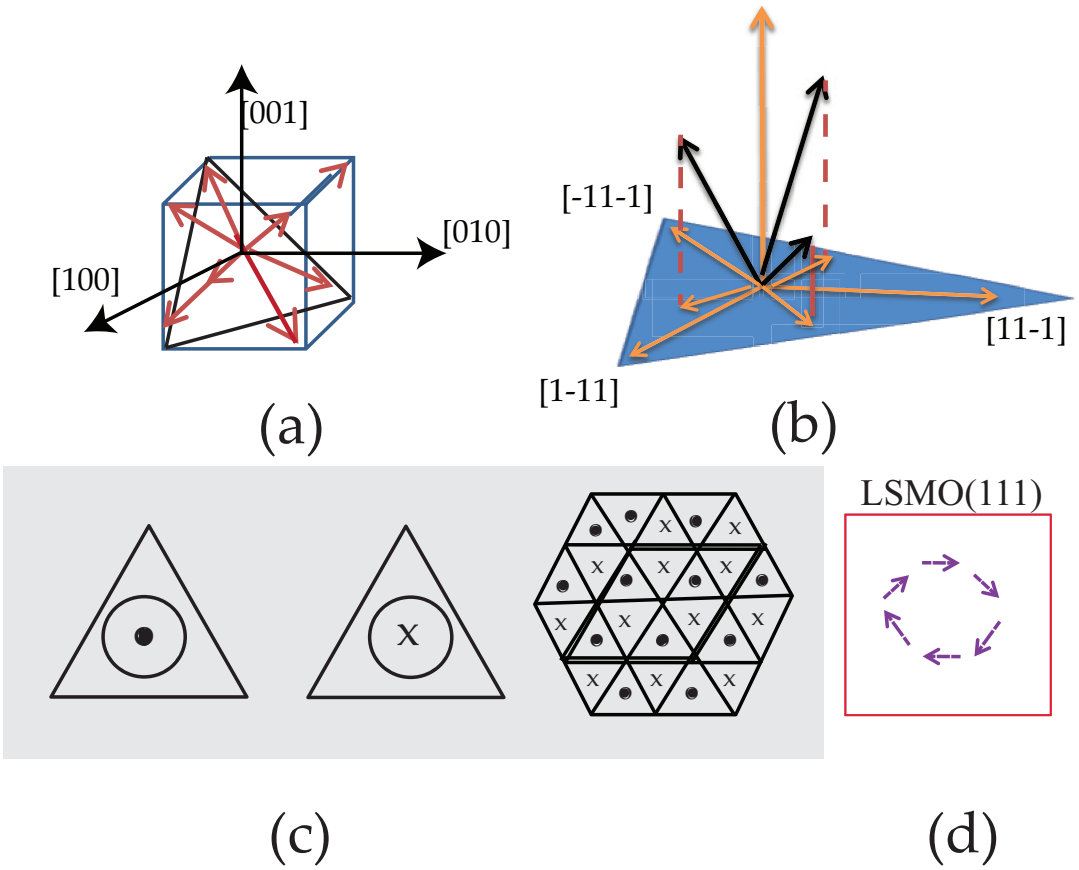

FIGURE 5.11: (a) Unit cell of cubic PMN-PT(111), (b) projections of the polarization directions, (c) resultant of the projected polarization on (111) plane of PMN-PT and (d) magnetization directions of LSMO.

5.4 Summary

In summary, epitaxial oriented films of LSMO have been formed on PMN-PT with orientations of [001], [011] and [111], respectively. The films are FM at RT, and the T_C is about 350 K. At RT, in-plane *M*-*H* measurements indicate that the films formed on PMN-PT (001), (011) and (111) have magnetic 4-fold and 2-fold axis and isotropic symmetry, respectively. The LSMO sample deposited on PMN-PT(111) is magnetically isotropic in nature. These findings suggest that the symmetry observed for the film strain, and hence the film's magnetic anisotropy, are significantly connected to the FE domain configurations of the substrate. The magnetic anisotropy at the FE-FM interface via strain-mediated ME coupling might be possible to generate magnetoelastic coupled devices.

References

[1] J. O'Donnell, M. S. Rzchowski, J. N. Eckstein and I. Bozovic, Appl. Phys. Lett. **72** 14 (1998).

[2] O. Chmaissem, B. Dabrowski, S. Kolesnik, J. Mais, J. D. Jorgensen, and S. Short, Phys. Rev. B **67** 094431 (2003).

[3] A. M. Haghiri-Gosnet and J. P. Renard, J. Phys. D: Appl. Phys. **36** R127 (2003).

[4] R. J. Zeches, M. D. Rossell, J. X. Zhang, A. J. Hatt, Q. He, C.H. Yang, A. Kumar, C. H. Wang, A. Melville, C. Adamo, G. Sheng, Y. H. Chu, J. F. Ihlefeld, R. Erni, C. Ederer, V. Gopalan, L. Q. Chen, D. G. Schlom, N. A. Spaldin, L. W. Martin and R. Ramesh, Science **326** 977 (2009).

[5] D. Rasic and J. Narayan, Epitaxial Growth of Thin Films, Crystal Growth **127** (2019).

[6] X. Xue, Z. Zhou, G. Dong, M. Feng, Y. Zhang, S. Zhao, Z. Hu, W. Ren, Z. Ye, Y. Liu and M. Liu, ACS Nano **11** 9286 (2017).

[7] L. M. Berndt, V. Balbarin and Y. Suzuki, Appl. Phys. Lett. **77** 2903 (2000).

[8] M. Zheng, H. Ni, Y. Qi, W. Huang, J. Zeng, and J. Gao, Appl. Phys. Lett. **110** 182403 (2017).

Chapter 6

Ferromagnetic resonance studies of LSMO/PMN-PT heterostructures

6.1 Introduction

FMR originates from the coupling between an electromagnetic (EM) wave and the M of a magnetic material. A substantial amount of rf power is lost because of the coupling. The precessing M ("Larmor precession") of the material absorbs the power, resulting in a loss in the form of heat. The frequency of EM wave equals the precession frequency of M ("Larmor frequency"), the resonance condition is satisfied, and the coupling occurs. The orientation polarization of the wave must match the orientation of the M. Therefore, this can be used in FMR probing the precession of M, at GHz frequencies. The FMR technique allows researchers to investigate spontaneous M, "magnetic anisotropy", and the Landé g factor by analyzing resonance frequencies and magnetic damping by examining linewidth. Hence, it is an excellent technique for extracting magneto-dynamic properties of magnetic materials [1]. It is a standard tool for probing "spin waves" (SW) and spin dynamics. The FMR is very similar to the "electron paramagnetic resonance" (EPR) and also to "nuclear magnetic resonance" (NMR).

In order to get generation and transmission of spin motion with minimum energy, the FM medium should have low Gilbert damping value, which enables to develop a desirable SW device. Non-conducting magnetic materials may show low damping coefficient than hetero-epitaxial magnetic-metal film in which spin dissipation of conduction e processes does not occur. The thin-film "yttrium iron garnet" (YIG) magnetic insulator has exhibited significantly low damping on the scale of 10^{-4}. Apart from YIG, the Gilbert damping parameter for magnetic isolators is only restricted in investigations. This highlights the difficulties in using microwave FMR techniques to perform the research on insulating thin-film materials. The soft magnetic spinel NiZnAl-ferrite thin films have recently been described, with a low Gilbert damping value ($3x10^{-3}$) [2]. The LSMO has a damping value of 10^{-2}, which is lower than that of typical FM metals, indicating that it is a suitable material to use in magneto-dynamic devices [3]. Furthermore, Liao et al. discovered that either strain or interfacial oxygen MnO_6 interaction might tune the "magnetic" and

"electronic" anisotropies of LSMO, which in turn influences the magneto-dynamic constant. As a result, the LSMO is a good candidate for FM thin films in multiferroic heterostructure fabrication [4]. The FMR technique is frequently employed to measure the "g-factor", "magnetic anisotropy" constant, and interlayer magnetic coupling of films and substrates. Although damping constants may be obtained from line-width (H_{pp}) values which define static magnetic characteristics, are calculated from the resonance field (H_R) of FMR spectra. The "Gilbert damping constant" (α) of FM materials is crucial for achieving different magnetic switching applications [5]. The FMR has been performed to detect the influence of epitaxial strain-induced ME coupling on magneto-dynamic properties of both isotropic and anisotropic LSMO films. Also, to explore E-field-controlled FMR of LSMO thin films, the LSMO/PMN-PT heterostructures were electrically poled, and FMR measurements were undertaken.

6.2 Experimental

The FMR measurements were carried out at RT with a "vector network analyzer" in the frequency range of 1 to 20 GHz. The applied H-fields of up to 4000 Oe were employed IP along with the three different LSMO directions after placing the LSMO films on a CPW. The CPW was masked with a SiO_2 non-conducting layer to prevent electrical contact between the LSMO films and the CPW. The CPW was exposed to a 5 dBm rf power, and the S_{21} parameters were measured, from which the α value was calculated. As a background, the spectra measured at 2780 Oe was subtracted from every measured data.

The PMN-PT substrate was deposited with a 100 nm-thick Cu-layer as a bottom electrode by the thermal evaporation process to obtain good electrical contacts for electrical poling measurements. The LSMO/PMN-PT samples were electrically poled positively and negatively by applying a maximum 10 kV/cm E-field.

6.3 Results

6.3.1 LSMO/PMN-PT(001)

6.3.1.1 Lineshape measurements

The FMR measurements were carried out both on LSMO/PMN-PT(001) un-poled and poled samples in three different crystal orientations, viz., [010], [110] and [100] happen to be magnetically differently oriented directions. Figure. 6.1 shows the observed field-dependent "transmission signal" (S_{21}) lineshape curves measured at different frequencies. The data were acquired by changing the external H-field from 4000-0 Oe field values at fixed GHz frequency. It is found that the H_r enhances with the enhanced frequency, which is not uncommon for a FM thin film [6]. As it can be observed from the graph, with the increase in an applied magnetic field, the peak

shifts towards a higher value of the magnetic field, and there is an increment of FWHM. This happens for both poled and un-poled samples.

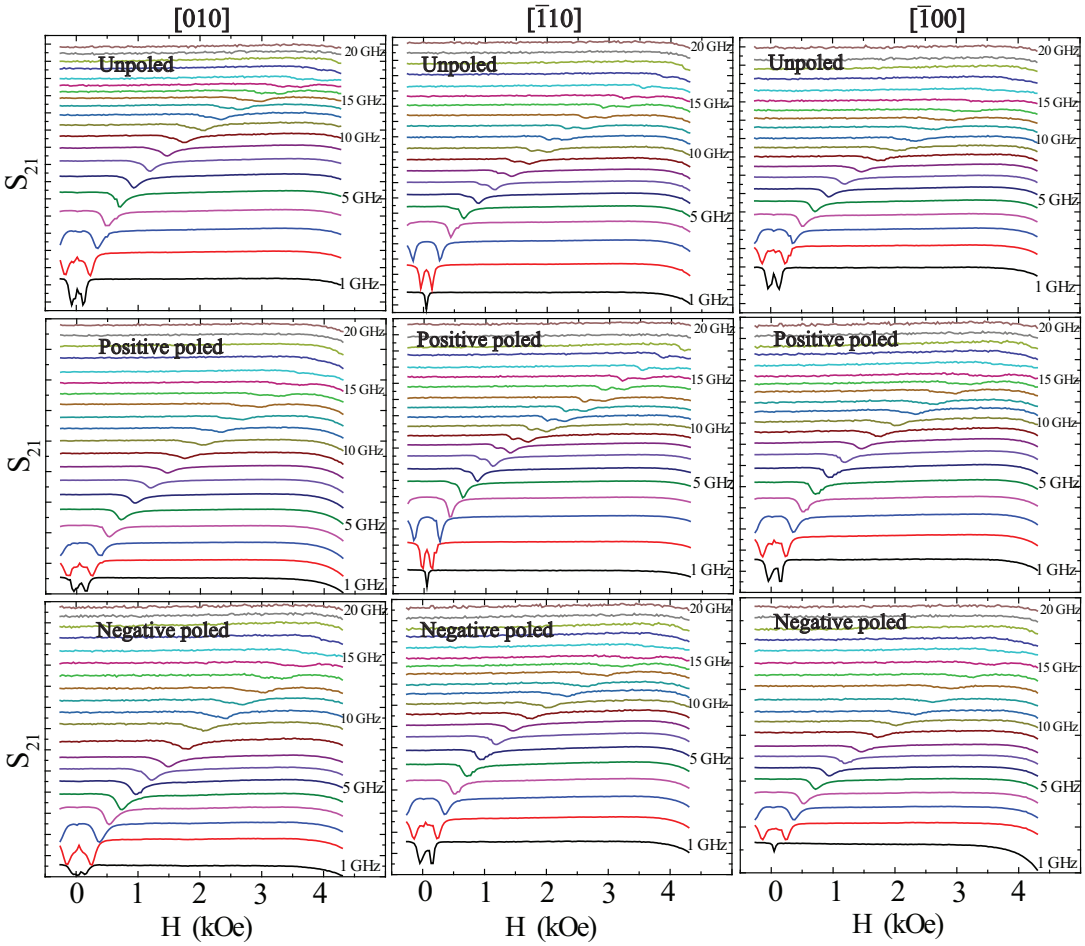

FIGURE 6.1: The lineshape plot of LSMO/PMN-PT(001) with a frequency ranging from 1-20 GHz by varying applied magnetic field from -400 to 4000 Oe in different directions.

The FMR absorption line shape is usually considered to be symmetric Lorentzian for metallic samples [7]. However, in the case of non-conductive materials, the generated microwave "eddy currents" in the film can alter the "line-shape symmetry" [3]. The relative phase between E-field and H-field components can also impact the line shape in an experimental setup comprising waveguides, coaxial cables, etc. [7, 8]. As a result, the FMR absorption to a linear mixture of symmetric and antisymmetric contributions, as defined by the parameters in equation (6.1). As it can be observed from the line-shape plots that the multiple resonance peaks arise from the LSMO/PMN-PT (001). The combination of the "absorptive" and "dispersive" components causes distortions in the FMR line shapes in general [3]. The absorptive and dispersive components shown by L and D, respectively, and were fitted by using,

$$S_{21} = L\frac{\Delta H^2}{(H_{ext} - H_r)^2 + \Delta H^2} + D\frac{\Delta H(H_{ext} - H_r)}{(H_{ext} - H_r)^2 + \Delta H^2} + C \tag{6.1}$$

where, S_{21} is comes from "Lorentzian" and "dispersive" line shape, L and D are amplitudes of the "absorptive" and "dispersive" parts, H_{ext} is the "external magnetic field", H_r is the "resonance field", ΔH is the "FWHM", and C is a "constant". While fitting, ΔH and H_{ext} has been treated as free-fitting parameter. The observed FMR absorption agrees well with the Lorentzian fit calculated using equation (6.1).

6.3.1.2 Kittel fit

Kittel equation describes the relationship between frequency and resonance field. Fig. 6.2 shows the Kittel fit for the LSMO/PMN-PT (001). The extracted H_r values from the fitting and M_S obtained from the *M-H* data was used to fit all the obtained dispersion curves using equation 6.2 mentioned below;

$$f_{FMR} = \gamma[(H_r + H_K)(H_r + H_K + 4\pi M_S)]^{(1/2)} \tag{6.2}$$

where, f_{FMR} is the FMR frequency and $\gamma = g\mu_B/h$ is the "gyromagnetic ratio". H_k is the effective anisotropic field, and $4\pi M_S$ is the "effective magnetization field". In the above equation, H_k and γ have been taken as the free fitting parameter, and M_S from $M - H$ data is used in the fitting procedure. From Fig. 6.2, it can be observed that the magnetic easy axis points towards [-110] for both the un-poled and poled sample, which matches with the polar plot shown in Fig. 5.4 in the previous chapter. The value of the effective anisotropic field comes out to be -115 Oe for the hard axis and -21 Oe for the easy axis for the LSMO/PMN-PT (001) sample.

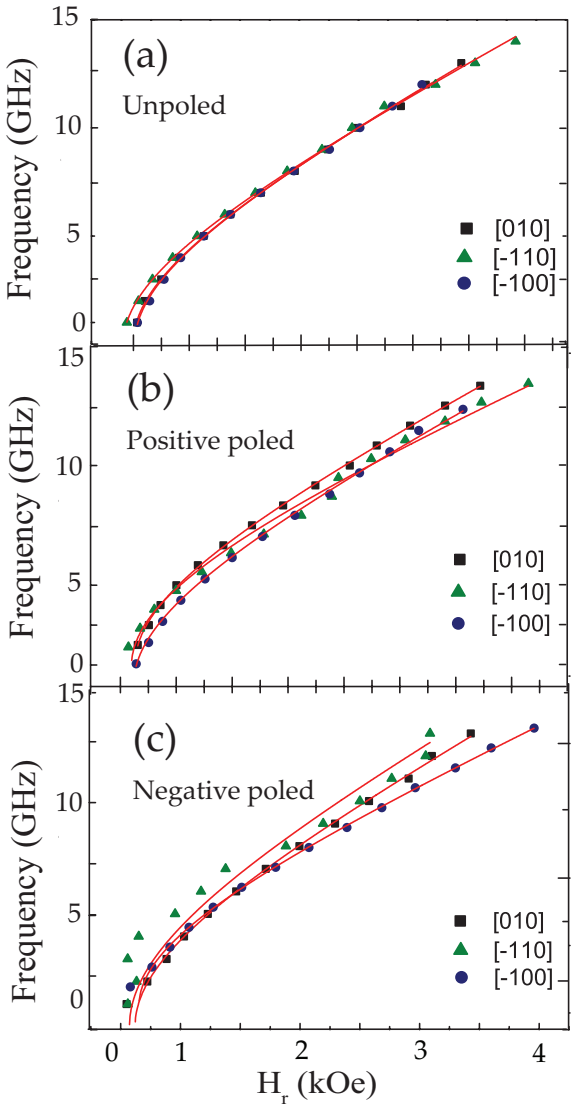

FIGURE 6.2: The plot of absorption frequency versus resonance field for (a) un-poled (b) positively poled and (c) negatively poled LSMO/PMN-PT(001) samples in different directions. The solid (red) lines show the Kittle fit.

6.3.1.3 Gilbert damping factor

The LLG equation describes M precession in the material and provides the important information about the magnetic system under investigation. This has attracted considerable attention to the scientific community over many years due to its importance in "information storage" and SW applications. In particular, the damping constant, α can be important in many controlling processes of spin dynamics phenomena [9]. The basic concept of α arises from M precession relaxation in the absence of an external agency. However, a proper knowledge of its origin is still need to be explored [10]. A combination of "spin-orbit interaction" and "*s-d* scattering" into FM band "electrons" by "phonon" is believed to be the reason for magnetic relaxation resulting to an intrinsic α of the LLG type [9,10].

This magneto-dynamic damping constant (α) is calculated from FMR linewidth. To characterize α, frequency as a function of linewidth (ΔH) for LSMO/PMN-PT (001) is plotted and shown in Fig. 6.3 for unpoled and poled sample in both magnetically easy [010] and hard [$\bar{1}$00] axis directions. The data has been fitted using the equation,

$$\Delta H(f) = \Delta H_{in-homo} + \frac{4\pi\alpha f}{\gamma} \tag{6.3}$$

where, $\Delta H_{in-homo}$ is the linear relation between "linewidth" and "frequency", which can be used to extract the damping parameter α and inhomogeneous linewidth broadening ΔH.

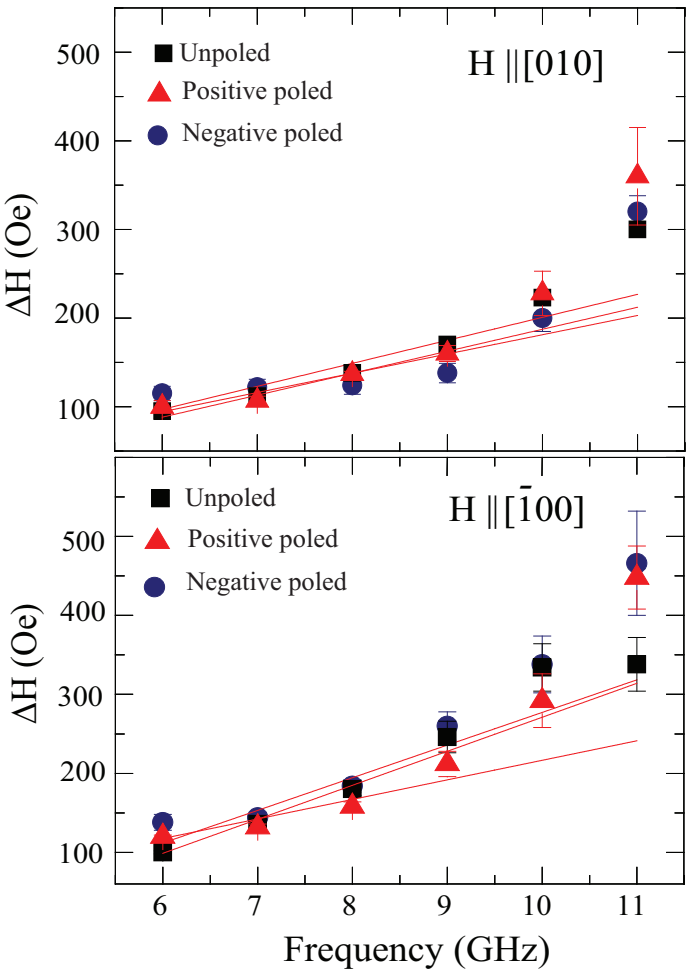

FIGURE 6.3: The linewidth versus frequency plot of unpoled and poled samples of LSMO/PMN-PT(001) applying H-field along the easy axis (a) and hard axis (b) directions, respectively

The plot shows that both the poled and unpoled samples behave linearly. Inhomogeneity of the sample LSMO/PMN-PT(001) arising because of the extrinsic contribution to the linewidth is evident from the zero-frequency intercept (ΔH_0). A significant change is observed when the sample is measured in easy and hard axis

directions showing the direction dependence of the inhomogeneity of the sample. The α has been obtained using equation 6.3 and tabulated in Table 6.1.

TABLE 6.1: The Gilbert damping constant α for LSMO/PMN-PT(001) in different directions with and without electric poling.

Sample code	Easy axis	Hard axis
Un-poled	5.60 x 10^{-2}	2.65 x 10^{-2}
Positive poled	9.77 x 10^{-2}	2.78 x 10^{-2}
Negative poled	6.71 x 10^{-2}	2.35 x 10^{-2}

The table shows that the α varies with the change in magnetic orientation. The damping is less along the hard axis direction than in the easy axis direction, meaning that the SW excited and measured corresponding to the easy-axis direction will get damped faster than on the hard axis.

It can also be noticed that when the sample is electrically poled, the damping constant value changes. There is an increment in damping when the sample is poled as compared to the un-poled sample. With the application of an electric field, the polarization results in the strain. The piezoelectric coefficient of PMN-PT(001) is d_{33} = 1281 pC/N for the PMN-PT(001) substrate, the LSMO film between the two electrodes suffers a "tensile strain" in x-direction and a "compressive strain" in y-direction in an applied electric field, E = 10 kV/cm and suffers opposite strains at E = -10 kV/cm [11].

6.3.2 LSMO/PMN-PT(011)

6.3.2.1 Lineshape measurements

The FMR measurements were carried out both on LSMO/PMN-PT(011) un-poled and poled samples in three different magnetic orientations viz., [100], [$1\bar{1}1$], and [$01\bar{1}$]. Figure 6.4 shows the observed field-dependent S_{21} lineshape curves measured at different frequencies. The observations are similar to that of LSMO/PMN-PT(001) sample.

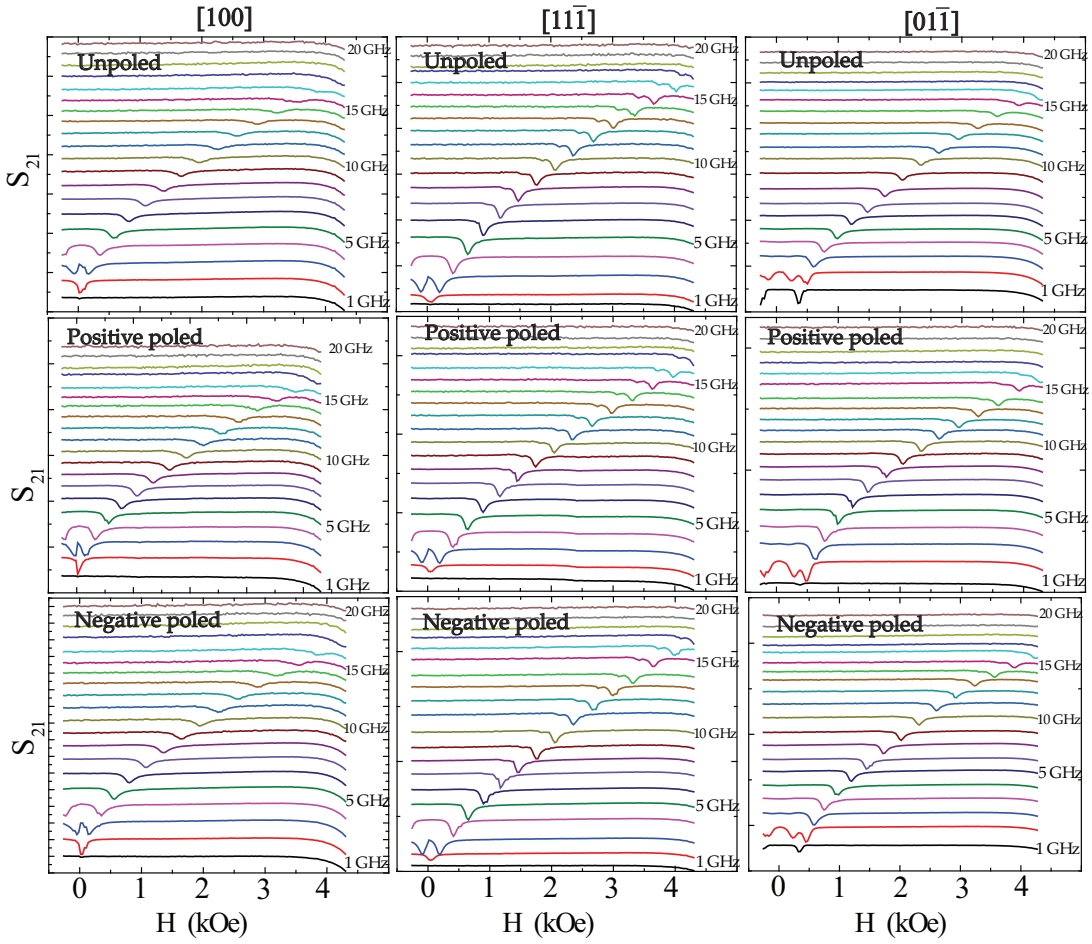

FIGURE 6.4: The lineshape plot of LSMO/PMN-PT(011) with a frequency ranging from 1-20 GHz by varying applied magnetic field from -400 to 4000 Oe in different directions.

The lineshape curves were fitted using equation 6.1. The observed FMR absorption agrees well with the Lorentzian fit calculated using equation 6.1.

6.3.2.2 Kittel fit

The extracted H_r values from the fitting and M_S obtained from the $M-H$ data were used to fit all the obtained dispersion curves using equation 6.2 mentioned above. Figure 6.5 shows the plot for LSMO/PMN-PT(011). The dependence of H_r on applied "microwave frequency" can be analyzed by Kittel's formula for the films.

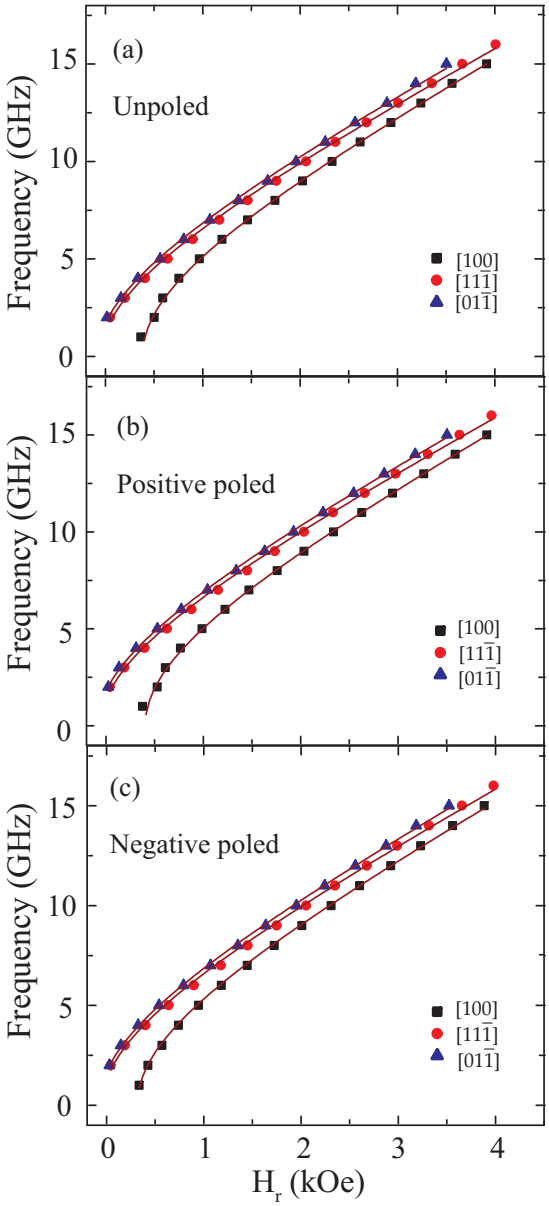

FIGURE 6.5: The plot of absorption frequency versus resonance field for (a) un-poled sample (b) positive poled and (c) negative poled LSMO/PMN-PT(011) in different directions. The solid lines shows the Kittle fit.

From Fig. 6.5 it can be observed that for both the un-poled and poled sample, the magnetic easy axis points towards [01$\bar{1}$], which matches with the polar plot shown in Fig. 5.6 in the earlier chapter. The value of the effective anisotropic field comes out to be -380 Oe for the hard axis and 80 Oe for the easy axis for LSMO/PMN-PT(011).

6.3.2.3 Gilbert damping factor

Magneto-dynamic damping is also a significant parameter as calculated from FMR linewidth. To characterize the α, frequency as a function of linewidth (ΔH) for LSMO (011) is plotted as shown in Fig. (6.6) for unpoled and poled sample in both easy

and hard magnetic axis direction. The zero-frequency intercept (ΔH_0) shows the presence of the inhomogeneity of the sample. The data has been fitted using the equation (6.3) mentioned earlier.

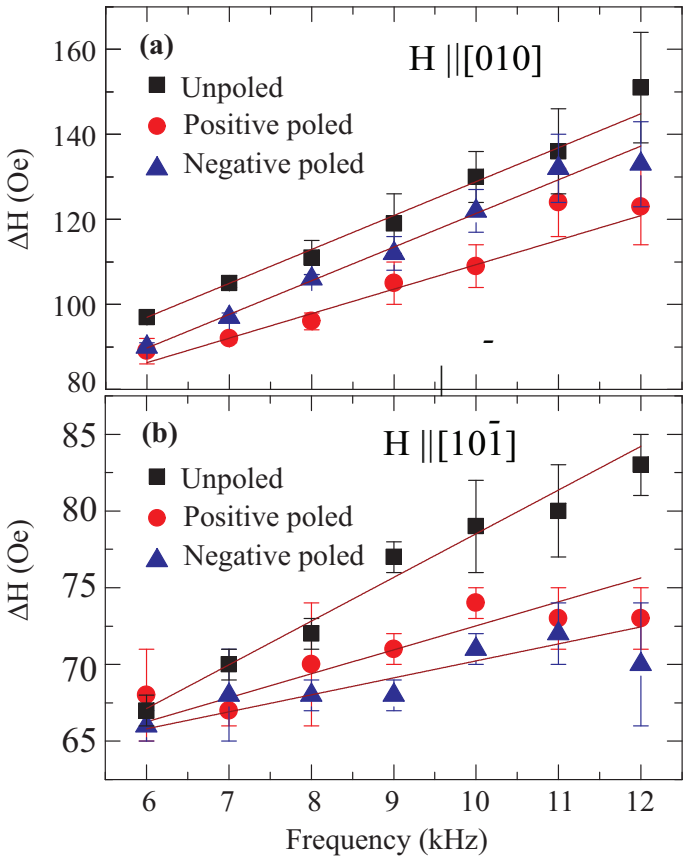

FIGURE 6.6: The linewidth versus frequency plot of unpoled and poled samples of LSMO/PMN-PT(011) applying H-field along the easy axis (a) and hard axis (b) directions, respectively.

TABLE 6.2: The Gilbert damping constant α for LSMO/PMN-PT(011) in different directions with and without electric poling.

Sample code	Easy axis	Hard axis
Un-poled	11.08 x 10^{-3}	4.3 x 10^{-3}
Positive poled	8.83 x 10^{-3}	1.79 x 10^{-3}
Negative poled	11.78 x 10^{-3}	1.33 x 10^{-3}

From the tabulated values, it is clear that the damping constant varies with the change in magnetic orientation. The damping is less along the hard axis direction than in the easy axis direction, showing the SW getting damped faster along the "hard axis direction" than in the "easy axis direction". It can also be observed that when the sample is electrically poled, the damping constant value changes. There is an increment in damping along the hard axis when the sample is un-poled compared to the poled sample.

With the application of E-field for LSMO/PMN-PT(001), along z-axis, the direction of polarization, $[\bar{1}10]$, $[\bar{1}\bar{1}0]$, $[1\bar{1}0]$ and [110] squeezes towards the z-axis. With the application of positive E-field on the piezoelectric PMN-PT(011), the projection of polarization [100] and $[01\bar{1}]$ rotates towards the z-direction. This induces a contraction along x-axis and an extension along y-axis. Similarly when negative field is applied, at-first the polarization direction rotates towards in-plane and with the further increase of field moves towards $[1\bar{1}\bar{1}]$ and $[\bar{1}\bar{1}\bar{1}]$. Consequently, the strain response behaves similar to the z-axis poling [12]. Similar to an un-poled sample, the Kittel formula was used to fit the extracted data from the dispersion curves. To calculate the value of α, equation (6.3) was used to fit the obtained ΔH values. It can be seen that there is quite a massive difference between the poled and un-poled sample, although positive and negative poling does not bring that much change in the value of α as the amount of strain generated remains almost the same. The slope of the linear plot measures the value of the damping constant α.

6.3.3 LSMO/PMN-PT(111)

6.3.3.1 Lineshape measurements

Figure 6.7 shows the field-dependent S_{21} signal of the LSMO sample obtained at different frequencies. As observed from the lineshape plots, very feeble resonance peaks arise for LSMO/PMN-PT(111).

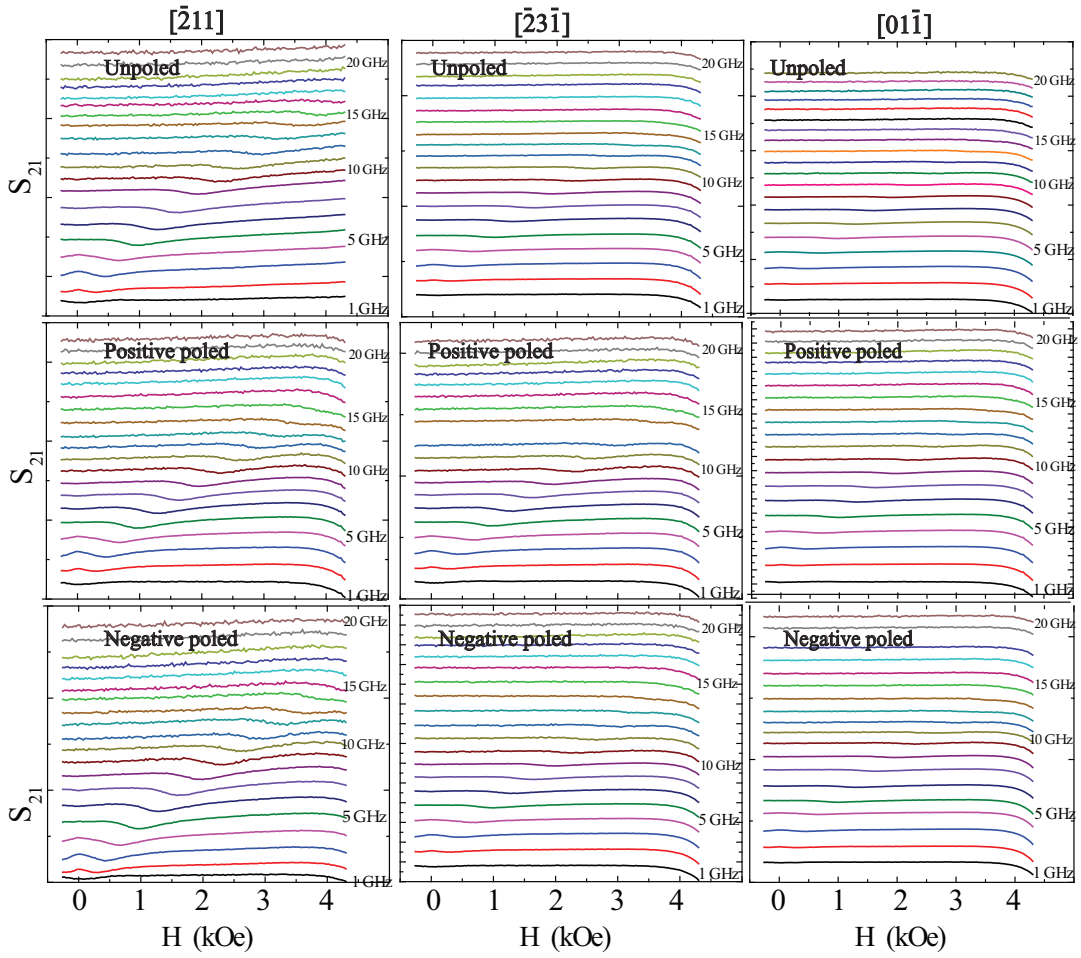

FIGURE 6.7: The lineshape plot of LSMO/PMN-PT(111) with a frequency ranging from 1-20 GHz by varying applied magnetic field from -400 to 4000 Oe in different directions.

6.3.3.2 Kittel fit

The extracted H_r values from the fitting and M_S obtained from the *M-H* data were used to fit all the obtained dispersion curves using equation (6.2) mentioned above. The value of effective magnetic anisotropy for LSMO/PMN-PT(111) comes out to be -170 Oe along [01$\bar{1}$] and -160 Oe along [$\bar{2}$11] amount showing the magnetic isotropy of the sample.

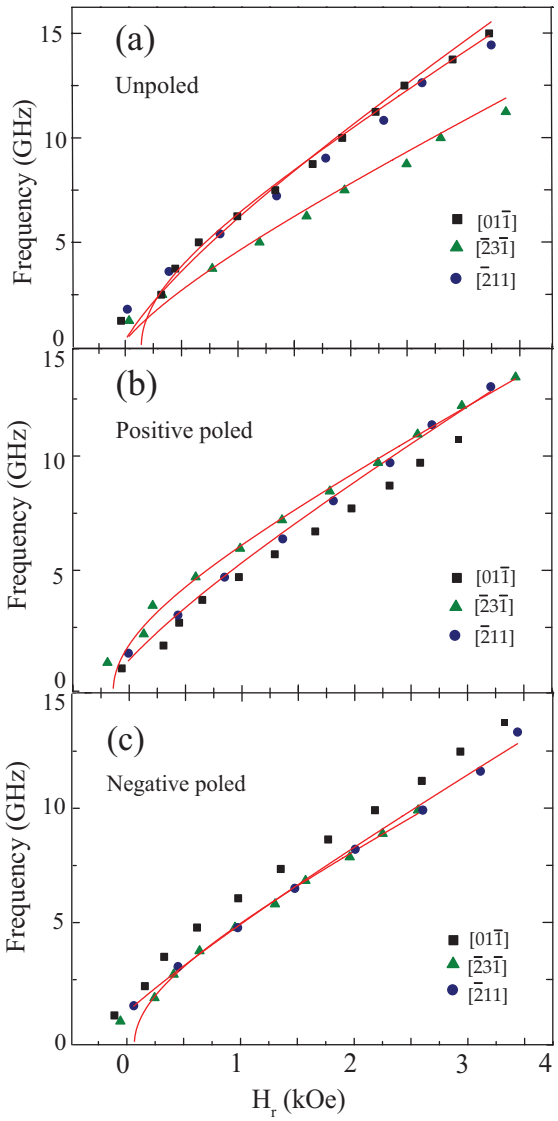

FIGURE 6.8: The plot of absorption frequency versus resonance field for (a) un-poled sample (b) positive poled and (c) negative poled LSMO/PMN-PT(111) in different directions. The solid lines shows the Kittle fit.

6.3.3.3 Gilbert damping factor

Magneto-dynamic damping is also one of the significant parameters as calculated from FMR linewidth. To characterize the magneto-dynamic constant (α), frequency as a function of linewidth (ΔH) for LSMO/PMN-PT(111) is plotted as shown in Fig. 6.9 for unpoled and poled sample in three directions. The data has been fitted using equation 6.3 mentioned earlier.

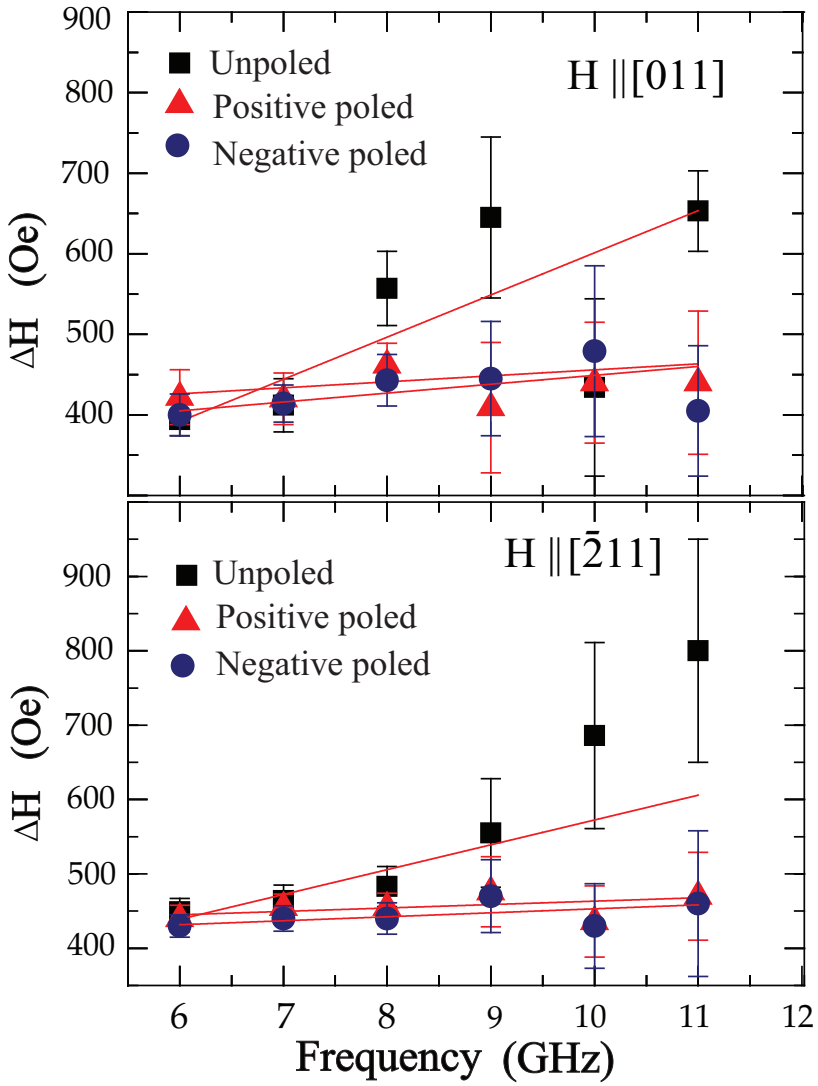

FIGURE 6.9: The linewidth versus frequency plot of unpoled and poled samples of LSMO/PMN-PT(111) applying H-field along the easy axis (a) and hard axis (b) directions, respectively.

TABLE 6.3: The Gilbert damping constant α for LSMO/PMN-PT(111) in different directions with and without electric poling.

Sample code	Easy axis	Hard axis
Un-poled	2.74 x 10^{-2}	2.63 x 10^{-2}
Positive poled	1.80 x 10^{-2}	1.72 x 10^{-2}
Negative poled	1.58 x 10^{-2}	1.56 x 10^{-2}

From the Table 6.3 it can be observed that the variation in damping is very negligible in case of LSMO/PMN-PT(111). This shows that the damping of the excited spin-wave will remain be directional independent. Even after poling the damping constant does not change much.

For LSMO/PMN-PT(111), piezoelectric coefficient, d_{33} = 81 pC/N for the PMN-PT(111) substrate is so small that the E-field has almost no influence on the substrate [11].

6.4 Summary

In summary, coplanar waveguide-based FMR measurements were carried out on the epitaxial and magnetically oriented samples. From the Lorentzian lineshape fittings, resonance field and linewidth were obtained. The dispersion curves were obtained and fitted using the Kittle equation, proving to agree with the obtained data. The "Gilbert damping constant" obtained from the linewidth fitting shows directional dependence both in the case of poled and unpoled samples. The easy axis of M for the LSMO grown on PMN-PT (001) and (011) has a larger damping constant value as compared to the hard axis. The change in the Gilbert damping factor because of the E-field poling shows the presence of ME coupling in the LSMO/PMN-PT heterostructures.

References

[1] S. J. Callori, T. Saerbeck, D. L. Cortie and K. W. Lin, Solid State Phys. **71** 73-116 (2020).

[2] B. Madon, H. B. Kang, M. G. Kang, D. Maurya, B. A. Magill, M. J. P. Alves, J.E. Wegrowe, H. J. Drouhin, S. Priya and G. A. Khodaparast, AIP Adv. **8** 105034 (2018).

[3] V. Flovik, F. Macià, S. Lendínez , J. M. Hernàndez , I. Hallsteinsen, T. Tybell and E. Wahlström, J. Magn. Magn. Mater. **420** 280 (2016).

[4] W. Zhao, D. Zhang, D. Meng, W. Huang, L. Feng, C. Hou, Y. Lu, Y. Yin and X. Li, Appl. Phys. Lett. **109** 263502 (2016).

[5] M. Oogane, T. Wakitani, S. Yakata, R. Yilgin, Y. Aando, A. Sakuma and T. Miyazaki, Jpn. J. Appl. Phys. **45** 3889 (2006).

[6] R. Qiu, Z. Wang and Z. Zhang, J. Magn. Magn. Mater. **331** 92 (2013).

[7] M. Harder, Z. X. Cao, Y. S. Gui, X. L. Fan and H. Cm, Phys. Rev. B **84** 054423 (2011).

[8] A. Wirthmann, X. Fan, Y. S. Gui, K. Martens, G. Williams, J. Dietrich, G. E. Bridges and C. M. Hu, Phys. Rev. Lett. **105** 017202 (2010).

[9] A. Hirohata, K. Yamada, Y. Nakatani, I. Prejbeanu, B. Diény, P. Pirro and B. Hillebrands, J. Magn. Magn. Mater. **509** 166711 (2020).

[10] A. Barman, S. Mondal, S. Sahoo and A. De, J. Appl. Phys. **128** 170901 (2020).

[11] Q. Guo, X. Xu, F. Wang, Y. Lu, J. Chen, Y. Wu, K. Meng, Y. Wu, J. Miao and Y. Jiang, Nanotechnology **29** 224003 (2018).

[12] T. Wu, P. Zhao, M. Bao, A. Bur, J. L. Hockel, K. Wong, P. M. Kotekar, C. S. Lynch and G. P. Carman, J. Appl. Phys. **109** 124101 (2011).

Chapter 7

Summary and conclusion

7.1 Summary and conclusions

Magnetic anisotropy and magneto-dynamic damping are the two main important parameters of magnetic materials, which play a vital role in developing device applications [1]. The concept of energy saving in devices without Joule heat dissipation in miniaturized devices is not only feasible by modulating magnetism locally using E-field and lattice-strain, but also challenging job to execute for devices at ultra-low power consumption [2]. The control of magnetic anisotropy by manipulating the nanoparticles' shapes and sizes and selecting suitable hetero-interfaces is also an important aspect and demands systematic research. In view of that, the present research work was carried out by choosing CFO and LSMO as magnetic materials and PMN-PT as ferroelectric material in the form of heterostructures.

The nanoparticles of both CFO and LSMO were synthesized by the sol-gel method. These material systems were studied systematically by varying particle sizes from nano to bulk. In order to realize strain-mediated manipulation in magnetic and magneto-dynamic properties, the thin films of CFO and LSMO were deposited by using the PLD technique, and some of them are explored in the form of heterostructures. The major outcomes from the present research have been compiled in the thesis and described chapter wise below:

The *first chapter* presents an overview of the research work undertaken. It includes a brief introduction to magnetic interactions, static, and dynamic properties of *M*, followed by the aims and objectives of the thesis to be fulfilled by choosing CFO and LSMO as suitable materials. Finally, the organization of the thesis was clearly mentioned at the end of the chapter.

The *second chapter* deals with the synthesis of bulk, nanoparticles, and thin films of CFO and LSMO materials. The working/operational principle behind the instruments/techniques used for characterization and physical property measurements were presented with suitable schematics diagrams/photographs. The data acquired by these instruments were discussed in subsequent chapters.

The *third chapter* consists of the preparation of the targets, CFO and LSMO. The single-phase CFO and LSMO were synthesized successfully by using the sol-gel method by varying the sintering temperature. The phase purity for the obtained

samples was confirmed through XRD data and Rietveld refinement analysis. Particularly in the case of CFO samples, significant changes in physical parameters were obtained with varying particle size. The surface morphology and microstructural studies of CFO show different shapes of particles with varying particle sizes. The surface morphology changes from spherical to pyramidal to lamellar to octahedral, then to truncated octahedral structures with sintering temperature. The 2-D TEM micrographs confirm the transformation of these structures with varying particle size. The observed shapes have been explained by considering the crystal growth energy for different facets of the structures. The magnetic behavior of the spherical particles ensures SPM behavior. Further, the variation of H_C with particle size depicts the single domain to multi-domain transformation upon the increase in particle size. Keeping the application of these materials in mind, the B-H_{max} values are also calculated. The results clearly ensures that the single domain with large H_C particles can be used for making permanent magnets, which are alternative to rare-earth-based magnets. In conclusion, this chapter establishes the strong connection between the CFO particles' size, shape, and magnetic nature.

The magnetic behavior of CFO thin films has been studied in *fourth chapter*. The CFO thin films were deposited by varying thicknesses from 115 nm to 300 nm. The structural and morphological studies of the deposited films show monophasic polycrystalline with different morphology. The growth of the films is interpreted to be Stranski-Krastinov growth in the present investigation. The MFM micrographs ensure the presence of OP M, which was confirmed by the magnetization measurements. From this chapter, it can be concluded that increased film thickness can promote the OP M, which might have originated because of the clustered or island (the Stranski-Krastinov) growth of the CFO thin films.

In *fifth chapter*, the strain-induced ME coupling was demonstrated in heterostructures of a 50 nm LSMO grown on PMN-PT single-crystal substrates with different orientations [001], [011] and [111]. The structural studies show the epitaxial growth of LSMO films on PMN-PT substrates oriented in [001], [011] and [111] directions. The IP $M - H$ loops measured in different directions show interesting anisotropic behavior. The polar plots (M_r/M_s versus angle between magnetic field and sample, θ) obtained from the M-H loops of LSMO deposited on PMN-PT(001) exhibit a four-fold anisotropy, whereas LSMO on PMN-PT(011) exhibits a two-fold anisotropy, and finally, LSMO deposited on PMN-PT(111) comes out to be isotropic in nature. From this chapter, it has been concluded that the strain generated across the interface of LSMO/PMN-PT oriented single crystal substrates establishes the strain-mediated ME coupling and interface-driven magnetic anisotropy. The possible mechanism behind this coupling was also presented in this chapter with suitable schematic representations.

In *chapter six*, FMR studies of LSMO/PMN-PT samples with different orientations were carried out, and from the obtained data, Gilbert damping factor, α was estimated. It has been observed that the value of α is high along the easy magnetic

axis direction as compared to the hard magnetic direction. Therefore, it has been concluded that the anisotropy-driven α is a potential guiding parameter for SW based applications and is useful for ultra-low power consumption devices. As PMN-PT is a piezoelectric material, the strain generated in PMN-PT can influence the magnetic nature of LSMO and, in turn, α. Therefore, E-field-dependent FMR measurements were also performed. The significant changes observed in α show the pathway to miniaturized communicating devices at gigahertz frequencies. From this chapter, it has been concluded that a microwave signal generated along the easy axis will get damped faster than the hard axis orientation. Also, the change in α value with the application of electric field further confirms the electric field-controlled FMR in LSMO. It paves the pathway to ultra-low-power magnetic devices at RT.

Finally, the thesis concludes with the seventh chapter, summary and future scope.

7.2 Future scope

In light of the present research results mentioned in the thesis, it is evident that the current research area has a lot of scope for further investigations of magnetic anisotropy and magnetoelastic coupling in oxide heterostructures. Some of them are mentioned below:

In this research, the fundamental characteristics of CFO nanoparticles were investigated. These particles may have scope from an application standpoint, particularly in targeted drug delivery biomedical applications [3]. In addition, the CFO nanoparticles have a large surface area, which allows for surface functionalization with antibodies and receptors, and their porous shape allows for good absorption in many medical applications [4]. The epitaxial growth of CFO on a single crystal substrate with low lattice mismatch will aid in studying thickness-dependent MCA behavior and their use in M switching applications without applying a H-field.

A fundamental investigation of the thickness dependence of LSMO on mainly oriented PMN-PT substrates to evaluate variations in anisotropic magnetic behavior may be undertaken. In view of the present research, there exists a ME coupling between LSMO and PMN-PT; this research may be investigated by employing various approaches to determine the level of coupling between the two materials qualitatively. Due to promising ME coupling, this pair of materials in the form of heterostructure can be explored for prototype device applications that can demonstrate functionalities at low power consumption [5]. Based on the FMR results obtained in the present thesis, there is a lot of scope for SW excitation, propagation, and detection at RT in FM oxides [6]. Additionally, SW characterizations can be carried out on the LSMO/PMN-PT samples, and their suitability can be checked for fabricating SW devices. The strategies employed for LSMO/PMN-PT system can be used for other oxide materials and their combinations. Finally, the present research opens the gateway to more developments in SW and magnonic technology. Due to the unique

features of SW spectra, the magnonic devices should be able to provide significant new functionality, which was not realized yet in photonics or electrical devices [7].

References

[1] Y. Wei, W. Zhang, L.V. Bing, X. Xushibo and Z. Ma, Science Adv. **7** 4 (2021).

[2] B. Rana and Y. C. Otani, Commun. Phys. **2** 90 (2019).

[3] K. Shahzada, S. Mushtaq, M. Rizwan, W. Khalida, M. Atifa, F. Nafees, A. R. Abbas, Z. Ali, Mater. Sci. and Eng: C **119** 111444 (2021).

[4] S. Y. Srinivasan, K. M. Paknikar, D. Bodas and V. Gajbhiye, Nanomedicine (Lond.) ISSN 1743-5889 (2018).

[5] J. M. Hu, Z. Li, L. Q. Chen and C. W. Nan, Nat. Commun. **2** 553 (2011).

[6] T. Liu, H. Chang, V. Vlaminck, Y. Sun, M. Kabatek, A. Hoffmann, L. Deng and M. Wu, J. Appl. Phys. **115** 17A501 (2014).

[7] V. V. Kruglyak, S. O. Demokritov and D. Grundler, J. Phys. D: Appl. Phys. **43** 264001 (2010).

Correlation between structural, microstructural and magnetic properties of CoFe2O4 and La0.7Sr0.3MnO3 nano, bulk and thin films for possible room-temperature device applications

by Avisek Das

Submission date: 26-May-2022 02:48PM (UTC+0530)
Submission ID: 1844510439
File name: Avisek_Das.pdf (23.32M)
Word count: 30602
Character count: 151397

Correlation between structural, microstructural and magnetic properties of CoFe2O4 and La0.7Sr0.3MnO3 nano, bulk and thin films for possible room-temperature device applications

ORIGINALITY REPORT

16%	11%	14%	2%
SIMILARITY INDEX	INTERNET SOURCES	PUBLICATIONS	STUDENT PAPERS

PRIMARY SOURCES

1	iopscience.iop.org Internet Source	7%
2	Avisek Das, Kranthi Kumar Bestha, Prakash Bongurala, Venkataiah Gorige. " Correlation between size, shape and magnetic anisotropy of CoFe O ferrite nanoparticles ", Nanotechnology, 2020 Publication	2%
3	Submitted to University of Hyderabad, Hyderabad Student Paper	1%
4	Kranthi Kumar Bestha, Joyal John Abraham, Jeyaramane Arout Chelvane, Venkataiah Gorige. " Influence of cation distribution on magnetic response of polycrystalline Co Ni Fe O (0 ≤ ≤ 1) ferrites ", Physica Scripta, 2020 Publication	<1%
5	Kranthi Kumar Bestha, Joyal John Abraham, J Arout Chelvane, Venkataiah Gorige. "	<1%

Dr. VENKATAIAH GORIGE
Assistant Professor
School of Physics, University of Hyderabad
Gachibowli, Hyderabad 500046, INDIA

Dr. VENKATAIAH GORIGE
Assistant Professor
School of Physics, University of Hyderabad
Gachibowli, Hyderabad 500046, INDIA

	Influence of cation distribution on magnetic response of polycrystalline Co Ni Fe O (0 ≤ ≤ 1) ferrites ", Physica Scripta, 2020 Publication	
6	hdl.handle.net Internet Source	<1 %
7	V. Madhav Kumar, A. Srinivas, A. Talapatra, Saket Asthana, J. Mohanty, S. V. Kamat. "Effect of deposition temperature on structural, microstructural and magnetic properties of CoFe2O4 thin films deposited by pulsed laser deposition", Journal of Materials Science: Materials in Electronics, 2016 Publication	<1 %
8	www.digikey.com.mx Internet Source	<1 %
9	aip.scitation.org Internet Source	<1 %
10	Advances in Superconductivity III, 1991. Publication	<1 %
11	tudr.thapar.edu:8080 Internet Source	<1 %
12	Handbook of Spintronics, 2016. Publication	<1 %
13	lr.ua.edu Internet Source	<1 %

63 you, long and 游, 龍. "Thermally Assisted Magnetic Writing on Microfabricated TbFe films for Magnetic Random Memory Applications", NAGOYA Repository (New oai_dc setup Aug 2014), 2008. <1%

Publication

Exclude quotes	On	Exclude matches	< 14 words
Exclude bibliography	On		

University of Hyderabad
School of Physics
Professor C R Rao Road, Central University P O
Gachibowli, Hyderabad 500046, India

Dr. Venkataiah Gorige
Assistant Professor
E-Mail: vgsp@uohyd.ac.in

Tel: +91 40 2313 4303
Fax: +91 40 2301 0227

May 27, 2022
Hyderabad

TO WHOM IT MAY CONCERN

This is to certify that the thesis entitled "**Correlation between structural, microstructural and magnetic properties of $CoFe_2O_4$ and $La_{0.7}Sr_{0.3}MnO_3$ nano, bulk and thin films for possible room-temperature device applications**", submitted by **Mr. Avisek Das** (Reg. No.: 15PHPH19) has been screened by the Turnitin software at the Indira Gandhi memorial library (IGML), University of Hyderabad. This software shows a 16% similarity index out of which approximately 9% came from the candidate's own research article (where he is the first author) directly related to this thesis. From the detailed similarity index report, it is obvious that the remaining 7% of the similarity index, is due to the resemblance caused by the frequent use of the well-known standard terms such as magnetism, manganite, ferrite, superexchange, double exchange, magnetoelectric, ferromagnetic, ferrimagnetic, Curie temperature, strain, crystal structure, x-ray diffraction, scanning electron microscopy, transmission electron microscopy, Rietveld refinement, Raman effect, temperature, spectra, coupling, magnetization, magnetic moment, coercivity, hysteresis loop, magnetic field, electric field, ferromagnetic resonance, Gilbert damping factor, spin-waves, magnons, spintronics, etc. to name a few. The use of such terms is rampant in the literature, and hence it is not surprising that the similarity index is artificially inflated. It should be noted that the use of such standard terms cannot be avoided.

Venkataiah Gorige
(Thesis supervisor)

DR. VENKATAIAH GORIGE
Assistant Professor
School of Physics, University of Hyderabad
Gachibowli, Hyderabad 500046, INDIA